Terahertz Time-Domain Spectroscopy and Near-Field Imaging of Microstructured Waveguides

Pan, Yi

Award date:
2013

Awarding institution:
University of Bath

TERAHERTZ TIME-DOMAIN SPECTROSCOPY AND NEAR-FIELD IMAGING OF MICROSTRUCTURED WAVEGUIDES

Yi Pan

A thesis submitted for the degree of Doctor of Philosophy

University of Bath

Department of Physics

May 2013

Abstract

This thesis presents studies of novel terahertz photonic devices, including photoconductive optoelectronic devices and guided-wave components, aimed at the development of next-generation terahertz systems.

In chapter 2, a scalable interdigitated THz transmitter is designed to increase the output power and compared with a conventional 50 μm coplanar transmitter. In chapter 3, we compare four different receivers with different antenna geometries in terms of bandwidth and sensitivity. Then we describe a photoconductive near-field detector with a subwavelength aperture and its system integration and characterization.

In chapter 4, a parallel metal plate waveguide is designed with an integrated step inside the waveguide that can couple to higher order TM modes efficiently from the TEM mode. In this chapter, we also experimentally and numerically study a 2-dimensionally tapered parallel plate waveguide, by which a free-space THz beam can be focused into a deep subwavelength-scale volume. In chapter 5, a parallel thin dielectric film waveguide is used to explore the guiding mechanism of an antiresonant optical reflection waveguide. Cylindrical silica single capillaries and a microstructured capillary, which guide in a similar way, are characterized in terms of mode profiles and attenuation. In chapter 6, we study oblique transmission through freestanding thin nickel films, which are perforated with periodic conical hole arrays. Surface modes can be supported by both metallic surfaces with different nonlinear dispersion curves, which results in spectral interferences in a near-field region when the surface modes couple out of the waveguide into free space.

Acknowledgements

I would like to thank many people during my work for the PhD study. It has been a great privilege to spend four years in the Department of Physics at University of Bath, and its members will always remain dear to me.

I would like to express my heartfelt gratitude to my supervisor, Steve Andrews for giving me this opportunity to undertake the study and his patience during my research works. I would like to thank great researchers, Fei Yu and Jonathan Knight during our collaboration on the silica capillary project.

Special thanks to Physics Department and many people, Paul Reddish, Catherine Dyer and Wendy Lambson for their support, guidance and helpful suggestions. I owe them my heartfelt appreciation.

Lastly, I would like to thank my wife, Junting Duan and my parents for all their love and encouragement. I hope that this work makes you proud.

Contents

Chapter 1 Introduction

1.1 The terahertz spectrum and THz-TDS

The terahertz (THz) spectrum spans the frequency range from 100 GHz to 10 THz and lies between the mid-infrared and microwave regions. Historically this frequency region has been explored for over one hundred years with the names sub-millimetre wave or far-infrared but it has been a resurgence of interest in the last two decades [1]. In that period, THz science and technology has grown rapidly [2] and has been making an impact in many application areas, including materials science [3], security [4], manufacturing [5] and medicine [6].

There are a number of commercially available THz sources, such as optically pumped gas lasers and backward wave oscillators which are operated in continuous wave mode with up to tens of milliwatt output power [2]. Solid state devices such as Gunn Diodes with Schottky-diode multiple chains can generate hundreds of GHz [4]. More recently, narrowband emitters have also been realized with quantum cascade lasers (QCL), which exploit intersubband transitions in quantum well structures [7]. Thanks to developments in ultrafast lasers, broadband, optically excited pulsed source of THz radiation have realized since the 1980s.

Terahertz time domain spectroscopy (THz-TDS) has played a large part in recent developments [8]. In this technique, broadband pulses of THz radiation are coherently generated and detected using ultrafast laser pulses with a time resolution of a few hundred femtoseconds. Fourier transform of the time-domain signal gives both spectral amplitude and phase information which allows probing of the real and imaginary parts of the dielectric function of materials. Extremely high signal-noise ratios of up to 10^6 in electric field make the technique very powerful despite the low source power of typically a few micro watts.

Further technological development of THz-TDS is being actively explored. For example, there has been recent progress on high resolution near-field imaging

techniques [9, 10] and ultra-broadband and intense generation in air [11, 12]. Nevertheless, many technologies taken for granted in other frequency ranges are relative poorly developed at THz frequencies. A specific example is that of THz waveguides.

1.2 Overview of THz waveguides

As the terahertz band lies in the gap between optical frequencies and microwaves, the concepts of waveguides have been borrowed from the two mature technologies. Here, we briefly review THz waveguide technology.

For delivering electromagnetic energy over a long distance, transmission loss is the first concern, whilst in time-domain measurements, low dispersion is also a requirement. Metal structures can efficiently guide THz radiation because of nearly perfect mirror reflection by metal surfaces. The metallic parallel plate waveguide (PPWG), widely used at microwave frequencies, can be used at THz frequencies with a low loss of ~5 dB/m at 1 THz and supports a single TEM mode with negligible dispersion [13, 14]. The loss is determined by finite surface conductivity and increases with increasing frequency and inversely linearly increases with increasing plate separation. Hollow metal tubes can support a TE_{11} mode efficiently [15] with a cutoff frequency. The loss has a cubic growth with decreasing the diameter. For example, a bendable metal pipe of 1 mm diameter was demonstrated with a loss of 7-8 dB/m at 1.5 THz [16]. There is a trade-off between the confinement and the loss.

Total internal reflection in dielectric provides another route to guiding THz radiations using high-index dielectric structures, such as sapphire fibre [17], plastic ribbon [18], and plastic fibre [19, 20]. However, nearly all dielectric materials exhibit high material absorption (>10 dB/m), except for high-resistivity single crystal silicon. To reduce material absorption, THz waves can be guided in air. Hollow core waveguides have been demonstrated with plastic photonic crystal fibre [21] and capillary [22, 23]. However, losses are typically tens of dB/m. Hybrid metal-dielectric structures are perhaps a more promising technology. For example, a hollow metal tube with a thin-dielectric coating on the inner surface has shown a remarkably low loss of 1 dB/m at 2.5 THz over a broad transmission window [24, 25], although several higher order

modes (TE) are generally excited with the fundamental mode (HE). The dielectric material should be a low loss material and the layer thickness has to be accurately designed for optimal transmission at the desired frequencies [26]. The dielectric material also increases the dispersion of the propagating field.

Chemical and biochemical sensing are some of the most promising applications of THz spectroscopy [27]. If materials are limited and a lack of sensitivity is an issue, it is beneficial to increase the interaction between samples and THz radiation using waveguides. Strong absorption line signatures in the spectrum enable chemists to differentiate and recognize samples [27], so that broadband transmission without modal interferences is desirable. A good example is Grischkowsky's study of water vapour absorption in a PPWG [28]. The TEM mode is uniformly distributed in the gap, which can be adjusted to achieve a significant modal overlap with very thin samples.

It is also sometimes desirable to have open access to the guided mode. Planar metal waveguides have potential in this regard. THz surface waves, known as Zenneck wave [29], can be supported on a metal surface, but the wave extends into air for hundreds of wavelengths. Recently, the field confinement has been dramatically improved by two orders of magnitude with subwavelength-scale metamaterial structures [30]. However, the confined field can be disturbed simply by the physical proximity of samples. For example, the surface field collapses if a dielectric material is deposited onto a metal surface [31]. Slight variations in sample thickness can also modify a transmission spectrum considerably [32].

Coplanar waveguides and striplines that are commonly used at microwave frequencies have been studied at THz frequencies but show large attenuation and dispersion over short propagation lengths of a few mm. Nevertheless, the THz field is strongly confined and interacts with dielectric samples held in close proximity. Spectral features, such as vibrational absorption, can be determined from the transmitted time domain signal [33, 34].

1.3 Roadmap for this thesis

This thesis begins by describing progress on the development of terahertz photoconductive sources and detectors, and then focuses on our studies of

microstructured waveguides. Experimental studies were carried out using near and far field time-domain THz spectroscopy in the frequency range 0.1-3 THz. Numerical simulations were generally performed to verify the experimental results and to obtain improved physical understanding.

Photoconductivity is commonly used for THz generation and detection in many research and commercial THz-TDS systems. Our work focuses on designing THz transmitters and receivers to improve the system's sensitivity and imaging capability. In Chapter 2, we describe the characterization of an interdigitated THz emitter and compare the output power with a conventional 50 μm-gap coplanar antenna. Chapter 3 describes experimental and numerical studies on four different geometry receiving antennas. Then we present a photoconductive near-field receiver with integrated aperture.

The main part of this thesis is composed of three chapters concerning THz waveguides. Chapter 4 introduces two modified parallel metal plates waveguides: a stepped PPWG and a tapered PPWG. Chapter 5 presents studies of parallel dielectric thin-film waveguides, silica capillaries and a microstructured capillary. Chapter 6 describes guiding on a freestanding nickel film perforated with a hexagonal array of holes.

References

1. M. Tonouchi, "Cutting-edge terahertz technology," Nature Photonics **1**, 97-105 (2007).

2. A. Dobroiu, C. Otani, and K. Kawase, "Terahertz-wave sources and imaging applications," Measurement Science & Technology **17**, R161-R174 (2006).

3. B. Ferguson and X. C. Zhang, "Materials for terahertz science and technology," Nature Materials **1**, 26-33 (2002).

4. D. Saeedkia and S. Safavi-Naeini, "Terahertz Photonics: Optoelectronic Techniques for Generation and Detection of Terahertz Waves," Journal of Lightwave Technology **26**, 2409-2423 (2008).

5. D. M. Mittleman, R. H. Jacobsen, and M. C. Nuss, "T-ray imaging," Ieee Journal of Selected Topics in Quantum Electronics **2**, 679-692 (1996).

6. E. Pickwell and V. P. Wallace, "Biomedical applications of terahertz technology," Journal of Physics D-Applied Physics **39**, R301-R310 (2006).

7. B. S. Williams, "Terahertz quantum-cascade lasers," Nature Photonics **1**, 517-525 (2007).

8. M. Van Exter and D. R. Grischkowsky, "Characterization of an optoelectronic terahertz beam system," Ieee Transactions on Microwave Theory and Techniques **38**, 1684-1691 (1990).

9. O. Mitrofanov, I. Brener, R. Harel, J. D. Wynn, L. N. Pfeiffer, K. W. West, and J. Federici, "Terahertz near-field microscopy based on a collection mode detector," Applied Physics Letters **77**, 3496-3498 (2000).

10. N. C. J. van der Valk and P. C. M. Planken, "Electro-optic detection of subwavelength terahertz spot sizes in the near field of a metal tip," Applied Physics Letters **81**, 1558-1560 (2002).

11. X. Xie, J. M. Dai, and X. C. Zhang, "Coherent control of THz wave generation in ambient air," Physical Review Letters **96**, 075005-075008 (2006).

12. D. J. Cook and R. M. Hochstrasser, "Intense terahertz pulses by four-wave rectification in air," Optics Letters **25**, 1210-1212 (2000).

13. S. Coleman and D. Grischkowsky, "A THz transverse electromagnetic mode two-dimensional interconnect layer incorporating quasi-optics," Applied Physics Letters **83**, 3656-3658 (2003).

14. R. Mendis and D. Grischkowsky, "Undistorted guided-wave propagation of subpicosecond terahertz pulses," Optics Letters **26**, 846-848 (2001).

15. G. Gallot, S. P. Jamison, R. W. McGowan, and D. Grischkowsky, "Terahertz waveguides," Journal of the Optical Society of America B **17**, 851-863 (2000).

16. T. Ito, Y. Matsuura, M. Miyagi, H. Minarnide, and H. Ito, "Flexible terahertz fiber optics with low bend-induced losses," Journal of the Optical Society of America B **24**, 1230-1235 (2007).

17. S. P. Jamison, R. W. McGowan, and D. Grischkowsky, "Single-mode waveguide propagation and reshaping of sub-ps terahertz pulses in sapphire fibers," Applied Physics Letters **76**, 1987-1989 (2000).

18. R. Mendis and D. Grischkowsky, "Plastic ribbon THz waveguides," Journal of Applied Physics **88**, 4449-4451 (2000).

19. B. You, J.-Y. Lu, T.-A. Liu, J.-L. Peng, and C.-L. Pan, "Subwavelength plastic wire terahertz time-domain spectroscopy," Applied Physics Letters **96**, 051105 (2010).

20. L. J. Chen, H. W. Chen, T. F. Kao, J. Y. Lu, and C. K. Sun, "Low-loss subwavelength plastic fiber for terahertz waveguiding," Optics Letters **31**, 308-310 (2006).

21. H. Han, H. Park, M. Cho, and J. Kim, "Terahertz pulse propagation in a plastic photonic crystal fiber," Applied Physics Letters **80**, 2634-2636 (2002).

22. J.-Y. Lu, C.-P. Yu, H.-C. Chang, H.-W. Chen, Y.-T. Li, C.-L. Pan, and C.-K. Sun, "Terahertz air-core microstructure fiber," Applied Physics Letters **92**, 064105 (2008).

23. E. Nguema, D. Ferachou, G. Humbert, J.-L. Auguste, and J.-M. Blondy, "Broadband terahertz transmission within the air channel of thin-wall pipe," Optics Letters **36**, 1782-1784 (2011).

24. O. Mitrofanov and J. A. Harrington, "Dielectric-lined cylindrical metallic THz waveguides: mode structure and dispersion," Optics Express **18**, 1898-1903 (2010).

25. O. Mitrofanov, R. James, F. A. Fernandez, T. K. Mavrogordatos, and J. A. Harrington, "Reducing Transmission Losses in Hollow THz Waveguides," Terahertz Science and Technology, IEEE Transactions on 1, 124-132 (2011).

26. J. A. Harrington, "A review of IR transmitting, hollow waveguides," Fiber and Integrated Optics **19**, 211-227 (2000).

27. A. I. McIntosh, B. Yang, S. M. Goldup, M. Watkinson, and R. S. Donnan, "Terahertz spectroscopy: a powerful new tool for the chemical sciences?," Chemical Society Reviews **41**, 2072-2082 (2012).

28. J. Q. Zhang and D. Grischkowsky, "Waveguide terahertz time-domain spectroscopy of nanometer water layers," Optics Letters **29**, 1617-1619 (2004).

29. T. I. Jeon and D. Grischkowsky, "THz Zenneck surface wave (THz surface plasmon) propagation on a metal sheet," Applied Physics Letters **88**, 061113 (2006).

30. C. R. Williams, S. R. Andrews, S. A. Maier, A. I. Fernandez-Dominguez, L. Martin-Moreno, and F. J. Garcia-Vidal, "Highly confined guiding of terahertz surface plasmon polaritons on structured metal surfaces," Nature Photonics **2**, 175-179 (2008).

31. M. Gong, T.-I. Jeon, and D. Grischkowsky, "THz surface wave collapse on coated metal surfaces," Optics Express **17**, 17088-17101 (2009).

32. J. F. O'Hara, R. Singh, I. Brener, E. Smirnova, J. Han, A. J. Taylor, and W. Zhang, "Thin-film sensing with planar terahertz metamaterials: sensitivity and limitations," Optics Express **16**, 1786-1795 (2008).

33. S. Kasai, A.Tanabashi, K. Kajiki, T. Itsuji, R. Kurosaka, H. Yoneyama, M. Yamashita, H. Ito, and T. Ouchi, "Micro Strip Line-Based On-Chip Terahertz Integrated Devices for High Sensitivity Biosensors", Applied Physics Express **2**, 062410 (2009)

34. M. B. Byrne, J. Cunningham, K. Tych, A. D Burnett, M. R. Stringer, C. D. Wood, L. Dazhang, M. Lachab, E. H. Linfield, and A. G. Davies, "Terahertz vibrational absorption spectroscopy using microstrip-line waveguides", Applied Physics Letter **93**, 182904 (2008)

Chapter 2

Interdigitated coplanar transmitter

2.1 Free-space THz time-domain spectroscopy

Photoconductive antennas are the key components in most THz time-domain spectroscopy (THz-TDS) systems [1]. The typical structures we have used for transmitters and receivers are sketched in Figure 2.1 (a) and (b), respectively. The electrodes consist of 20 nm of titanium and 200 nm of gold deposited on a semiconductor substrate using a conventional photolithography, thermal evaporation and lift-off processes. The transmitter is a coplanar stripline design and the receiver a dipole antenna. The transmitters are made from semi-insulating GaAs (SI-GaAs) and the receivers from low-temperature GaAs (LT-GaAs) epitaxially grown on a SI-GaAs substrate with an intervening layer of AlAs.

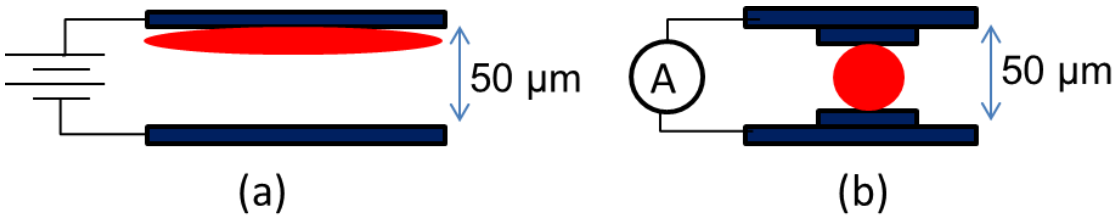

Figure 2.1. (a) A coplanar waveguide transmitter biased with an external voltage of 50 V. The red area indicates the laser focus. (b) A dipole receiver connected to a current meter. A circular laser spot is focused on the photoconducting gap between the antenna arms.

Our THz-TDS system is an optical pump and probe setup as shown in Figure 2.2. The system employs a self-mode-locked Ti:Sapphire laser optically pumped by a

continuous-wave (cw) argon-ion laser with 8 W average output power. The femtosecond laser has a repetition rate of 82 MHz and produces 70-130 fs pulses with a central optical wavelength in the range 740-820 nm. A pair of SF18 prisms (not shown) is used immediately in front of the laser to introduce negative group velocity dispersion (GVD) to compensate for pulse broadening in the rest of the optical system. The term of GVD used in the thesis indicates that the group velocity of THz waves travelling in waveguides depends on its wavelength. The femtosecond laser beam is divided by a beam splitter into pump and probe beams, where typically 90 mW laser power is transferred to the pump arm before chopping and 20 mW to the probe arm.

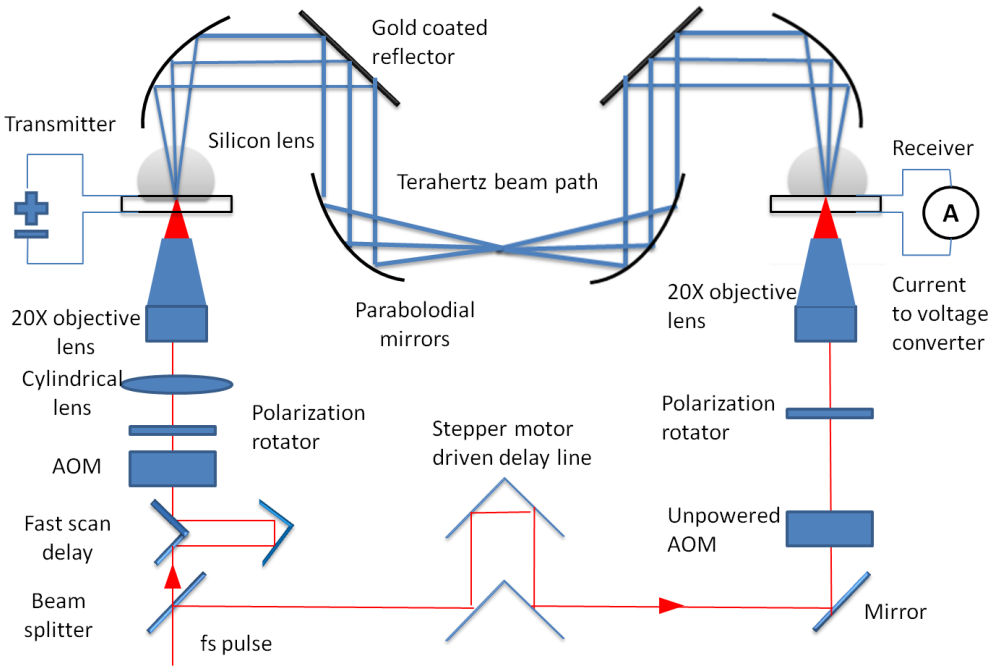

Figure 2.2. Schematic of the free space pump-probe terahertz time-domain spectroscopy system. The time-domain signal is mapped by varying the transmitter beam path using a fast scan delay line.

The pump beam is usually time-delay modulated by a fast scanning retro-reflector. An acoustic-optic modulator (AOM) chops the pump beam at a frequency of 6.5 kHz and the receiver current is detected using a lock-in amplifier to improve the signal to noise ratio. A cylindrical lens and a 20× microscope objective produce a line focus on the transmitter with an area ($1/e^2$ diameter of ~4 μm×100 μm) [2]. This arrangement enhances the THz emission by a factor of 2-3 compared with a point focus. The illumination is close to the positive track where the radiation efficiency is larger due to geometrical and trap enhancement of the quasi-static field and the high mobility of

electrons compared with holes [3]. The polarization of the pump beam is perpendicular to the metal edges of the antenna structure to optimize the emission efficiency [4].

The fs laser pulse generates free carriers in the photoconducting gap of the transmitter. When a DC bias voltage of typically 50 V is applied to the 50 μm spaced electrodes on the transmitter, the transient conductivity leads to a sub-picosecond electrical current transient and consequently generates THz radiation. The largest fraction of the THz radiation is emitted into the GaAs substrate. A hyper hemispherical silicon substrate lens is attached to the back of the transmitter to avoid total internal reflection at the substrate-air interface. A high resistivity silicon lens is chosen because of its low absorption coefficient of 0.05 cm^{-1} and low dispersion over the frequency range 0.1-5 THz [5]. The THz radiation propagates and diffracts towards an off-axis parabolic mirror which collimates the radiation into a highly directional beam. The THz beam is re-focused by another parabolic mirror and a silicon lens onto the receiving antenna.

In practice, it should be noted that for the SI-GaAs transmitter, the average photo-induced current is restricted to around 1 mA to maintain a long working lifetime. Alignment of the silicon lenses to a precision of a few μm is essential to optimise the high sensitivity and bandwidth.

The probe laser beam passes through an identical unpowered AOM to match the dispersion in the pump beam. Then the pulse is retro-reflected by a long stepper motor driven delay line which allows long-distance scans and changes to the experimental geometry. A 20× microscope objective focuses the probe beam to a $1/e^2$ diameter of about 5 μm to switch on the receiver for THz detection.

When not optically illuminated the receiver has a high resistance. The incident electric field of the THz beam induces a transient current in the antenna of the receiver only when it is optically gated. This current is mapped as a function of pump-probe delay and is roughly proportional to the electric field of the THz pulse. The time resolution and bandwidth are limited by the gating pulse width, carrier scattering and trapping times, the antenna geometry and the THz optics. The THz beam path is purged with dry air to reduce the effect of water absorption. Data is usually collected with the faster scanning delay line which allows real time optimization on an oscilloscope. The effects of system drift are reduced by averaging multiple scans.

2.2 THz generation model

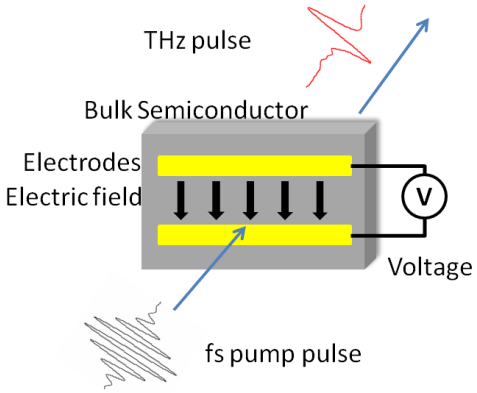

Figure 2.3. Schematic of photoconductive THz generation, where a near-infrared laser pulse excites electron-hole pairs in the semiconductor between the electrodes.

In a photoconductive transmitter a pair of parallel metallic electrodes stores the static electrostatic energy, $E_c = (1/2)CV^2$, where C is the capacitance of the photoconducting gap and V is the applied bias voltage. A portion of this energy can be converted to THz radiation under pulsed laser excitation of the gap between the electrodes in the arrangement shown in Figure 2.3 [6]. A transient photocurrent partially screens the applied field and depletes the stored energy on a time scale of 100 fs [6], and is given by,

$$j(t) = eN(t)v(t) \tag{2.1}$$

where $v(t)$ is the time dependent velocity of free carriers and the time dependence of the carrier density $N(t)$ is given by,

$$\frac{dN}{dt} = G(t) - \frac{N(t)}{\tau_c} \tag{2.2}$$

where $G(t)$ is the carrier generation rate of the laser pulse and τ_c is the carrier trapping time (~100 ps for SI-GaAs and ~1 ps for LT-GaAs). The first term describes the generation of free carriers on the time scale of the laser pulse duration (~100 fs) and the second describes the evolution of the carrier density at longer times.

The equation of electron motion is given by,

$$\frac{dv}{dt} = -\frac{v}{\tau_s} + \frac{e}{m^*}E(t) \tag{2.3}$$

where the τ_s is the momentum relaxation time (~30 fs for LT-GAs), m^* is the effective mass and $E(t)$ is the bias field across the photoconductive gap.

The radiated THz field is proportional to the temporal derivative of the photocurrent and is given by,

$$E_{THz} \propto \frac{dj}{dt} \approx ev(t)\frac{dG(t)}{dt} + G(t)e\mu\frac{dE(t)}{dt} \tag{2.4}$$

in the farfield, where μ is the carrier mobility. This assumes that $\omega\tau_s \ll 1$, so that μ is independent of time. The electric field obtained from Eq (2.4) is plotted in Figure 2.4. Here, we have used a Gaussian laser pulse with full width at half maximum (FWHM) of 100 fs, a carrier scattering time τ_s of 30 fs and a carrier recombination time of 300 fs. The screening effect has not taken into account and the carrier trapping and recombination is assumed to follow a single exponential decay.

The THz bandwidth is mainly determined by the laser pulse duration and not by the relatively long decay time of the photocurrent. This is why both SI-GaAs with 100 ps carrier lifetime and LT-GaAs with only few ps lifetime both behave similarly as THz transmitters.

We review the dynamics of the free carriers in the THz emission process: (a) photoexcited free carriers are generated and accelerated by the external bias field; (b) the electrons and holes move apart so as to screen the applied field; (c) the reduced field leads to a deceleration of free carriers akin to a restoring force. The carrier dynamics process can be treated as an oscillating electric dipole moment [9]. The high initial momentum is provided with the external electric field and the damping factor is associated with the carrier scattering and collisions. Generally speaking, the high frequency components have a strong contribution from the screening effect. The model has not taken account of the frequency responses of the antenna and the THz optical system.

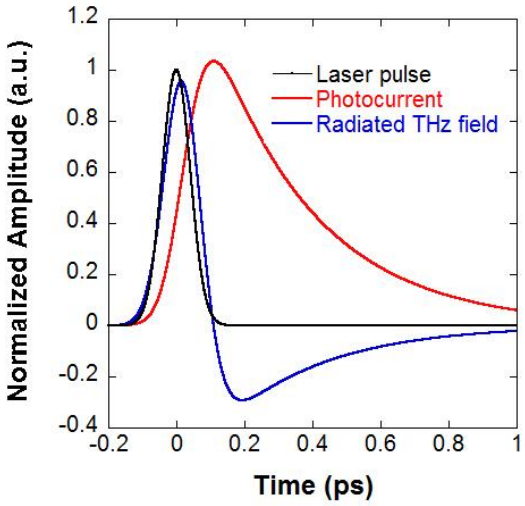

Figure 2.4. Time variations of the laser pulse, transient photocurrent, and radiated field in the far-field. The details of the parameters used for the plot are in the text.

2.3 Interdigitated coplanar THz antenna

Different photoconductive (PC) transmitter designs have been studied to improve the optical to THz conversion efficiency and the THz frequency response. Dipole antennas made on silicon on sapphire [12] were the first used. Later several other antenna patterns were investigated, such as equiangular spiral [13], planar [14] and exponentially tapered coplanar stripline [15], which were found to be more efficient at low frequency (<0.5 THz). Cai *et al* [16] reported enhanced emission efficiency using pointed dipole arms, but the bandwidth is reduced and the structure is prone to electrical breakdown.

Hitherto, Grischkowsky's coplanar stripline structure with a separation of 50 μm [17] has been the most commonly used transmitter device, because of its relative high average power of typically a few μW and large bandwidth of 3 THz at 10% maximum amplitude in a typical THz-TDS setup, although the bandwidth is also dependent of THz optical system and detection. This structure does not contain a resonant antenna; instead the electron-hole plasma behaves as a point dipole source. The performance can be improved by a factor of 2 to 3 using line focus illumination so that more of the capacitively stored energy is converted into radiation. The main path to improving performance is simply to enlarge the active area and use more near-infrared power rather than improving the energy conversion efficiency.

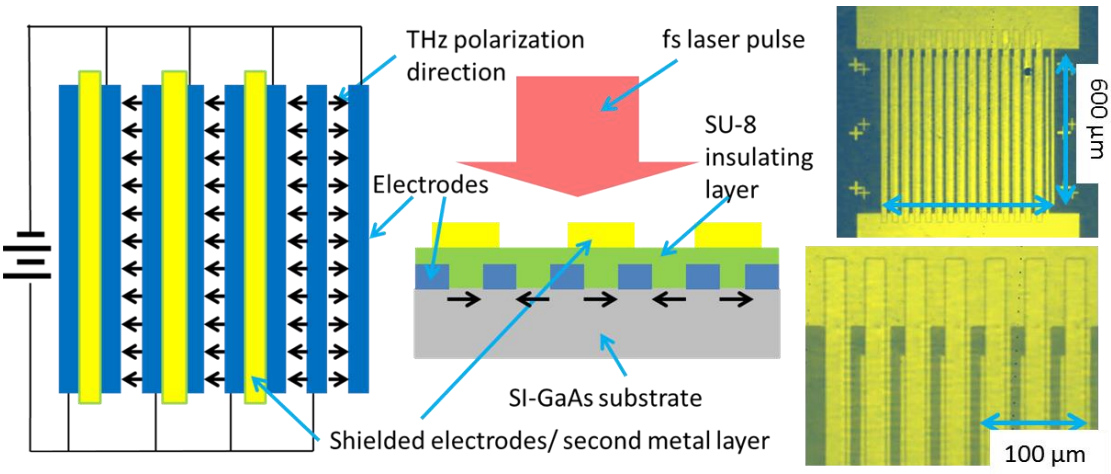

Figure 2.5. (a) Schematic of the interdigitated THz transmitter structure. The black arrows show the bias field direction. (b) Schematic side view of the multilayer structure. (c) Optical microscope image of the transmitter (d) Magnified image of (c).

An innovative transmitter design was demonstrated in 2005 by Dreyhaupt *et al* [18]. The concept was to build multiple coplanar antennas on a single substrate using interdigitated electrodes. As the electric field is normally reversed every period in such a structure, every other electrode gap was covered by an insulated metal layer to avoid THz field cancellation, as shown in Figure 2.5. The electrode spacing in an individual coplanar antenna is a few µm. Obviously, the scalable transmitter enlarges the active region but at the expense of low applied bias and substrate silicon lenses can no longer be used effectively. In the simple generation model described above, the THz amplitude is linearly proportional to the applied field across the electrodes. In this chapter, the efficiency of the new design is compared with Grischkowsky's conventional coplanar transmitter.

2.4 Experimental results and discussion

2.4.1 Emission properties of single electrode pair

We replicated the interdigitated device design reported in Ref. 18 with a similar structure, shown in Figure 2.5. The device was fabricated on SI-GaAs substrates using conventional photolithography techniques. The active area is 600 µm by 600 µm. The interdigitated electrodes were deposited with Ti/Au of thicknesses of 10/200 nm. Then a layer of dilute SU-8 with thickness of ~1 µm was spin-coated and UV exposed to

provide a pinhole-free insulating layer. Every second gap was covered by a second metal layer of Ti:Au to allow constructive interference in the far field. The width of the bottom electrodes and the gaps are both 10 μm, whilst the shielding strips are 20 μm wide.

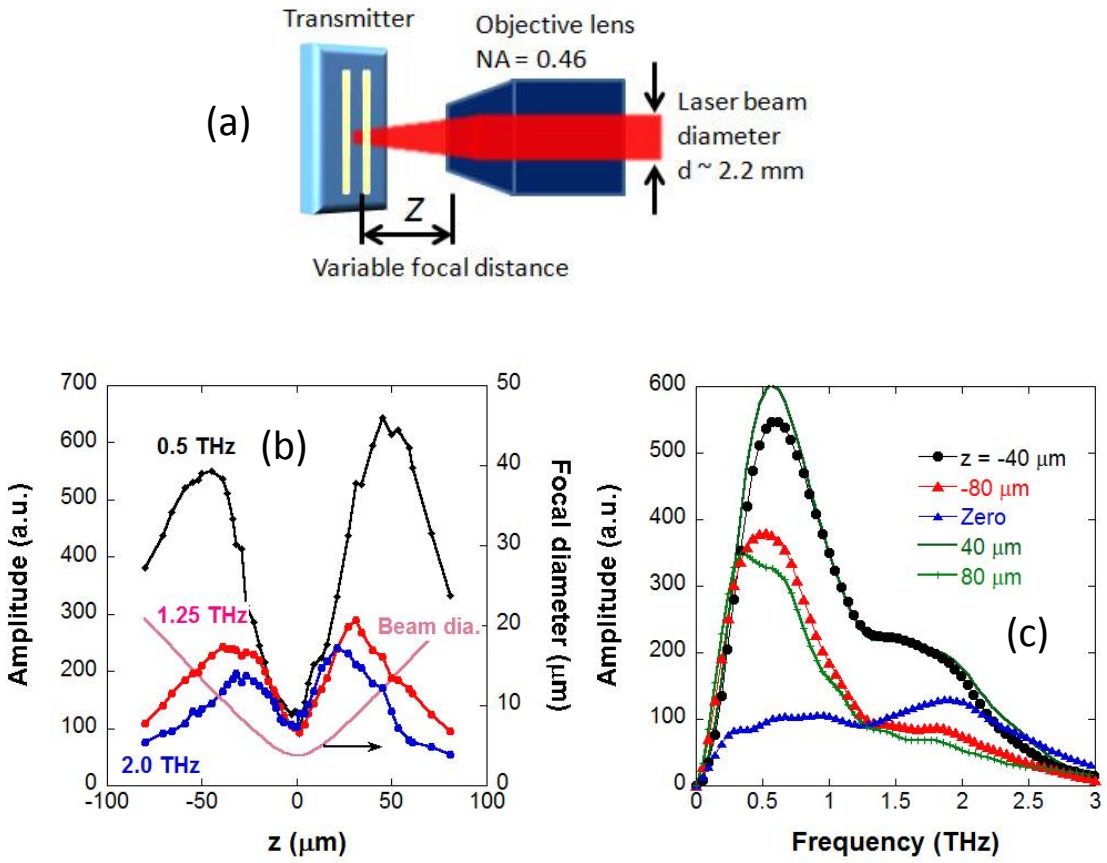

Figure 2.6. (a) Configuration for varying the excitation-spot size for the single element transmitter. (b) The z-amplitude profile at three different frequencies. The pink line shows the calculated spot size. (c) Spectrum comparison for different lens positions.

We first characterized the emission properties of a single pair of electrodes, i.e. a single element of the interdigitated transmitter, using a tightly focused laser spot. The spot diameter was varied by adjusting the distance between the objective lens and the transmitter as shown in Figure 2.6 (a). The intensity of the pump laser beam was kept constant at 1.0 mW. The applied bias was set to 20 V, which was restricted by a nominal photocurrent limit of ~1 mA. Regarding the anode-enhancement effect, Cai *et al* [16] suggested that the anode-enhanced THz emission intensity is absent or reduced in small gap structures (<50 μm). However, we still found a trap enhancement in our microstructured transmitter. Experimental results showed that an asymmetrical

emission between positive and negative tracks still exists at track separations as smaller as 7 and 4 μm. Consequently, the excitation spot was always adjusted to be close to the anode.

The diffraction limited focal spot diameter ($2w_0$ = 1/e^2 diameter) is given by

$$2w_0 = \frac{4\lambda f}{\pi D} M^2 = 3.8\,\mu m \tag{2.5}$$

where λ = 765 nm is the wavelength and f = 9 mm is the focal length of the objective lens, D = 2.2 mm is the incidence laser beam diameter, and M^2 is the beam quality factor of ~1. Assuming Gaussian beam propagation, the diameter as a function of lens position along the z axis is given by,

$$2w_z = 2\omega_0 \left[1 + M^2 (\frac{\lambda z}{\pi w_0^2})^2\right]^{1/2}. \tag{2.6}$$

Figure 2.6 (b) shows the amplitudes at three frequencies as a function of objective position. The optimum focal spot size is frequency dependent. The signal amplitude at the higher frequency of 2.0 THz reaches a maximum at $2w_z$ ~ 6 μm, i.e. before the laser spot fills the 10 μm gap. This is because the higher frequency generation relies on a strong screening effect and a small spatial overlapping of free-carriers (i.e. tight focusing). The decrease in amplitude with larger spot size is due to the increasing fraction of the laser power outside the gap region. The peak amplitude at the frequency of 1.25 THz occurs with full gap illumination.

Figure 2.6 (c) compares spectra at different lens z positions. The signals at z = 40 and 80 μm are almost identical except for a change in amplitude and very similar to those at z = -40 and -80 μm. It is clear that the tight laser focus at the zero position gives rise to a very broad band signal, with 10% amplitude bandwidth of 3.65 THz. On the other hand, the generation efficiency of lower frequency components is greater with the full gap illumination.

Then we measured the bias and pump power dependence of the emission from a single 10 μm-gap transmitter under conditions of tight focus (z = 0 μm) and full gap illumination (z = 40 μm). Dreyhaupt *et al* [18, 19] observed a spectral shift with

changing voltage. However, we found that the spectral shape was independent of bias and the peak THz signal increased linearly with bias.

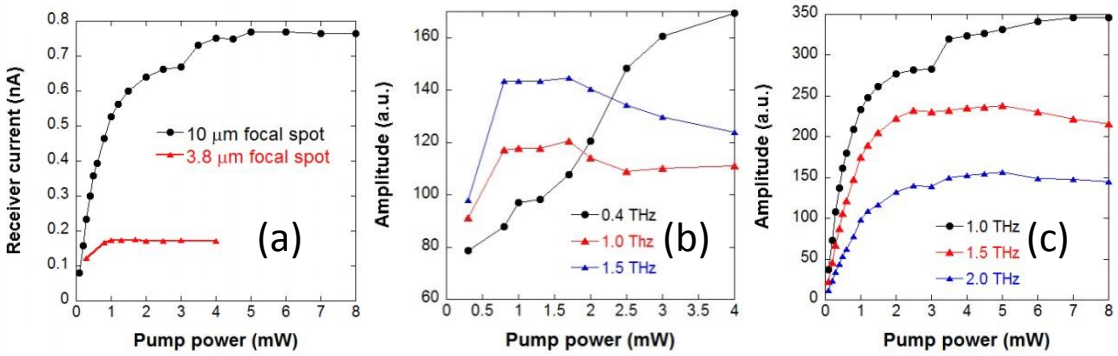

Figure 2.7. (a) Peak to peak receiver current as a function of optical pump power under two different illumination conditions of the single element transmitter. The spectral amplitude dependence on laser power with tightly focused spot (b) and full gap illumination (c).

Figure 2.7 (a) shows that the peak to peak THz signal saturates at laser pump powers of 1 and 5 mW with amplitudes of 0.16 and 0.78 nA for tight focus and large spot, respectively. Figure 2.7 (b) shows that the high frequency emission is suppressed above saturation for tighter focus, as a result of the reduction of the screening effect [6]. However, in Figure 2.7 (c), illumination with a large spot shows similar saturation for all the frequencies. The results contribute to an understanding of the effect of illumination on bandwidth in the next section, where we describe the studies of the complete structure.

2.4.2 Emission properties of complete structure

To study the emission characteristics of the complete interdigitated THz antenna, the laser pump beam was defocused to cover the active area of 0.36 mm^2. The bias voltage was 20 V and limited by the safe photocurrent, which we estimated to be ~15 mA.

We compared the interdigitated transmitter with a conventional 50 μm gap separated coplanar transmitter in terms of signal amplitude and bandwidth. For the conventional transmitter, the optimal bias was 40 V and the pump power was 50 mW after chopping. The peak to peak amplitude of the THz signal was about 100 nA with the 10 μm dipole receiver. The peak emission frequency is at 1 THz and the 10% amplitude bandwidth is

3 THz.

The interdigitated device was capable of generating a signal amplitude with 180 nA at 180 mW pump power but lower frequency components (<1 THz) dominate the spectrum. This is different to the case when the gap between two electrodes is fully illuminated (Figure 2.6c). As previously mentioned for full gap spot illumination the spectral bandwidth is independent of laser power. For this reason, the narrow band spectrum obtained with full illumination of the interdigitated devices is mostly likely a feature of the THz optical system. The emission is transferred and imaged onto the receiver with similar beam size, but the receiver response is limited by the small effective antenna area and the focused THz spot is frequency dependent. Consequently, higher frequencies make a relatively low contribution to the signal.

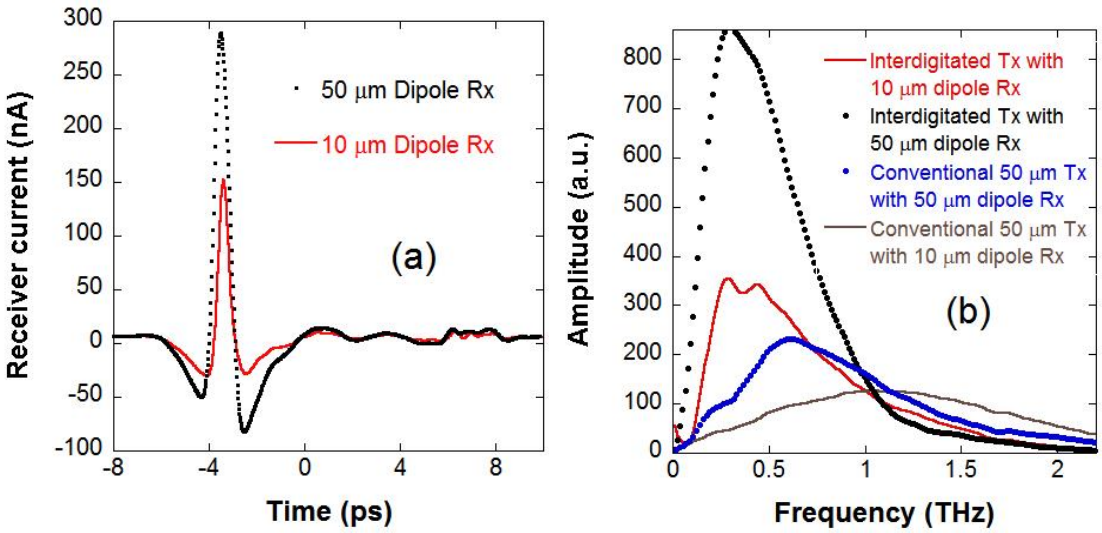

Figure 2.8. (a) The time-domain signals from the fully illuminated interdigitated antenna with two different receiver dipoles. (b) The corresponding spectra of (a) together with the spectrum of the conventional 50 μm-gap coplanar transmitter.

To confirm this picture, we switched the 10 μm receiver to a 50 μm dipole antenna which has a larger effective area and higher sensitivity to lower frequencies. Doing this with a conventional coplanar transmitter, the signal increases by 30% to 130 nA and the bandwidth decreases by 30% to 2 THz (Figure 2.8b). In comparison, the amplitude from the interdigitated transmitter increases to 380 nA, as shown in Figure 2.8 (a), but the bandwidth is only slightly reduced to 1.0 THz from 1.5 THz. The large increase in the amplitude and the slight reduction in the bandwidth confirm the picture presented above. To improve the detection efficiency, the interdigitated device should also be

used as a receiver and the silicon lens should be redesigned.

To find the optimum emission conditions under multiple track illumination, we varied the optical excitation area by defocusing the objective lens and monitored the laser beam diameter using a camera. Figure 2.9 (a) shows the signal amplitude dependence on the laser spot size. The maximum amplitude is obtained for an excitation spot size of the order of the central THz wavelength (~400 μm). As previously mentioned, under full gap illumination (Figure 2.7c), the spectral bandwidth is expected to be unaffected by the optical pump power. Figure 2.9 (b) shows however the spectral weight shifts to lower frequency with larger excitation spot size. We therefore again attribute this to the THz imaging system.

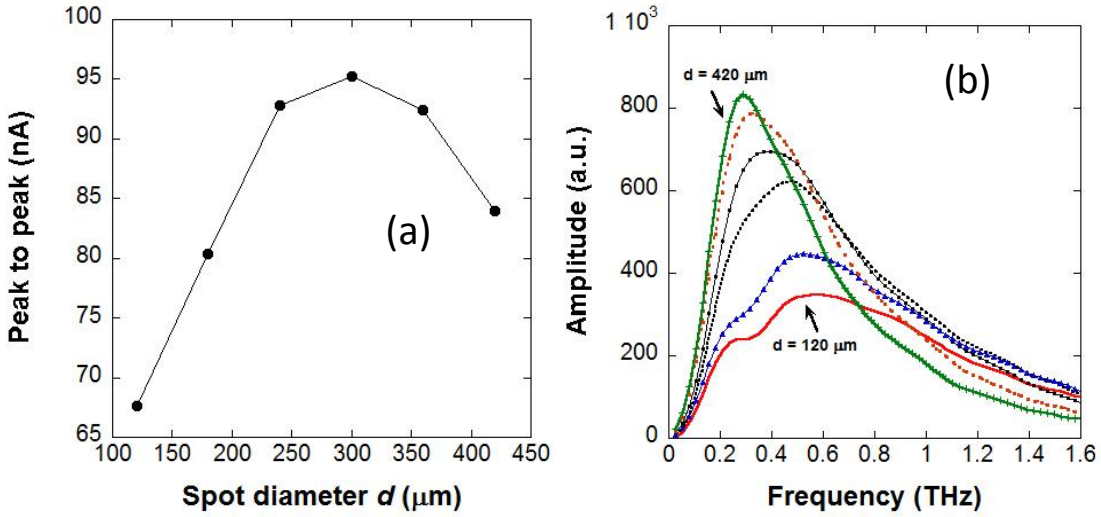

Figure 2.9 (a) Peak to peak receiver current versus the excitation spot size for the full interdigitated transmitter. (b) Dependence of the THz spectrum on the excitation spot size, corresponding to the measurements in (a).

We characterized the relative optical to THz power conversion efficiency of the interdigitated and conventional transmitters. In order to apply a high pump power, the bias applied to the conventional transmitter was turned down to 30 V, while the interdigitated device was maintained at 20 V. In Figure 2.10, the signal current is a function of pump power. The signal from the conventional transmitter saturates with a pump power of around 80 mW. In contrast, the signal from the interdigitated transmitter increases linearly with pump power. The study on the fully illuminated single pair of electrodes showed that the saturation power is 5 mW. The excitation area

was then $\pi \times 10 \times 10/4$ μm^2. For our full illumination under optimum condition the illuminated area is $\pi \times 400 \times 400/4$ μm^2, so that saturation is expected with a laser power of 8 W. The maximum optical power (180 mW) was far from the saturation power, which is why the signal amplitude varies linearly with pump power.

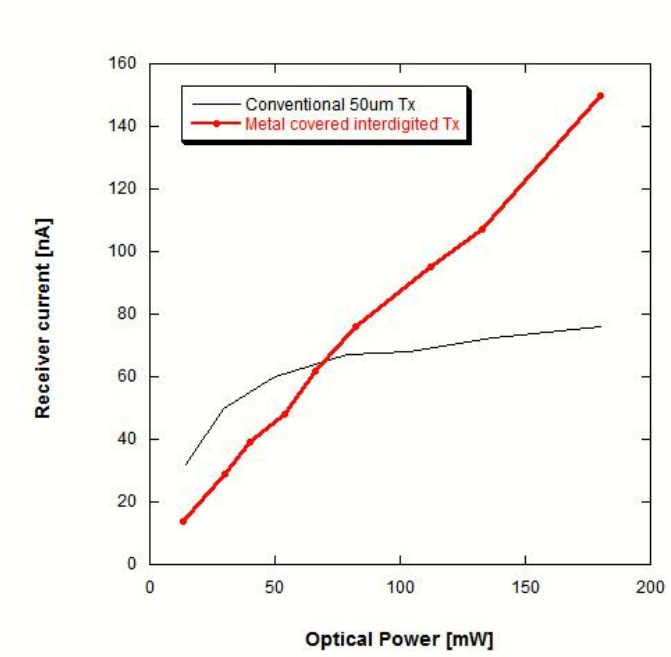

Figure 2.10. Comparison of peak to peak receiver current amplitudes of the interdigitated transmitter and 50 μm-gap coplanar transmitter using the 10 μm dipole receiver.

Finally, we calibrated a thermal bolometer with a silicon window using a blackbody source and used the bolometer to measure the average emission power of the transmitters under their optimum conditions. With a pump laser power of 50 mW and a bias of 50 V, the conventional coplanar transmitter gave a 100 nA peak to peak signal with a 10 μm dipole receiver. For the interdigitated device, the peak signal was 180 nA with a pump power of 180 mW and bias of 20 V and the same receiver. Under these conditions, the average powers were 14 and 27 μW for the coplanar and interdigitated transmitters, respectively.

2.5 Conclusions

We have designed and fabricated an interdigitated transmitter with a large active area of 600×600 μm^2 for high intensity THz emission. The characteristics of a single pair of

electrodes in this device have been experimentally studied as a function of illumination conditions to understand the THz emission process and gain the fundamental knowledge to use the interdigitated device efficiently.

The maximum emission power achieved from the interdigitated device is double that from a conventional 50 μm-gap coplanar transmitter according to our bolometer measurements. The device was operated far below its saturation pump power and the THz optics has not been optimized for its use in our THz system, so that much better results could be obtained in principle, particularly if using a similar device as a receiver.

References

1. M. Van Exter and D. R. Grischkowsky, "Characterization of an optoelectronic terahertz beam system," IEEE Transactions on Microwave Theory and Techniques **38**, 1684-1691 (1990).

2. S. R. Andrews, A. Armitage, P. G. Huggard, and A. Hussain, "Optimization of photoconducting receivers for THz spectroscopy," Physics in Medicine and Biology **47**, 3705-3710 (2002).

3. S. E. Ralph and D. Grischkowsky, "Trap-enhanced electric-fields in semi-insulators - the role of electrical and optical carrier injection," Applied Physics Letters **59**, 1972-1974 (1991).

4. P. G. Huggard, C. J. Shaw, J. A. Cluff, and S. R. Andrews, "Polarization-dependent efficiency of photoconducting THz transmitters and receivers," Applied Physics Letters **72**, 2069-2071 (1998).

5. C. Fattinger and D. Grischkowsky, "Terahertz beams," Applied Physics Letters **54**, 490-492 (1989).

6. P. U. Jepsen, R. H. Jacobsen, and S. R. Keiding, "Generation and detection of terahertz pulses from biased semiconductor antennas," Journal of the Optical Society of America B **13**, 2424-2436 (1996).

7. L. Duvillaret, F. Garet, J. F. Roux, and J. L. Coutaz, "Analytical modeling and optimization of terahertz time-domain spectroscopy experiments using photoswitches as antennas," IEEE Journal of Selected Topics in Quantum Electronics **7**, 615-623 (2001).

8. Z. S. Piao, M. Tani, and K. Sakai, "Carrier dynamics and terahertz radiation in photoconductive antennas," Japanese Journal of Applied Physics **39**, 96-100 (2000).

9. M. B. Johnston, D. M. Whittaker, A. Corchia, A. G. Davies, and E. H. Linfield, "Simulation of terahertz generation at semiconductor surfaces," Physical Review B **65**, 165301 (2002).

10. E. Castro-Camus, J. Lloyd-Hughes, and M. B. Johnston, "Three-dimensional carrier-dynamics simulation of terahertz emission from photoconductive switches," Physical Review B **71**, 195301 (2005).

11. V. L. Malevich, "Monte Carlo simulation of Dember effect in n-InAs under subpicosecond laser pulse excitation," Acta Physica Polonica A **107**, 169-173 (2005).

12. P. R. Smith, D. H. Auston, and M. C. Nuss, "Subpicosecond photoconducting dipole antennas," IEEE Journal of Quantum Electronics **24**, 255-260 (1988).

13. Y. Pastol, G. Arjavalingam, and J. M. Halbout, "Characterization of an optoelectronically pulsed equiangular spiral antenna," Electronics Letters **26**, 133-135 (1990).

14. A. P. Defonzo, M. Jarwala, and C. Lutz, "Transient-response of planar integrated optoelectronic antennas," Applied Physics Letters **50**, 1155-1157 (1987).

15. G. Arjavalingam, Y. Pastol, J. M. Halbout, and G. V. Kopcsay, "Broad-band microwave measurements with transient radiation from optoelectronically pulsed antennas," IEEE Transactions on Microwave Theory and Techniques **38**, 615-621 (1990).

16. Y. Cai, I. Brener, J. Lopata, J. Wynn, L. Pfeiffer, and J. Federici, "Design and performance of singular electric field terahertz photoconducting antennas," Applied Physics Letters **71**, 2076-2078 (1997).

17. N. Katzenellenbogen and D. Grischkowsky, "Efficient generation of 380 fs pulses of thz radiation by ultrafast laser-pulse excitation of a biased metal-semiconductor interface," Applied Physics Letters **58**, 222-224 (1991).

18. A. Dreyhaupt, S. Winnerl, T. Dekorsy, and M. Helm, "High-intensity terahertz radiation from a microstructured large-area photoconductor," Applied Physics Letters **86**, 121114 (2005).

19. A. Dreyhaupt, S. Winnerl, M. Helm, and T. Dekorsy, "Optimum excitation conditions for the generation of high-electric-field terahertz radiation from an oscillator-driven photoconductive device," Optics Letters **31**, 1546-1548 (2006).

Chapter 3

Photoconductive detection

3.1 Introduction

A photoconductive receiver is an essential optoelectronic component in coherent terahertz time-domain spectroscopy which converts the THz field into an electric current. In section 3.2, we present a systematic comparison of electric dipole antennas of different designs. In section 3.3, we describe the development of a high imaging resolution THz spectroscopy based on a near-field photoconductive probe.

A photoconductive receiver generally consists of a short carrier lifetime, high resistivity semiconductor substrate with an overlaid metal antenna, as shown in Figure 3.1 (a). The detection mechanism is based on similar physical principles to those underpinning THz generation. Free electron-hole pairs are excited by a gating laser pulse such that the semiconductor gap bridging the antenna becomes conducting. A THz electric field, parallel to the arms of antennas, will drive a current, which can be measured as a function of the gate delay. The carrier lifetime is arranged to be in the hundreds of femtosecond range so that a signal is only detected when there is temporal overlap between the incident THz pulse and the optical gating pulse. The THz electric field is mapped by varying the arrival time of the gating pulse using an optical delay line.

The fundamental properties of a photoconductive receiver are the response time and the sensitivity. The response time and the gating pulse duration determine the bandwidth that can be measured. For large bandwidth, shorter carrier lifetime and short laser pulses are preferred, although the bandwidth is fundamentally limited by the laser pulse width rather than by the carrier lifetime [1]. LT-GaAs is the most commonly used photoconductor in time-domain spectroscopy [2], because it has the advantages of high mobility μ (high sensitivity) and short carrier lifetime τ (low noise).

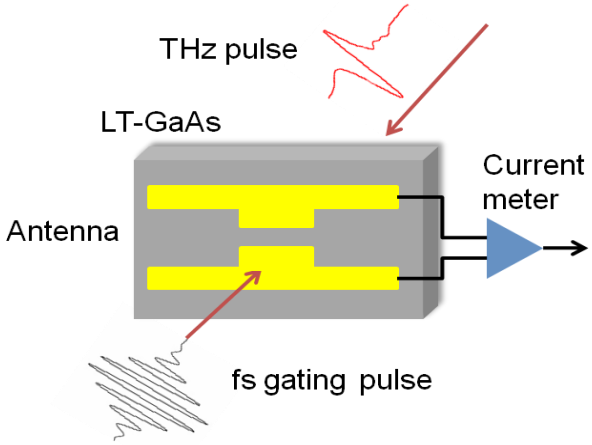

Figure 3.1. Schematic diagram of the photoconductive receiver. The laser pulse excites free carriers in the photoconducting gap and the incident THz electric field generates a net current.

Our photoconductor is typically ~1 μm thick expital layer of low temperature (LT) GaAs on a semi-insulating (SI) substrate with an intervening 100 nm layer of AlAs. A carrier trapping time of 0.4 ps and a mobility of 3000 cm^2/Vs were measured in optical pump-THz probe experiments [3].

The dynamic range is determined by the ratio of peak to peak signal amplitude to root-mean-square (RMS) noise amplitude in unit bandwidth. The peak to peak signal amplitude is proportional to the photoconductivity, $\sigma = n_0 e\mu$, where n_0 is the initial number of free carriers. The RMS current is dominated by the thermal (Johnson) noise and is given by,

$$I_{RMS} = \sqrt{\frac{4k_B T\Delta f}{R}} \propto \sqrt{n_0 \mu\tau} \tag{3.1}$$

where k_B is Boltzmann's constant, Δf is the detection bandwidth, and R is the average illuminated resistance of the photoconducting gap. For our LT-GaAs receivers, the photoconducting gap has a high "off" resistance of 100 MΩ and the dark thermal noise is <100 $fA/\sqrt{Hz}$. The RMS noise was measured by using a lock-in amplifier. With a gating laser power of 20 mW, the average "on" resistance is ~10 MΩ and the RMS noise is typically ~600 $fA/\sqrt{Hz}$.

The gating laser beam also generates a photocurrent in the absence of a THz field, which is attributed to asymmetry in the Schottky barriers of the metal-semiconductor contacts. The magnitude of the shot noise due to this current is generally smaller than the thermal noise [4].

The receiver's spectral sensitivity also depends on the geometrical design of the antenna. Dipole antennas are the most commonly used for photoconductive systems. In the next section, we compare four different geometry antennas in terms of sensitivity and bandwidth and explore whether electromagnetic simulations can be used to predict the frequency response.

3.2 Dipole antennas

3.2.1 Bare antenna response

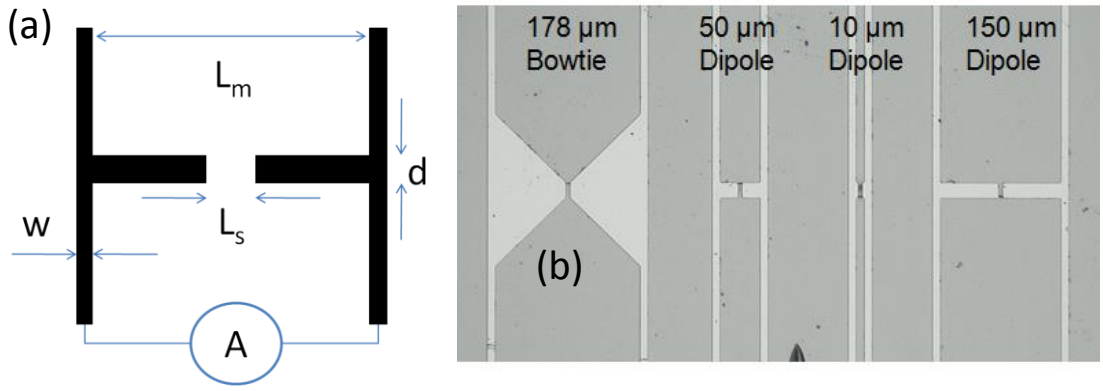

Figure 3.2. (a) Sketch of a typical dipole antenna. (b) Microscope image of four antennas on LT-GaAs.

Over 20 years ago, Smith *et al* [5] demonstrated an efficient THz dipole antenna for time-domain measurements with good bandwidth. The structure is shown in Figure 3.2 (a). The antenna can be considered equivalent to three serially connected resistors, including two metal electrodes and the photoconductive gap R_s. The electrodes can be neglected because the resistance is much smaller than that of the semiconductor. The resistance of the gap is given by,

$$R_s \approx \frac{\rho_s L_s}{\kappa d} \tag{3.2}$$

where L_s is the photoconductive gap width of 5 μm, κ is the photoconducting layer thickness (the optical absorption depth of the LT-GaAs), and ρ_s is the 'on' resistivity of the gap. The incident THz field induces a potential across the antenna. Ignoring the antenna frequency response, the current is roughly given by,

$$I = \frac{E_{THz} L}{\rho_s L_s} \kappa d \tag{3.3}$$

where $L = L_m + 2w$. We investigated the frequency response of dipole antennas of length L_m = 10, 50, 150 μm dipoles and a 90° bowtie with L_m = 178 μm. The widths d of the dipole arm and w of the transmission lines are 20 and 10 μm, respectively. The antennas were fabricated on the same substrate to avoid any material dependence, as shown in Figure 3.2 (b).

The experimental setup was described in Chapter 2. Initial measurements were carried out without the normally used hyper-spherical silicon substrate lens on the back of the receiver. The roughly focused THz beam spot was several millimetres in diameter, which can be treated like plane wave illumination. A 765 nm gating beam with an average power 20 mW was focused on the photoconducting antenna gap. A conventional SI-GaAs, 50 μm-gap coplanar transmitter was used for the study.

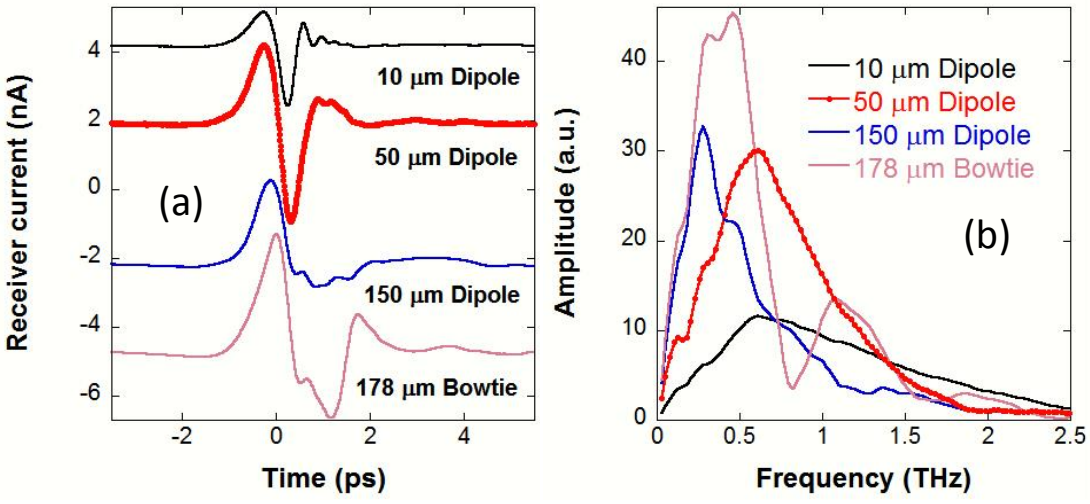

Figure 3.3. Measurements without a silicon lens on back of receiver. (a) Time-domain waveforms from the different antennas (b) Spectra of the waveforms shown in (a).

The time-domain signals for the different antennas are shown in Figure 3.3 (a). The

peak to peak signal (5.9 nA) from the 50 μm dipole is more than twice that from the 10 μm dipole (2.5 nA), partly due to the longer antenna arm L_m. The low (3 nA) peak to peak signal from the 150 μm dipole is due to the small bandwidth. For the bow-tie antenna, the amplitude is 6 nA and comparable to that for the 50 μm dipole.

The spectra of the 10, 50, 150 μm and bow-tie antennas are plotted in Figure 3.3 (b). The bandwidth of the 10 μm antenna is considerably broader than the others, stretching from about 0.1 to 2.5 THz. The 10% amplitude bandwidth for the 50 μm dipole and bowtie are both about 1.5 THz.

For a broad enough transmitter spectrum, the maximum current should be induced at the first resonant frequency and is given by [6],

$$\nu = \frac{c}{2L\sqrt{\varepsilon^*}} \tag{3.5}$$

where ε^* is the effective permittivity, c is the speed of light in vacuum, and the effective antenna length is $L = L_m + 2w$. The effective permittivity should lie between the air and the substrate permittivity. If a uniform GaAs substrate is taken into account for calculation, i.e. $\varepsilon^* = 13$, the calculated peak frequencies are 0.59 THz and 0.25 THz for 50 and 150 μm dipoles, respectively, and are in reasonable agreement with experiments. However, the calculation predicts 1.4 THz for the 10 μm dipole, which does not agree with the measured peak at 0.6 THz, possibly because the effective antenna length is larger than L. The finite length bowtie antenna has same feature of a dipole, with a resonance at 0.42 THz.

3.2.2 Antenna with substrate lens

A refractive index-matched high-resistivity hyper-hemispherical silicon lens was placed on the back of the receiver substrate with a thin intervening layer of paraffin oil, as shown in Figure 3.4. The lens is designed to focus the collimated THz wave onto the antenna gap. For a collimated incident beam, the specific design is given by,

$$h = R\frac{n}{n-1} \tag{3.6}$$

where h is the lens height, R is the radius, and n is the Si refractive index of 3.42.

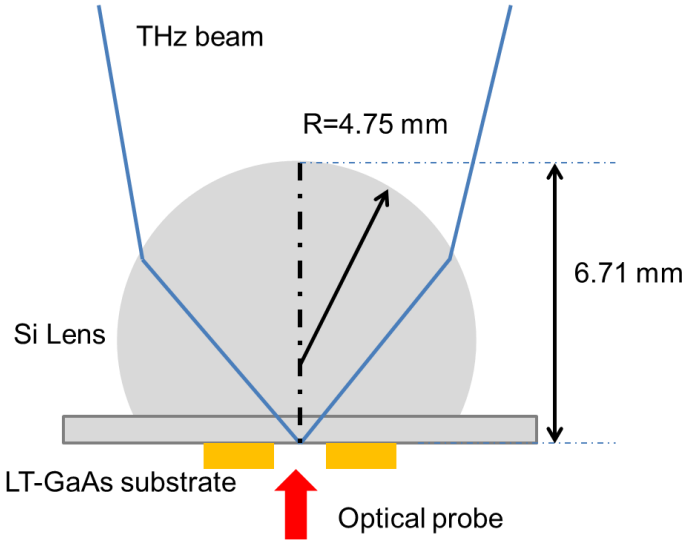

Figure 3.4. A hyper-hemispherical silicon lens attached to the receiver substrate for focusing THz radiation.

Figure 3.5 (a) shows time-domain waveforms measured with the silicon lens. It is noticeable that the shapes are very different from those measured without the silicon lens. The signal amplitudes are more than 20 times larger and 100 nA or more (peak to peak) for all antennas. Figure 3.5 (b) shows that the spectra are also altered by the silicon lens. For the 10 μm dipole, the peak frequency shifts up to 1.0 THz and the bandwidth increases to 3 THz. The enhancement of higher frequency components is due to the THz focal spot diameter's inverse dependence on frequency.

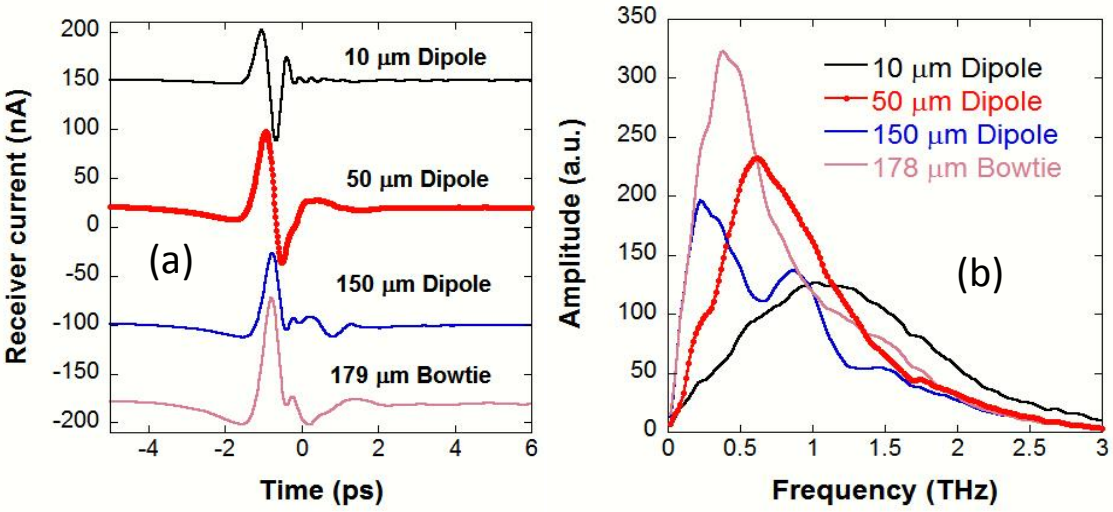

Figure 3.5. Measurements with silicon lens on back of receiver. (a) Time-domain THz waveforms from the different antennas on the same piece of LT-GaAs substrate (b) Spectra corresponding to the waveforms of (a).

3.2.3 Simulation and measurement comparison

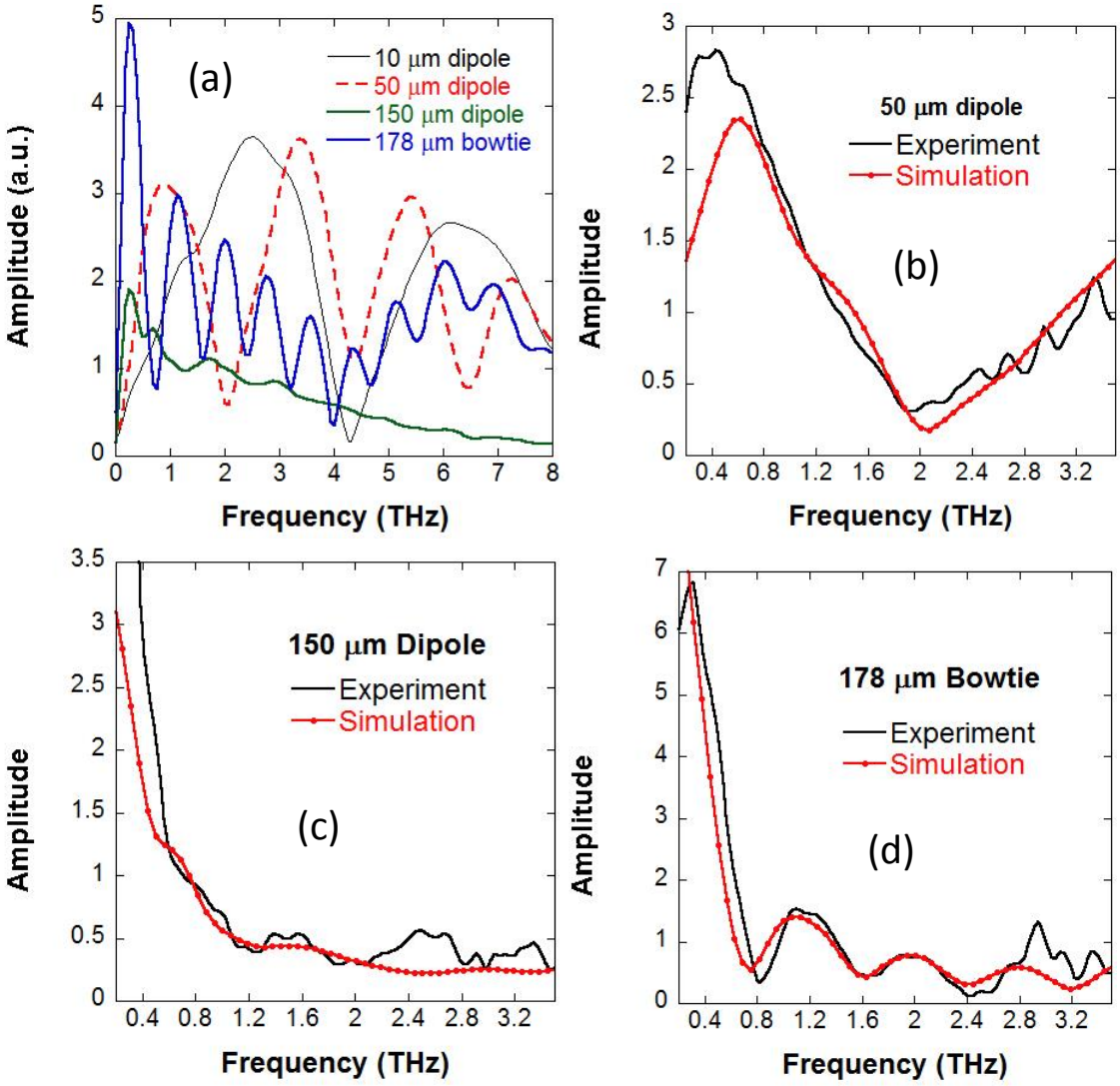

Figure 3.6. (a) Simulation results of the raw antenna responses. The ratio of the frequency response of other antennas to the 10 μm dipole antenna without the substrate Si lens (b) 50 μm dipole (c) 150 μm dipole and (d) 178 μm bowtie.

To understand the influence of antenna design, we have performed simulations using the commercial finite element modelling CST Microwave Studio for solving Maxwell's equations. The simulations use the finite integration technique in the time domain [7]. A dipole receiver was constructed with identical dimensions to the real structures and the simulation volume of $1\times1\times0.5$ mm^3 was divided into 80 million mesh cells. The active photoconductive gap volume was $5\times5\times1$ μm^3 and was treated with a plasma angular frequency of 2×10^{14} rad/s and a scattering time of 55 fs. The metal was treated in the perfect electric conduction (PEC) approximation. A plane wave used for the excitation

and a probe was placed in the middle of the gap to record time-domain signals. The silicon substrate lens was not included in the simulations.

Figure 3.6 (a) presents our simulation results over a frequency range larger than the measurements. The first resonant peak is at 2.47 THz for the 10 μm dipole and at 0.84 THz for the 50 μm dipole. Due to the poorly known incident spectrum in experiment, a quantitative comparison between simulation and measurements can only be made by dividing receiver responses. Consequently, we divided the spectra of the 50, 150 μm and bow-tie devices to that of the 10 μm dipole antenna. It is noted that the frequency components beyond 3.5 THz in the experiment are not reliable since noise dominated at these frequencies. Figure 3.6 shows good agreement between the simulations and measurements. This shows that the computer model provides an accurate picture of the bare antenna response and could be used to design new antennas with tailored response.

3.3 Near-field THz Photoconductive Probe

3.3.1 Near-field detection

Diffraction limits the spatial resolution of conventional THz spectroscopy to a few hundreds of micrometres. To improve the image resolution, radiation can be detected in the near field region of samples. Currently, there are two main techniques: electro-optic sampling with focused probe beam and photoconductive detection with integrated aperture.

Electro-optic sampling exploits the Pockels effect, where the incident THz electric field induces birefringence in an electro-optic material, like ZnTe [8]. The THz field is detected by measuring the change in polarization state of a femtosecond probe pulse. As detection occurs at the probe focus, near-field information can be obtained by placing the sample close to the focus. The spatial resolution is determined by the laser spot size and depth of field, and is typically about 10 μm [9].

The integrated aperture near-field photoconductive (PC) probe is a concept borrowed from near-field scanning optical microscopy (NSOM) [10]. At optical frequencies, a silver coated optical fibre with a tip window of tens of nanometres wide is placed close

to objects and collects and deliveries light in the near-field [11]. At terahertz frequencies, an opaque screen with a subwavelength aperture is placed a few micrometres in front of photoconductive antenna to improve the spatial resolution. The electric field at the aperture can be mapped by moving the receiver and aperture together. The resolution is determined by the size of the aperture and not the incident wavelength. In our work, we used this type of near-field PC probe.

There are some other near-field imaging techniques at THz frequencies. A dynamic aperture can be achieved with an optical gating beam focused on a semiconductor. The spatial resolution fundamentally depends on the spot size of the optical gating bean and the thickness of the semiconductor but this technique is very specialized [12]. Another example is a sharp metal needle that can scatter the THz field at the micro tip. The scattered field can be detected in far-field [13]. The concept is similar to the apertureless NSOM. This technique has a low sensitivity in time domain measurements.

3.3.2 Hollow-core fibre-coupled TDTS

A fibre coupled THz-TDS system was used to study the near-field probe and THz waveguides. This system was similar to the free-space THz-TDS system described in Chapter 2, except that the laser pulses are delivered to THz photoconductive devices via hollow-air-core photonic crystal fibres (HC-PCF) instead of free space, as illustrated in Figure 3.7.

Ti:sapphire femtosecond laser pulses pass through an optical isolator to prevent feedback to the laser. The central wavelength is chosen to be 775 nm where the dispersion of the fibre compensates that of other optical components. The laser beam is then divided into two parts for generation and detection. In order to match the 0.2 numerical aperture of HC-PCF [14], a beam expander and ×20 objective lens are used in each beam path. Half-waveplates are used to minimize the effect of the unintentional birefringence of the fibre arising from artefacts for the fabrication. The coupling efficiency from free space to the fibre output can reach 60%.

The pump beam is mechanically chopped at 2.5 kHz for lock-in detection. A fast scanning retro-reflector allows us to obtain a full THz signal in real time on an

oscilloscope. An average power of 35 mW (chopped) is used for THz generation. The output from the fibre is collimated and then focused on to a photoconductive transmitter. The transmitter is a conventional 50 µm coplanar transmitter on LT-GaAs substrate. The probe laser pulse can be used to gate either a conventional receiver or a near-field probe by flipping a mirror in the beam path as shown in Figure 3.7. The optical gating power for the far-field receiver is 20 mW and 8 mW for the near-field probe. The probe gating power is limited because an epoxy glue was used during the device fabrication and excessive optical heating leads to device failure.

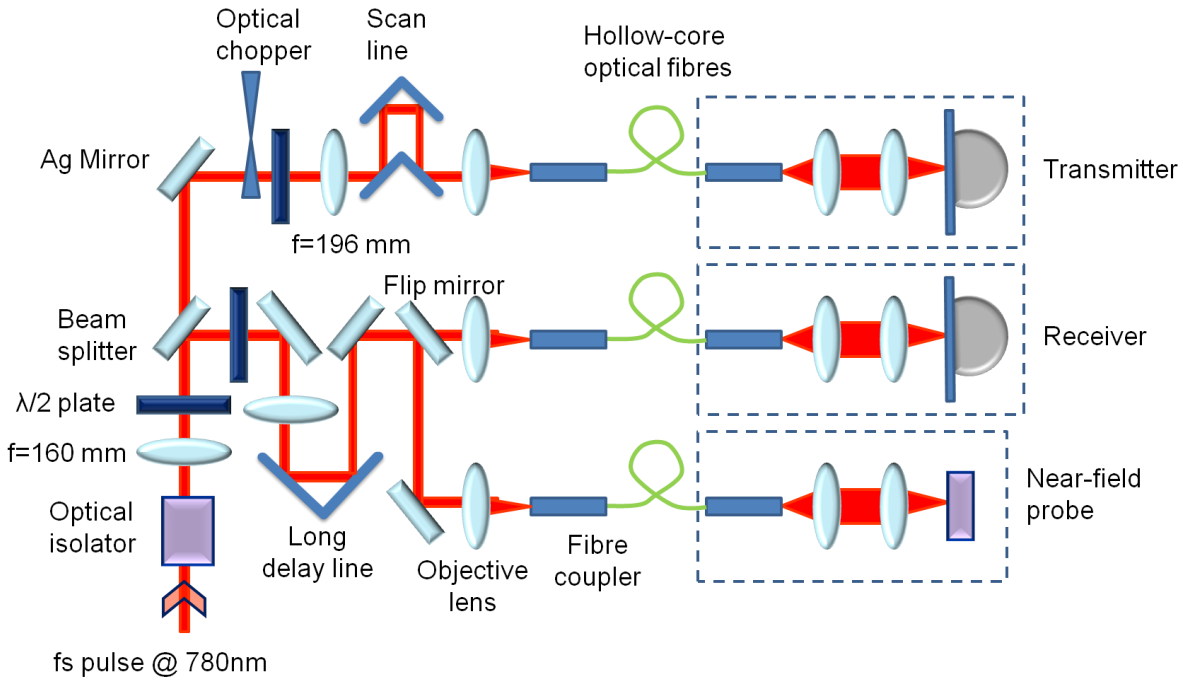

Figure 3.7. Schematic of fibre-coupled TDTS setup.

Fibre coupling offers the maximum flexibility for studying samples, such as parallel plate waveguides and metamaterials, since changes in geometry do not require complicated schemes for maintaining optical alignment and delay. HC-PCF is better than a conventional solid core fibre because it has negligible optical nonlinearity and its negative GVD can be used to compensate positive dispersion from the optical isolator and lenses. We used this system for our experimental studies of waveguides, which will be discussed in Chapter 4, 5 and 6.

3.3.3 Transmission through an aperture

We firstly studied the transmission through an aperture with size similar to the incident wavelength, as shown in Figure 3.8. The aperture was made from a 50 μm thick brass sheet and placed ~2 cm in front of a conventional receiver's silicon lens. Since the substrate silicon lens is designed for focusing collimated THz radiations, a high resistivity silicon wafer with 600 μm thickness was inserted between the Si lens and the receiver to improve the beam collection efficiency.

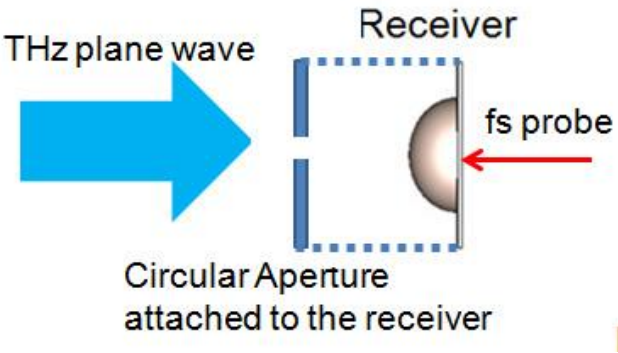

Figure 3.8. Sketch of a simple THz imaging setup with a circular aperture in front of the receiver silicon lens to improve the spatial resolution.

A plane THz wave was launched towards the aperture. The signals transmitted through 300- and 500-μm-diam circular apertures are similar to the directly measured plane wave as shown in Figure 3.9 (a). The peak to peak amplitudes are 250 and 780 pA, respectively. The cutoff frequency for the TE_{11} mode of an infinitely long circular metal waveguide is given by,

$$v_c = \frac{p_{11}}{\pi d\sqrt{\varepsilon\mu}} \tag{3.7}$$

where ε and μ are the permittivity and permeability of the filling dielectric, and d is the diameter of the aperture. The constant p_{11} has the value 1.841 [6]. The calculated cutoff frequency of the 300 μm round aperture is 0.59 THz. However, Figure 3.9 (b) shows that the frequency components below 0.35 THz just begin to be filtered by the 300-μm-diam aperture, which might be attributed to the fact that the metal is only 50 μm thick. Detection with the 300 μm aperture is used for our studies on dielectric waveguides in Chapter 5.

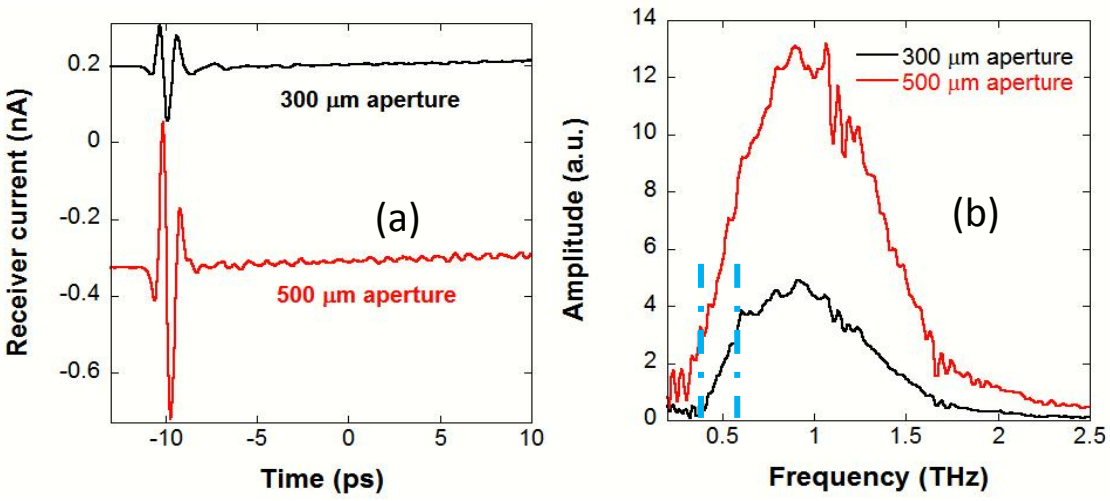

Figure 3.9. (a) Time-domain signal of the far field receiver with two different circular apertures. The aperture is a mechanically drilled hole in a solid brass sheet (50 μm thickness). (b) The corresponding spectrum of the transmitted signals. The blue dashed line shows calculated cutoff frequencies.

The electric field behind an illuminated small aperture has both propagating and non-propagating components and depends on the aperture diameter d, distance from the aperture z, and wavelength λ. Below the cutoff frequency, Bethe and Bouwkamp [15, 16] arrived at an analytical solution for the transmission coefficient of a circular aperture in an infinitely thin perfect conductive sheet, as $T \propto k_0^2 d^3/z^2$ at distance $z \gg \lambda$, where d is the aperture size. In the very near field $z < d$, the electric field amplitude is independent of λ and given by [17],

$$E(z) = e^{-(\frac{z}{\gamma d})} \tag{3.8}$$

where γ is a numerical factor and approximately equals to 0.55. A near-field measurement should use a detector in the very near field zone when the wavelength is larger than the hole diameter.

3.3.4 Near-field probe fabrication

It is feasible to improve the spatial resolution in THz time-domain spectroscopy using much smaller apertures than described in section 3.4.3. However, the limitations are the strong attenuation of the pulse propagating through the aperture (amplitude $\propto d^3$), and the high cutoff frequency for a subwavelength aperture ($v_c \propto d^{-1}$). In order to resolve

the problems, one has to measure the electric fields just behind the aperture in the very near-field region less than *d* away from the aperture.

From the practical point of view, the photoconductive antenna has to be positioned as close as possible to the sample to achieve high spatial resolution. Silicon on sapphire receivers can be used by placing the antenna close to samples [18, 19], whilst the laser gate beam enters through the back of the sapphire substrate. This approach relies on the small affective antenna area. A better solution is to integrate an aperture. A THz near-field probe with an integrated aperture was first developed by Mitrofanov *et al* [20, 21]. As the fabrication techniques are challenging, only a few groups have replicated this approach [22]. Here, we introduce our version of the near-field probe (NFP) and describe its fabrication processes.

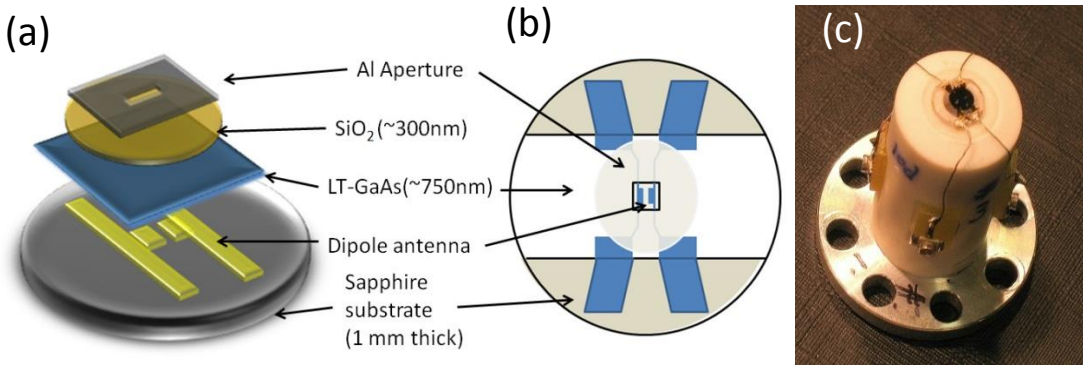

Figure 3.10. (a) Three-dimensional view of the near-field probe structure (b) Schematic diagram of top view of the terahertz near-field probe. Blue areas indicate the deposited metal of the antenna on polished bevels of sapphire (grey areas). (c) Picture of NFP mounted on a ceramic holder with integrated focusing lens.

A schematic diagram of the near-field probe is shown in Figure 3.10. The photoconductor used was LT-GaAs of ~1 μm thickness, epitaxially grown on a thin buffer layer of AlAs (~100 nm) on top of a SI-GaAs substrate (~600 μm). The metal antennas were firstly fabricated on top of the LT-GaAs by standard photolithography, thermal evaporation and lift-off processes and then glued face down onto a sapphire substrate using ultraviolet light curing epoxy adhesive. The glue layer must be cured under pressure to minimize its thickness and thermal resistance. Then, the majority of the GaAs substrate (>500 μm) was removed by wet etching (H_4SO_2:H_2O_2:H_2O = 8:10:100). A selective plasma etching technique using a mixture of $SiCl_4$ and SF_6 was then used to remove the remaining SI-GaAs substrate. This process was designed to

stop at the AlAs buffer layer with a high selectivity, leaving a mirror like surface. The sacrificial AlAs layer was later etched away using dilute HF to leave the LT-GaAs layer on the sapphire substrate. Then a circular protective layer of photoresist was coated on the LT-GaAs and wet etching was performed to expose contact pads at the edge, leaving a central 3 mm diameter disc of LT-GaAs.

In order to make electrical connections, the edges of the sapphire substrate were polished by hand to create a 45^{o} bevel. 600 nm thick Ti:Au contact pads were thermally deposited on the bevel so as to overlap with the exposed antenna contact pads. Before the deposition of the final 300 nm thick aluminium mask defining the aperture, an insulating layer of SiO_2 was electron beam evaporated and wet etched to expose the contacts again. Each device contains two antennas with apertures accurately centred over the photoconducting gaps. The both antenna dipoles are 10 μm long and the square apertures are typically 20 and 50 μm respectively.

The devices were mounted on a ceramic holder, as shown in Figure 3.10 (c). Thin copper wires were used for the electrical connection. The base was attached to a fibre coupler and mounted on a 3-axis motorised stage with position encoders.

3.3.4 Free-space characterization of near-field probe

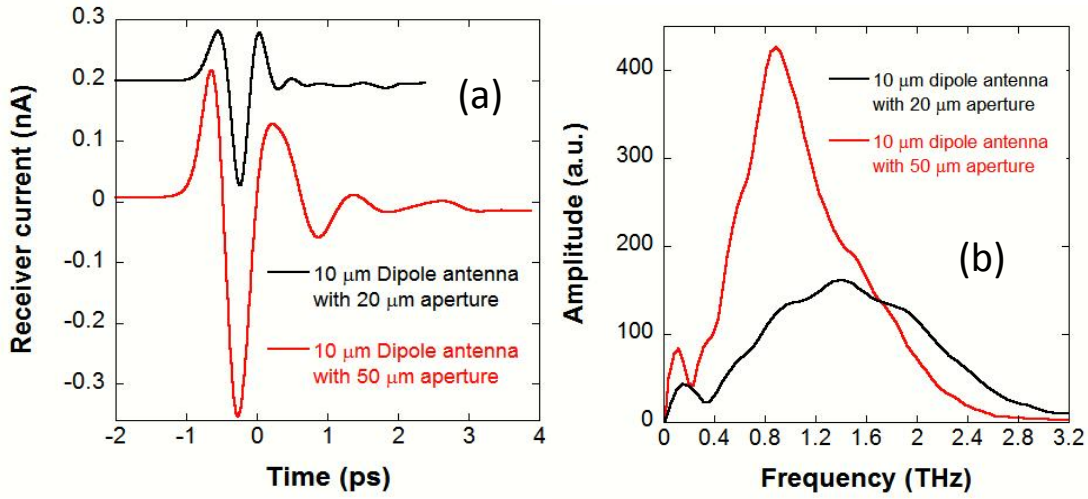

Figure 3.11. (a) Near-field probe time-domain responses with 10 μm dipoles and two different apertures. (b) The corresponding spectra.

Near-field probes were tested using the fibre-coupled time-domain spectrometer. THz

radiation was emitted from a conventional 50 μm LT-GaAs coplanar photoconductive antenna with a substrate lens and then collimated and focused using a pair of off-axis parabolic mirrors with 7.62 cm focal length. The focal plane was found with the minimal FWHM of the THz beam and the maximum amplitude.

For our antennas with 50 and 20 μm apertures, the calculated cutoff frequencies for the TE_{10} mode of a rectangular waveguide are 1.13 THz and 2.83 THz respectively, given by $f = 1/2d\sqrt{\mu\varepsilon^*}$, with the effective dielectric constant of $\varepsilon^* = \varepsilon_0(\varepsilon_r + 1)/2$, where ε_r is the GaAs relative permittivity of ~13. Figure 3.11 (a) shows the measured signals, which are single cycle-like pulses, similar to those obtained with a conventional far-field receiver. The peak to peak amplitude with the 50 μm aperture is about 550 pA, slightly more than double that with the 20 μm aperture (~250 pA). The spectra of the time-domain signals are shown in Figure 3.11 (b) and display spectral response up to 2.5 and 2.0 THz for 20 and 50 μm apertures, respectively. The enhanced higher frequency response with the smaller aperture can be attributed to the frequency dependent aperture transmission.

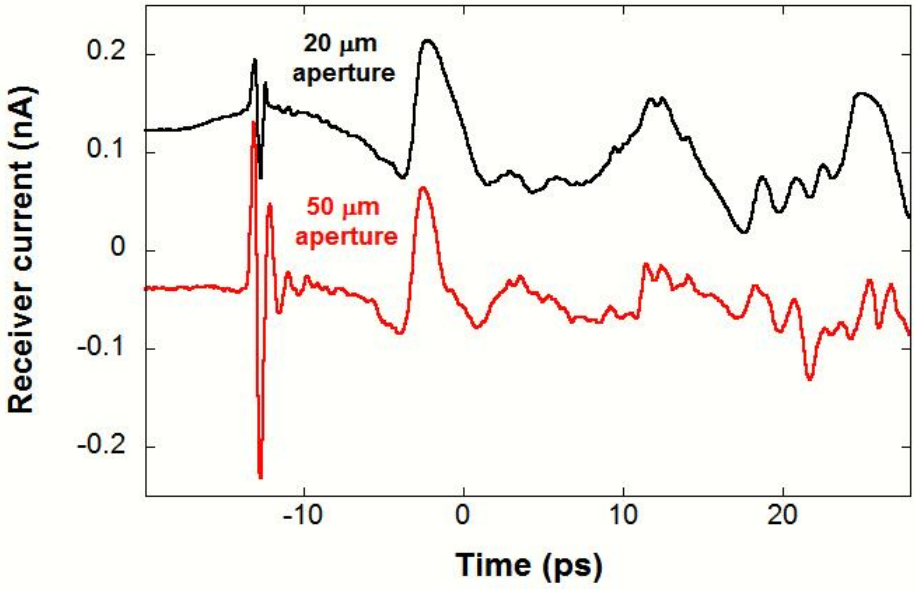

Figure 3.12. The near-field probe signal measured on a long time-scale, showing the artefact traces involving the utilization of the probes.

Although the main purpose of the integrated aperture is to improve spatial resolution, it also plays a role in cleaning up unwanted signals immediately preceding and following the main pulse. Nevertheless, there are still low frequency artefacts after the main peak,

as shown in Figure 3.12. The background signals at the time of +12 ps are due to the large incident beam reflected back from the sapphire and the aluminium aperture. Given the sapphire ordinary refractive index of ~3.1 and thickness of 1 mm, the corresponding time delay is associated with the thickness of the substrate. The signals at the time of -3 ps are similar in amplitude and bandwidth, although they are measured with different apertures. It is probably due to light guided at the aluminium-sapphire interface. The aluminium screen is 1 mm from the centre to edge, which accounts for the time delay of about 10 ps. These artefacts could be displaced to larger delay by increasing the thickness of the sapphire substrate and the size of the aluminium screen.

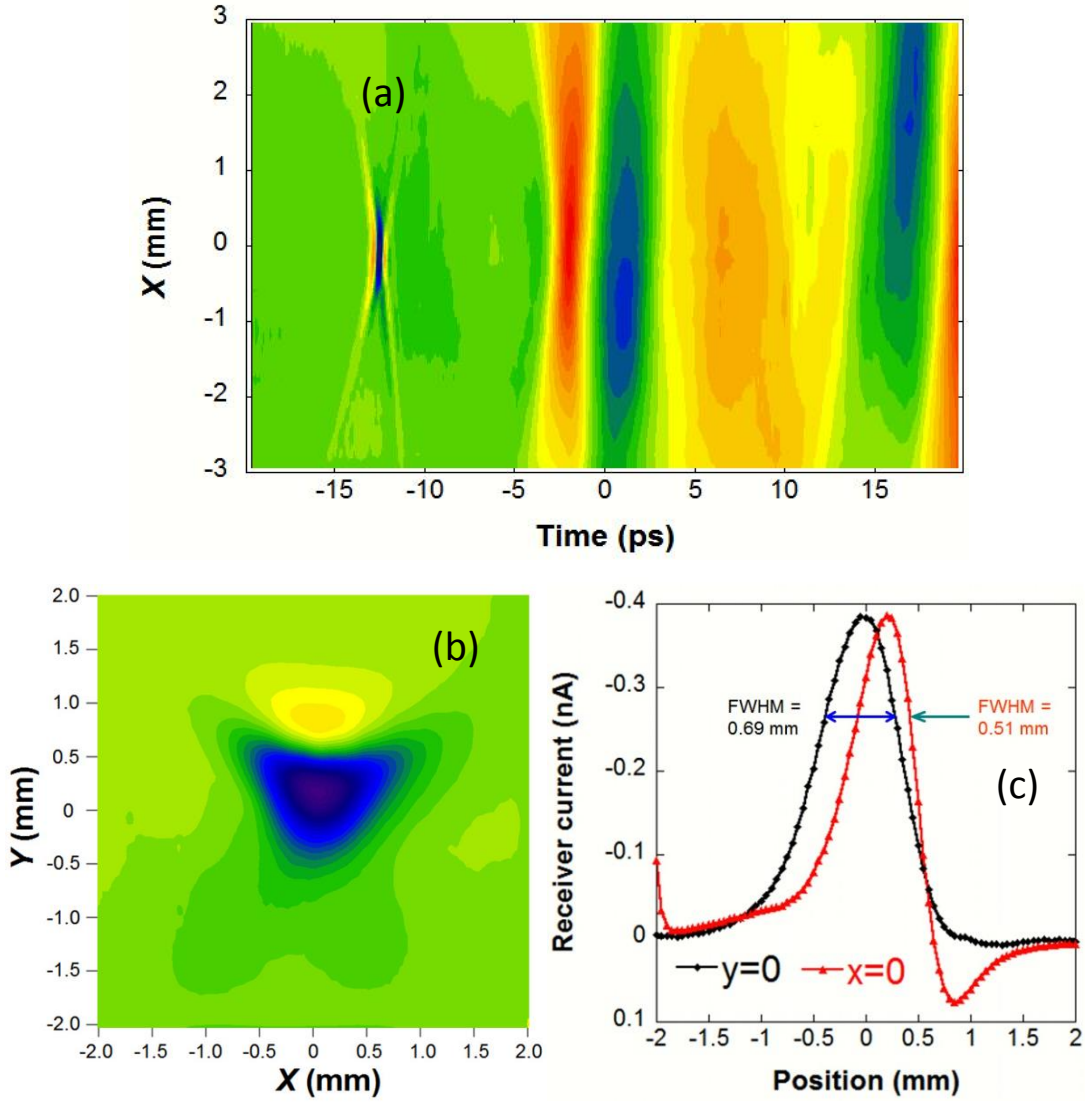

Figure 3.13. (a) Spatial-temporal field profile of time-domain signals measured along the x axis by a 10 μm dipole with a 50 μm aperture. Red indicates positive electric amplitude and blue negative. (b) Two-dimensional field map at a fixed delay corresponding to the maximum negative electric field at -12 ps. (c) Line profiles extracted the 2D map.

A simple imaging application of the NFP is to characterize the THz beam profile in the focal plane of the off-axis parabolic mirror. Figure 3.13 (a) shows the spatial-temporal field map along the x axis measured with the 10 μm dipole antenna with 50 μm aperture. The signal near -13 ps delay is the main THz pulse and is highly concentrated near zero along the x axis. The signal at -3 ps extends over a much larger length scale and is associated with the artefacts of mentioned above.

We measured the 2D field distribution by choosing a fixed time-delay corresponding to the largest negative peak of the THz electric field on the optical axis. Figure 3.13 (b) shows that the beam profile has approximate mirror symmetry about x = 0 but is asymmetric, with opposite polarity for larger ±y, about y = 0. The focal beam shape is attributed to aberrations of the off-axis parabolic mirrors [23]. The line scans shown in Figure 3.13 (c) provide estimates of the FWHM of the beam size, which is 0.69 mm along x and 0.51 mm along y, respectively. These values are close to the diffraction limit at 1 THz, given by Eq (2.5). A beam diameter of 3.4 cm and a focal length is 7.62 cm give a calculated 1/e spot size of ~0.86 mm and a FWHM of ~0.51 mm, although the focal spot size increases with lower frequency [24].

3.3.5 Near field probe limitations

The photoconductive near-field probe must be placed in close proximity to an object (a few tens of micrometres) to collect evanescent waves and obtain good spatial resolution. The ultimate resolution is roughly the sum of the aperture size and the distance from the object, although in practice this is greatly dependent on the structure and THz polarization. For example, a z-polarized wave can be generated by diffraction at metal edge and propagate in the air space between the sample and the probe [25]. These waves can be detected by diffraction at the probe dipole and aperture and contribute to the signal. The artefact affects the near-field applications discussed in Chapter 4.

The small probe-sample separation also causes a few operational problems. Extreme care has to be taken because the probe can be damaged by contact with samples. Achieving parallelism between the sample plane and the probe scanning plane is also critical to avoid changes in signal strength and resolution due to changes in sample-probe separation.

3.4 Conclusions

We have experimentally and numerically compared four different geometry photoconductive antennas in terms of bandwidth and sensitivity. Simulations performed with CST Microwave Studio showed good agreement with measurements made without a hyper hemispherical silicon substrate lens. The study provides a design tool for THz antennas.

We also designed and fabricated a photoconductive near-field antenna with an integrated subwavelength aperture. We incorporated the THz near-field probe into a fibre-coupled THz spectrometer and characterized the beam profile at the focus of a parabolic mirror. The high resolution images show that the focal spot size is close to the diffraction limit. Since THz waves can propagate in the gap between the probe and sample and be detected, images must be interpreted carefully. The results in this chapter provide the basic knowledge required to use the probe to study THz waveguides as described in the next chapter.

References

1. T. A. Liu, M. Tani, M. Nakajima, M. Hangyo, and C. L. Pan, "Ultrabroadband terahertz field detection by photoconductive antennas based on multi-energy arsenic-ion-implanted GaAs and semi-insulating GaAs," Applied Physics Letters **83**, 1322-1324 (2003).

2. R. S. Elliott and S. E. Robert, *Antenna theory and design* (Englewood Cliffs London : Prentice-Hall, Englewood Cliffs London, 1981).

3. R. Yano, H. Gotoh, Y. Hirayama, S. Miyashita, Y. Kadoya, and T. Hattori, "Terahertz wave detection performance of photoconductive antennas: Role of antenna structure and gate pulse intensity," Journal of Applied Physics **97**, 103103 (2005).

4. M. Van Exter and D. R. Grischkowsky, "Characterization of an optoelectronic terahertz beam system," IEEE Transactions on Microwave Theory and Techniques **38**, 1684-1691 (1990).

5. P. R. Smith, D. H. Auston, and M. C. Nuss, "Subpicosecond photoconducting dipole antennas," IEEE Journal of Quantum Electronics **24**, 255-260 (1988).

6. D. M. Pozar and M. P. David, *Microwave engineering* (New York Chichester : Wiley, New York Chichester, 2004).

7. CST MICROWAVE STUDIO, Computer Simulation Technology GmbH, Darmstadt, Germany.

8. Q. Wu and X. C. Zhang, "Ultrafast electro-optic field sensors," Applied Physics Letters **68**, 1604-1606 (1996).

9. A. Bartels, A. Thoma, C. Janke, T. Dekorsy, A. Dreyhaupt, S. Winnerl, and M. Helm, "High-resolution THz spectrometer with kHz scan rates," Optics Express **14**, 430-437 (2006).

10. A. Lewis, M. Isaacson, A. Harootunian, and A. Muray, "Development of a 500 A spatial-resolution light-microscope: I. Light is efficiently transmitted through λ/16 diameter apertures," Ultramicroscopy **13**, 227-231 (1984).

11. V. Sandoghdar, S. Wegscheider, G. Krausch, and J. Mlynek, "Reflection scanning near-field optical microscopy with uncoated fiber tips: How good is the resolution really?," Journal of Applied Physics **81**, 2499-2503 (1997).

12. Q. Chen, Z. Jiang, G. X. Xu, and X. C. Zhang, "Near-field terahertz imaging with a dynamic aperture," Opt. Lett. **25**, 1122-1124 (2000).

13. H. T. Chen, R. Kersting, and G. C. Cho, "Terahertz imaging with nanometer resolution," Applied Physics Letters **83**, 3009-3011 (2003).

14. F. Luan, J. Knight, P. Russell, S. Campbell, D. Xiao, D. Reid, B. Mangan, D. Williams, and P. Roberts, "Femtosecond soliton pulse delivery at 800nm wavelength in hollow-core photonic bandgap fibers," Opt. Express **12**, 835-840 (2004).

15. H. A. Bethe, "Theory of Diffraction by Small Holes," Physical Review **66**, 163-182 (1944).

16. C. J. Bouwkamp, "On bethes theory of diffraction by small holes," Philips Research Reports **5**, 321-332 (1950).

17. S. Mair, B. Gompf, and M. Dressel, "Spatial and spectral behavior of the optical near field studied by a terahertz near-field spectrometer," Applied Physics Letters **84**, 1219-1221 (2004).

18. T. I. Jeon, J. Q. Zhang, and D. Grischkowsky, "THz Sommerfeld wave propagation on a single metal wire," Applied Physics Letters **86**, 161904 (2005).

19. M. Walther, M. R. Freeman, and F. A. Hegmann "Metal-wire terahertz time-domain spectroscopy," Applied physics letters **87**, 261107 (2005).

20. O. Mitrofanov, I. Brener, R. Harel, J. D. Wynn, L. N. Pfeiffer, K. W. West, and J. Federici, "Terahertz near-field microscopy based on a collection mode detector," Applied Physics Letters **77**, 3496-3498 (2000).

21. O. Mitrofanov, M. Lee, J. W. P. Hsu, I. Brener, R. Harel, J. F. Federici, J. D. Wynn, L. N. Pfeiffer, and K. W. West, "Collection-mode near-field imaging with 0.5-THz pulses," IEEE Journal of Selected Topics in Quantum Electronics **7**, 600-607 (2001).

22. M. Waechter, M. Nagel, and H. Kurz, "Tapered photoconductive terahertz field probe tip with subwavelength spatial resolution," Applied Physics Letters **95**, 041112 (2009).

23. M. T. Reiten, S. A. Harmon, and R. A. Cheville, "Terahertz beam propagation measured through three-dimensional amplitude profile determination," Journal of the Optical Society of America B **20**, 2215-2225 (2003).

24. J. M. Dai, S. Coleman, and D. Grischkowsky, "Planar THz quasioptics," Applied Physics Letters **85**, 884-886 (2004).

25. M. Misra, S. R. Andrews, and S. A. Maier, "Waveguide artefacts in terahertz near field imaging," Applied Physics Letters **100**, 191109 (2012).

Chapter 4
Parallel metal plate terahertz waveguide

4.1 Introduction

Metals exhibit high conductivity at THz frequencies and metal waveguides can efficiently guide THz waves and be coupled to using simple quasi-optical techniques [1]. The parallel metal plates waveguide (PPWG) is probably the most important waveguide because it has no cutoff frequency for the fundamental TEM (TM_0) mode, negligible group velocity dispersion over a very large bandwidth and is easily configured for single-mode propagation [2]. In section 4.2, a step within a PPWG is used to couple the TEM mode to a higher-order TM mode. In section 4.3, a PPWG is linearly tapered in 2-dimensions such that the output end has a local aperture of 20 μm × 20 μm. A few mm-size THz beam can be focused down to a deep subwavelength size spot using this structure.

4.2 PPWG with step discontinuity

Higher order guided modes can be excited using edge coupling techniques [3], but in general coupling to odd modes in a conventional PPWG is inefficient. Here, we demonstrated that an integrated step inside the PPWG can allow efficient coupling higher order modes (at least the TM_1 mode) from the TEM mode because of the broken waveguide symmetry.

For a parallel plate waveguide as shown in Figure 4.1, a TEM mode has the electric and magnetic fields given by [1],

$$\bar{E}(r) = -\bar{x}\frac{k_z}{\omega\varepsilon}H_0 exp(-jk_z z) \tag{4.1}$$

$$\bar{H}(r) = \bar{y}H_0 exp(-jk_z z) \tag{4.2}$$

where r is the distance from origin, x, y, z are vectors. k_z is the propagation constant and ε is the dielectric permittivity between the plates. The fields are independent of the x position. The dispersion relation for TM_m guided modes is given by,

$$k_x^2 + k_z^2 = \omega^2\mu_0\varepsilon \tag{4.3}$$

$$k_z = \sqrt{\omega^2\mu_0\varepsilon - (\frac{m\pi}{d})^2}, \quad m = 0,1,2,3,.... \tag{4.4}$$

where d is the plate separation. The cutoff frequency of the TM_m mode is given by,

$$\omega_m = \frac{1}{\sqrt{\mu_0\varepsilon}}\frac{m\pi}{d} \tag{4.5}$$

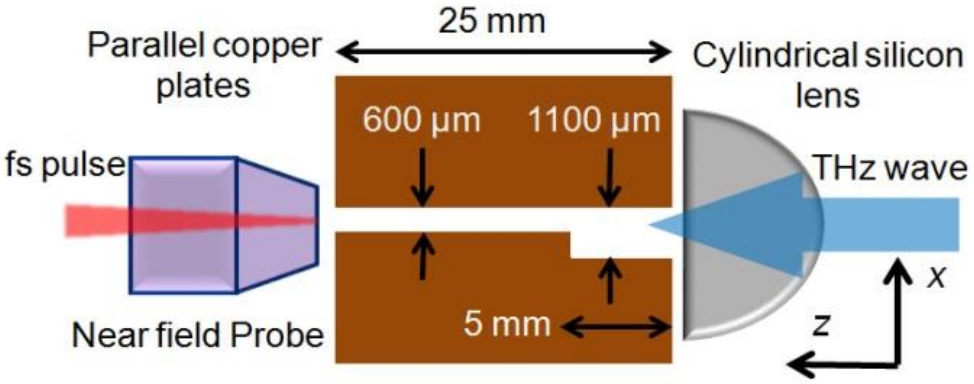

Figure 4.1. Schematic of experimental setup

Figure 4.1 shows the configuration of the experiment and the air spaced brass waveguide. One plate has a flat surface, whilst the other has a 5 mm long and 500 µm deep step. The output end plate separation is ~600 µm. A cylindrical silicon lens was used to couple in plane THz waves. The entrance and exit faces of the PPWG were hand-polished to allow the near-field probe to closely approach the sample (20~30 µm). The near-field probe in this case was a 50 µm dipole antenna with an integrated 50 µm square aperture, as described in Chapter 3.

The near-field probe was scanned along the x axis to produce the amplitude map in Figure 4.2 (a), which shows the variation of the output field with time-delay and position. In this figure, one can see that the time of the peak signal is constant in the waveguide gap but the delay increases dramatically once the probe is outside the gap region. The propagation velocity in this region was measured as ~0.286 mm ps^{-1}, close to *c*. A similar phenomenon was observed but not explained ten years ago [4], but recently our group provided an explanation in terms of a waveguiding artefact [5]. In brief, the output field from the PPWG gap can be diffracted into the small gap between the metal screen of the near-field probe and the end face of the PPWG. The receiver dipole antenna is only sensitive to the linearly polarized electric field parallel to the dipole length along the x axis but the probe aperture can scatter the guided wave to generate an additional component along the x axis, which is detected by the probe. Similar detection artefacts will be seen again in section 4.3 and discussed in more detail.

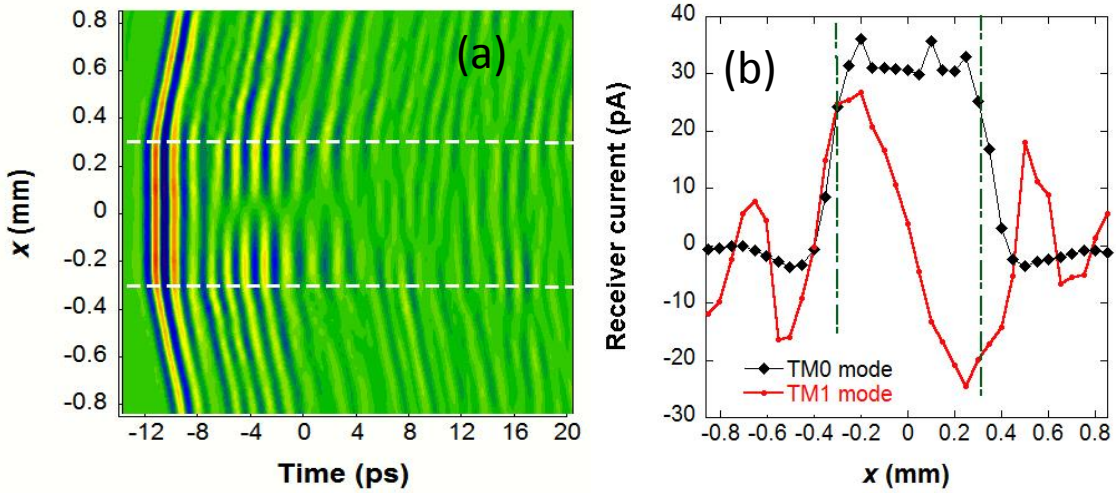

Figure 4.2. (a) Spatial amplitude map at y = 0 for the PPWG, showing time dependence of amplitudes versus near field probe position at the output end of the PPWG. Red colour indicates the positive field, blue negative and green zero. The space between the two white dashed lines is the air gap. (b) Cross section through the time-domain spatial amplitude map at fixed delays of -11 ps (black dot curve) and -4 ps (red dot curve).

Figure 4.2 (b) shows the peak receiver current along x at a fixed delay of -11 ps. The field profile shows a flat-top distribution across the waveguide gap, characteristic of the TEM mode. The small negative signals at x = -0.5 and 0.5 mm are due to the

waveguide artefacts. The initial TEM mode can be partially transformed into higher order modes at the step discontinuity. This can be seen at a time delay of -4 ps when the signals are asymmetric with maximum amplitudes but opposite polarity at x = -0.22 and +0.2 mm and zero amplitude at the centre of the waveguide, characteristic of a TM_1 mode. The signals for |x| > 0.3 mm are again due to waveguide artefacts. The TM_1 mode is broadened by several ps due to group velocity dispersion near the cutoff frequency.

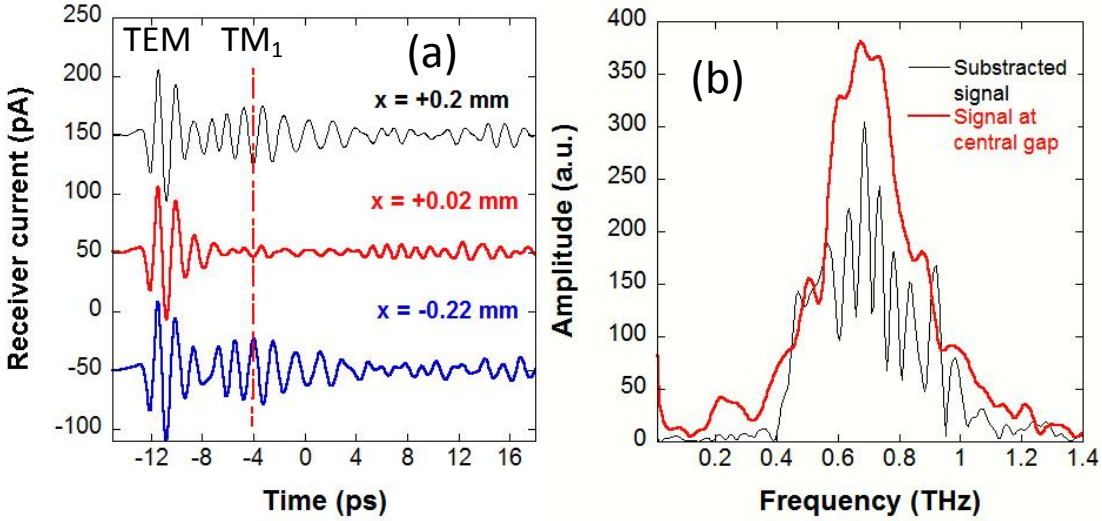

Figure 4.3. (a) PPWG time-domain signal at three different x positions of the probe. (b) Comparison of the spectra of TM_0 and TM_1 modes. The cutoff frequency is clearly seen in 0.4 THz.

Figure 4.3 (a) shows the time-domain signals at three different positions in the air gap. The TM_1 mode is in the time domain signals from -7 to 4 ps, because the sign of signals at x = +0.2 and -0.22 mm is reversed. There are probably other higher order modes, e.g. TM_2 mode at a time delay of +8 ps in Figure 4.2 (a), although the amplitude is too weak to confirm their existence.

In order to obtain the higher mode spectrum, we subtracted the time-domain signal at zero position from the signal at x = +0.2 mm to eliminate the TEM mode signal before -7 ps. The Fourier-transformed spectrum shows a cutoff frequency of 0.4 THz, compared with the broadband transmission of TEM mode in Figure 4.3 (b). For the air-filled waveguide, according to Eq (4.5), the cutoff frequency is 0.25 THz with d = 0.6 mm, which is smaller than that measured.

4.3 Subwavelength focusing by a tapered PPWG

4.3.1 Introduction

Light concentration via tapered waveguiding is a route to achieving intense radiation for point-source-like illumination in near-field micro-spectroscopy and for enhanced light-matter interactions in nonlinear optical investigations [6, 7]. In THz time domain measurements, dielectric loss and dispersion are serious problems so that effort has concentrated on low loss and broadband waveguiding and sub-wavelength focusing concepts using metal structures. Examples include a conically tapered aperture [8], conical coaxial waveguide [9], tapered wire [10] and tapered parallel plate [11]. In particular, the tapered parallel plate waveguide (TPPWG) has recently been used to transport THz radiation with subwavelength lateral confinement. A similar structure, but with sapphire replacing the air gap, has also been explored for THz microscopy [12], but introducing the dielectric gives rise to strong dispersion. The TPPWG has advantages over the tapered cylindrical aperture because there is no cutoff frequency and it is easier to fabricate than the cutoff free tapered coaxial guide. Moreover, compared to open propagation on tapered wires, it is less affected by external perturbations.

Our aim in this work was to explore some of the issues that need to be addressed when considering practical applications of the air-filled TPPWG. We describe a numerical and experimental study of beam propagation from the TPPWG into the space surrounding the effective aperture. Simulations of beam divergence and coupling efficiency into free space are compared with the results of near field imaging using a photoconductive near-field probe. We clarify the nature of the guided mode and identify the effect of geometry (tapered metal angle) on the efficiency of energy transfer from the input to the guide to the near field at the output. The study provides an insight into the beam propagation process.

4.3.2 Numerical simulations

The waveguide geometry shown in Figure 4.4 (a) consists of a pair of 1 mm thick

tapered metal plates extending 2 cm along the z axis and 1.0 mm thick with narrowest width $w(z = 0)$ = 20 μm. The plates surrounds a tapered air gap with width $d(z = 0)$ = 20 μm at the narrowest point. The air angle, θ_a, is 1.25° and the metal angle, θ_m, is 2.5°.

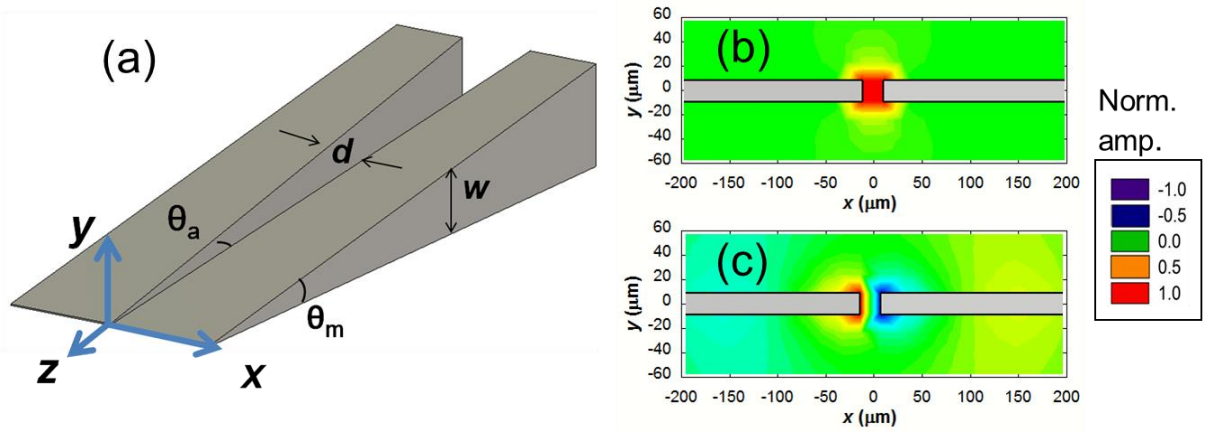

Figure 4.4. (a) Schematic of the tapered PPWG. (b) Simulated average electric field along the x axis (E_x) and (c) electric field along the z axis (E_z) at 1.0 THz at the position z = 0.

In the time domain simulations, an x-polarised plane wave was used for the input field. This wave travels a short distance (<0.5 mm) before transforming into the fundamental TEM-like waveguide mode. The time average E_x field distribution at z = 0 is shown in Figure 4.4 (b). It is highly confined in the air gap region and slightly extends into the adjacent air region above and below the metal plates. Figure 4.4 (c) shows that the E_z field has maximum strength but opposite polarity near the metal edges in a similar way to the electric field of a charged capacitor.

It has been suggested that surface plasmon polaritons play an important role in guiding and confinement in TPPWGs at THz frequencies [11]. However, such excitations are very weakly bound to the metal surface and develop over many cm length scales. We believe that, at least for short structures (<10 cm) experimental observations can be explained in the perfect electric conductor (PEC) approximation where there is no field penetration into the metal so that surface plasmon do not exist. We find that this approximation gives good qualitative and quantitative agreement with the experiments described below.

4.3.3 Near field probing measurements

In our experiments, the TPPWG was made of 120 mm long, 6 mm thick polished aluminium plates linearly tapered down to ~20±2 μm. The plates were separately mounted on two xyz translation stages and adjusted to create an entrance slit width of 3 mm and an output air gap of ~20±5 μm. In the geometry that was studied the air angle was θ_a = 1.43° and the metal angle was θ_m = 4.76°. A fibre-coupled photoconductive time-domain THz imaging system with an aperture type near-field probe, as described in Chapter 3, was used to study the TPPWG. The probe consists of a 10 μm dipole antenna behind a 20 μm aperture. The THz source was a conventional LT-GaAs stripline emitter with a silicon substrate lens. The system frequency response is centred at 1 THz with a 10% amplitude bandwidth of 2.5 THz. The x-polarised THz radiation was launched into the waveguide using a pair of off-axis parabolic mirrors and the probe was oriented with its dipole axis parallel to x. Optical microscopes oriented along the x and y axes were used to monitor the probe approach to the output end of the waveguide and to approximately calibrate the probe-aperture separation.

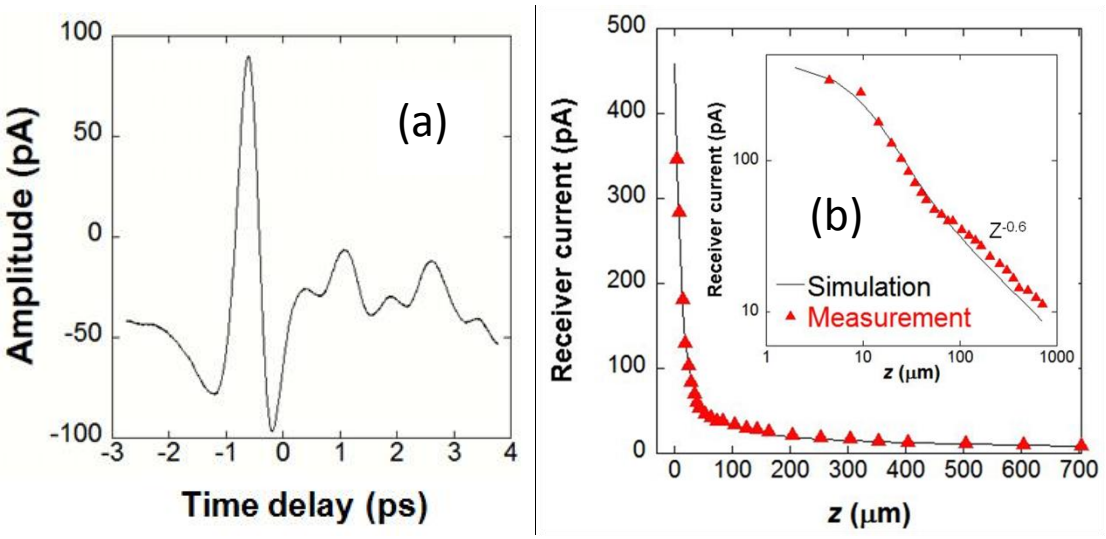

Figure 4.5. (a) Measured time-domain signal from TPPWG at z = 15 μm. (b) Calculated (solid line) and measured peak (red triangles) to peak amplitudes along the z axis. The inset is a logarithmic plot of the same data.

Figure 4.5 (a) shows the measured time-domain signal 15 μm away from the output end of the TPPWG. The shape of input pulse is preserved, suggesting negligible dispersion. Figure 4.5 (b) shows the z variation of the x component of the electric field near the open end of the TPPWG. Simulations and experiments both revealed that E_x falls off

approximately as $z^{-0.6}$ in the far field ($z > \lambda$, $z > 100$ μm) but varies more slowly in the very near-field region ($z < d$) (see the inset of Figure 4.5b). The calibration of the absolute distance of the probe from the output end of the TPPWG was finely tuned by linearly fitting the experimental data to the calculation. The minimum distance of approach was then found to be ~5±0.5 μm.

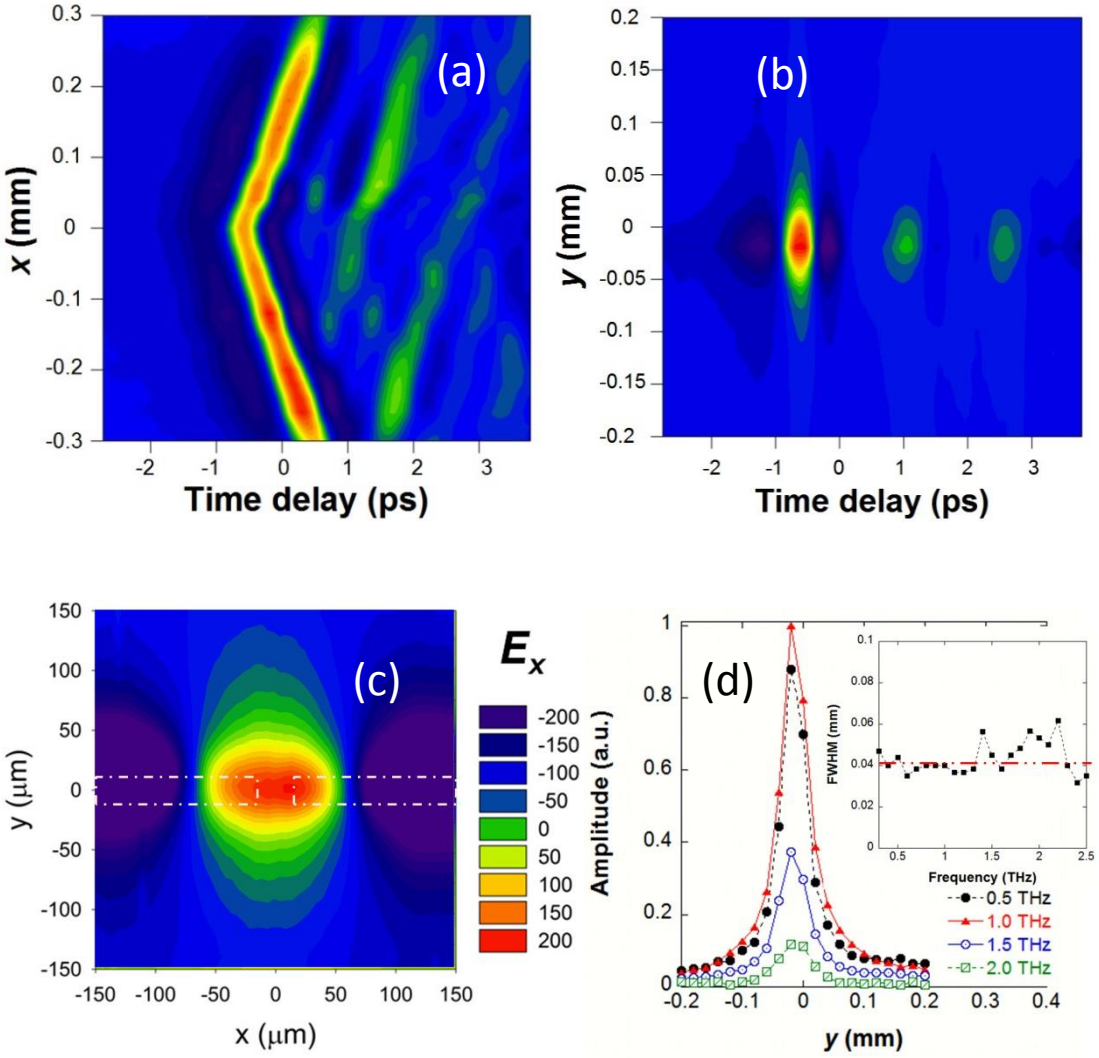

Figure 4.6. Experimental spatial-amplitude maps in the planes at z = 15 μm (a) y = 0 and (b) x = 0. (c) Peak amplitude map for z = 15 μm with delay fixed at the value for the positive peak-on-axis amplitude. The dash lines indicate the area of metal plates. (d) Different spectral amplitudes along y axis at z = 15 μm. The inset shows that the FWHM is independent of frequency with a value of ~40 μm.

The electric field maps shown in Figures 4.6 (a) and (b) were obtained by scanning the near-field probe along x and y at a constant distance of ~15 μm from the output end of the waveguide, with the delay fixed at the peak of the THz signal. A large modal

intensity is clearly distinguishable in the square gap of the two metal plates. The fundamental mode for the sub-λ scale propagation is a TEM-like mode with dominant field component E_x. Even with open boundary conditions along the y axis, the mode is efficiently confined to sub-λ scales. However, along the x axis, the measurement shows that the THz field seems to be extended and the signal is increasingly delayed with increasing x. The peak amplitude delay (Figure 4.7a z = 15 μm) follows a sharp "V" shape with slope corresponding to the velocity of light in air. This effect is an artefact of the measurement and is described in section 4.3.4.

We raster scanned the probe to create a 2-dimensional field map with a time delay at the peak amplitude value to confirm our measurements as shown in Figure 4.6 (c). Figure 4.6 (d) plots the amplitude along the y axis at different frequencies. The super focusing property is frequency independent and the full width at half maximum intensity (FWHM) is about 40 μm up to 2.5 THz. This value is larger than the physical aperture dimension but the fringing fields and probe resolution should be taken into account. We conclude that the TPPWG efficiently squeezes the free space THz mode into the output air gap and that deep subwavelength confinement (~$\lambda^2/450$, ν = 1 THz) has been achieved.

4.3.4 Coupling efficiency and propagation into free space

From the practical point of view of using a TPPWG to couple radiation to an object in the near field the beam divergence and 'aperture' transmission are of paramount interest. As the TPPWG exhibits weak dispersion, it simplifies the data analysis to focus on the peak to peak amplitude and peak amplitude delay.

The beam profile along x and y at various values of z are shown in Figures 4.7 (b) and (d). Along the y axis the beam is concentrated in the region of the gap when z is small. In contrast, the field varies slowly with x when z is small. This effect is caused by efficient coupling of x-polarised light into a guided wave in the gap between the probe and end facet of the TPPWG as shown in Figure 4.8. The z component of the guided wave can be detected by the probe and this signal dominates that of E_x, except in the immediate vicinity of the TPPWG aperture. The sensitivity of the probe to E_z arises from scattering at the probe aperture, which create a field component along x that can be directly detected.

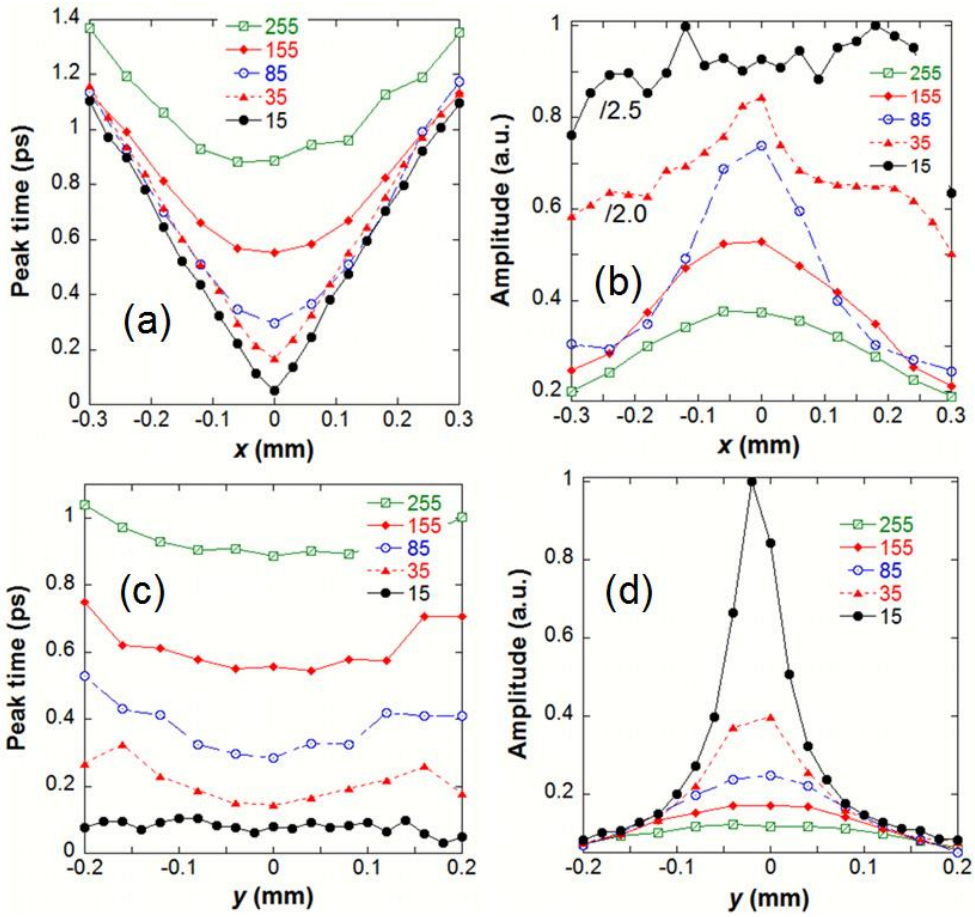

Figure 4.7. (a) Peak amplitude delay and (b) electric field amplitude E_x along the x axis at z = 15, 35, 85, 155, 255 μm. (c) Peak amplitude delay and (d) E_x along the y axis. The amplitudes are normalized to the peak to peak amplitude at z = 15μm.

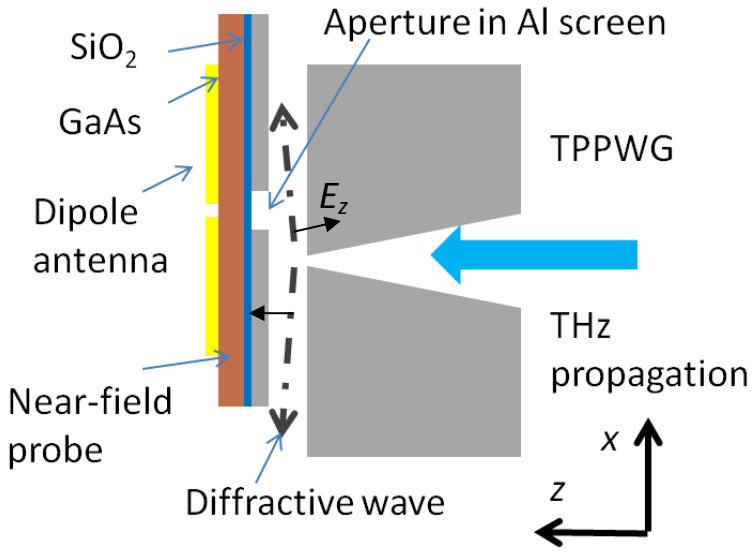

Figure 4.8. Schematic of the waveguide propagation between the TTWG output end and near field probe. The black dash lines show the propagation directions.

This assumption has been confirmed using simulations in CST Microwave Studio [13], where we mimicked the near-field probe by placing a metal plate with a single 20 µm aperture at different positions along the x axis and recorded the field in the aperture. For small z, the simulation shows a very slow fall in E_z with increasing x (Figure 4.9a). The polarity is opposite for positive and negative x. Figure 4.9 (b) shows the field E_x' in the sub-λ aperture at different z positions. The field in the aperture is related to E_x by $E_x' = E_x + k\, dE_z/dx$, where E_x is the field without the 'near-field probe' and k is a constant proportional to the aperture size. When the probe is at z = 15 µm, the electric field amplitude shows little variation over a wide range of x. A dip in E_x' appears at x = 0 where the sign of dE_z/dx is reversed. With increasing probe separation, the amplitude of E_z drops rapidly (Figure 4.7c) and E_x becomes the dominant field coupled into the aperture. Along the y axis, there is no analogous waveguiding mechanism so that the experimental measurement reflects the actual variation of E_x with y in the near field.

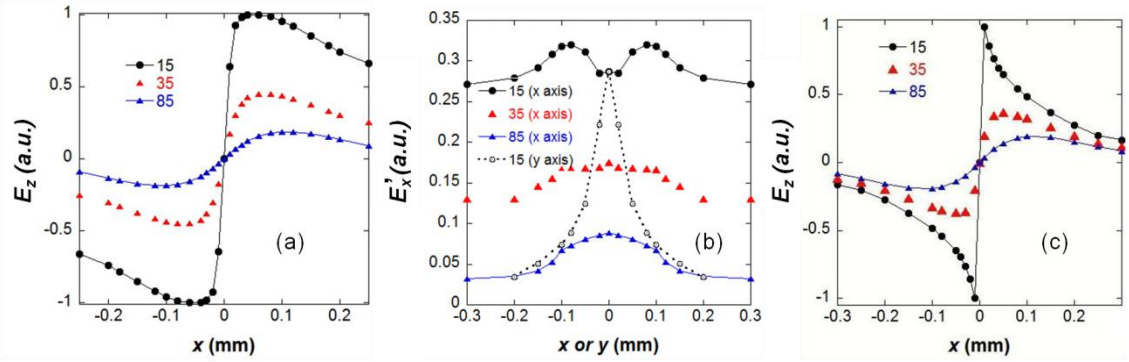

Figure 4.9. (a) Simulated peak to peak amplitudes of E_z along the x axis with a metal plate at different z position. (b) Peak electric field E_x' coupled into the rectangular aperture on the x axis at different z positions. (c) E_z without the metal plate.

The simulated results in Figure 4.9 (b) are in good qualitative agreement with our measurement in Figure 4.7 (b). Since the simulation is performed using the PEC approximation in which surface plasmon polaritons are not supported, we believe that the waveguiding artefact in aperture-based THz near-field probes is only weakly affected by surface plasmons [14, 15].

Next, we compare the experimental beam profile with numerical simulations in terms of the intensity and FWHM along the x and y axes, as shown in Figures 4.10 (a) and

(b). The FWHM contains the majority of the modal power and increases roughly linearly with increasing z but the increase is roughly double along x so that the beam is elliptical in cross-section.

To quantify the integrated intensity along the z axis, 2-dimensional images are preferred but they are slow to acquire. One dimensional line scan along x and y can be used to approximately analyse the propagation. We used a Gaussian distribution to fit the experimental peak to peak amplitudes along the x and y axes (Figure 4.7c, d), respectively. Then we integrated the Gaussian distribution to obtain an intensity at different z positions, as $P = \int E_i^2 \, di, i = x \, or \, y,$ shown in black dots in Figure 4.10 (a) and (b). The simulations were carried out without the near-field probe aperture in front of TPPWG. The results are the line intensity of E_x at 1 THz. Figure 4.10 shows that the intensities are high when z < 50 µm and asymptotically tend to a constant value at large z. This is due to the evanescent field associated with the reflected signal, which does not propagate into the far-field, $z > \lambda$. The reflection signal is caused by the impedance mismatch between the waveguide output aperture and free space [16].

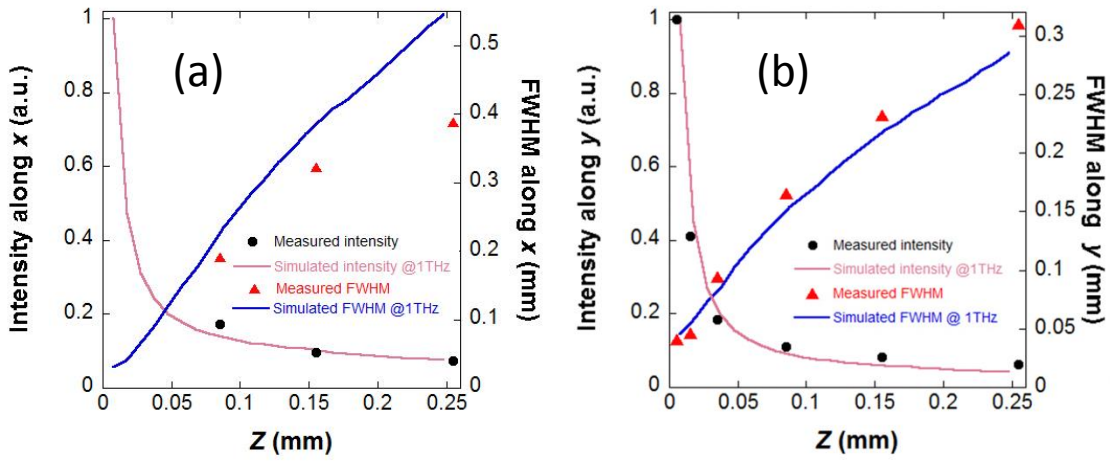

Figure 4.10. (a) Black circles show the integrated intensity along x. The pink curve shows the simulation results at 1 THz. The FWHM of the beam along x is shown in red triangles (experiment) compared with numerical simulation at 1.0 THz (solid blue curve). (b) As for (a) but along y-axis

4.3.5 Guiding loss

The reflection coefficient is determined by the impedance which is related to the local

dimensions *w* and *d* of the waveguide output. There is no simple analytic expression for the local impedance for $w, d \ll z$ However, if we consider the TM_0 mode of the TPPWG, an approximate expression can be derived based on the capacitive coupling between two finite width planar parallel plates, as $Z = Z_0 d/w$, where Z_0 is the impedance of free space, $\sqrt{\mu_0/\varepsilon_0}$. Quantitatively, the reflection coefficient can be obtained by numerical simulations. We kept one of the output physical dimensions as 20 μm and varied the other. The amplitude reflection coefficient was taken as the ratio of the peak electric amplitude of the reflected and incident pulses at z = -1 mm position. Figure 4.11 shows that the reflection coefficient decreases with larger air separation (*d*) and thinner metal (*w*). For $d = w$ the above expression for Z implies a reflection coefficient of zero, which is very different to the result in Figure 4.11. This shows the necessity for numerical simulations.

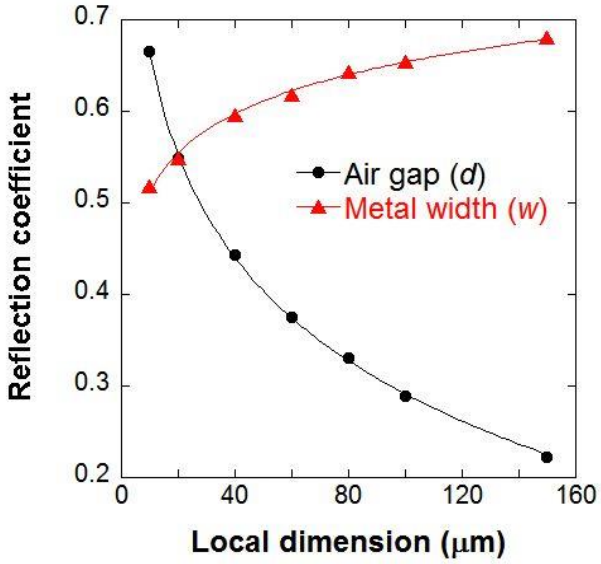

Figure 4.11. Reflection coefficient dependence on the local aperture dimensions. The solid lines are the guides to the eye.

To estimate the loss of the PPWG waveguide, we should consider the electric field at the output waveguide, which is given by [17],

$$E_{out}(\omega) = CE_0(\omega)exp[-j(\beta_z - \beta_0)L]exp(-\alpha L) \tag{4.6}$$

where *L* is the TPPWG length, and $E_0(\omega)$ is the input electric field, a Gaussian beam in our case, as described in Chapter 3. The Gaussian beam FWHM is 0.69 mm along the x

axis in the focal plane of the focusing parabolic mirror. C is the coupling coefficient from the input field to the waveguide TEM mode, which can be obtained quantitatively from the overlap integral,

$$C^2 = \frac{|\int E_0 E_{TEM}^* \, dA|^2}{\int |E_0|^2 \, dA \int |E_{TEM}|^2 \, dA}. \tag{4.7}$$

The calculated electric field coupling coefficient C^2 is ~0.35 with an input air separation D_{in} of 3 mm.

The loss α of a TPPWG is determined by the sum of the loss due to the finite conductivity of the metal, α_c, and that from distributed reflections, α_z, due to the cross sectional change.

For a conventional PPWG, the conductivity loss is given by [18],

$$\alpha_c = \frac{1}{Z_0 d}\sqrt{\frac{\omega\mu_0}{2\sigma}} \tag{4.8}$$

where σ is the dc conductivity of aluminium, 3.5×10^7 Ω^{-1} m^{-1}.

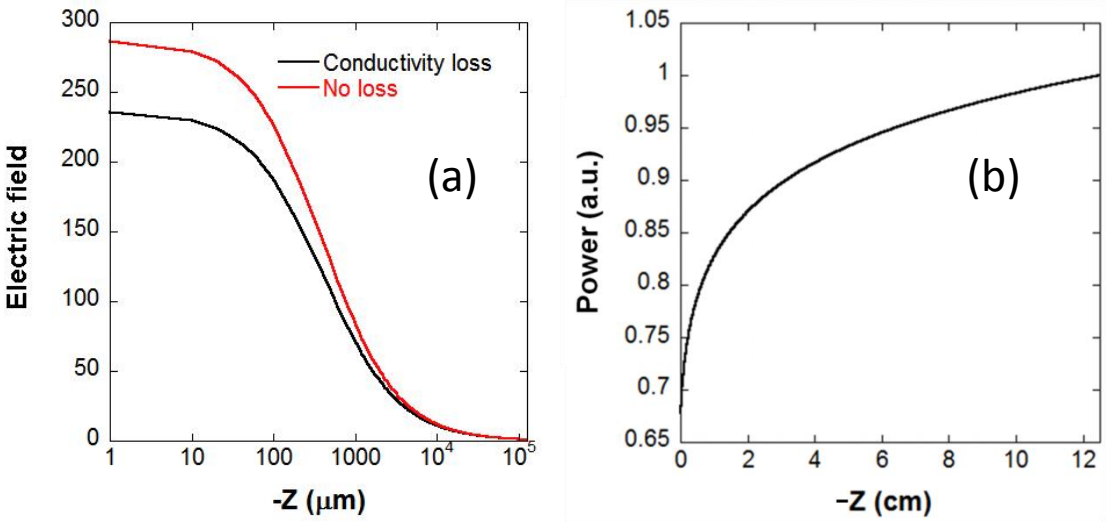

Figure 4.12. (a) The calculated ratio of the electric field at z position to the input field at 1 THz with the uniform field assumption. (b) Integrated power along the z axis.

For a linear tapered PPWG, both the electric field and the attenuation vary approximately inversely with z. If we consider only the conductive loss, the local electric field is given by [19],

$$E(z) = CE_0\sqrt{\frac{W_{in}D_{in}}{w(z)d(z)}}\left[1-\left(1-\frac{d_{out}}{D_{in}}\right)\frac{z}{L}\right]^{\frac{R_s}{Z_0}\frac{L}{D_{in}-d_{out}}} \quad (4.9)$$

where $w(z)$ and $d(z)$ are the local dimension at z, $R_s = (\omega\mu\sigma/2)^{1/2}$ is the surface resistivity. The input metal width and air gap are 11 and 3 mm, respectively. The output aperture *w* and *d* are both 20 μm at z = 0. *L* is the waveguide length of 12.5 cm. Figure 4.12 (a) shows the calculated electric field in the centre of the air gap ratioed to the input field CE_0 versus the z positions, according to Eq (4.9). The field is assumed to be uniform in the gap with no fringing field outside the gap. Figure 4.12 (a) also plots the electric field without the conductivity loss, which is inversely proportional to the square root of the local area along the z axis. Figure 4.12 (b) shows the integrated transmitted power along the z axis. The attenuation increases significantly with smaller plate separation *d*.

The distributed reflection loss can be thought of as a sum of reflections at a series of elements with a local impedance mismatch between input and output. In simulations, we studied the loss related to the finite metal angle θ_m taking the air angle to be $\theta_a = 0$ and a constant gap *d* = 100 μm. A tapered metal section was connected to two parallel plates for input and output coupling to minimize the input coupling loss and TPPWG output reflection as shown in Figure 4.13.

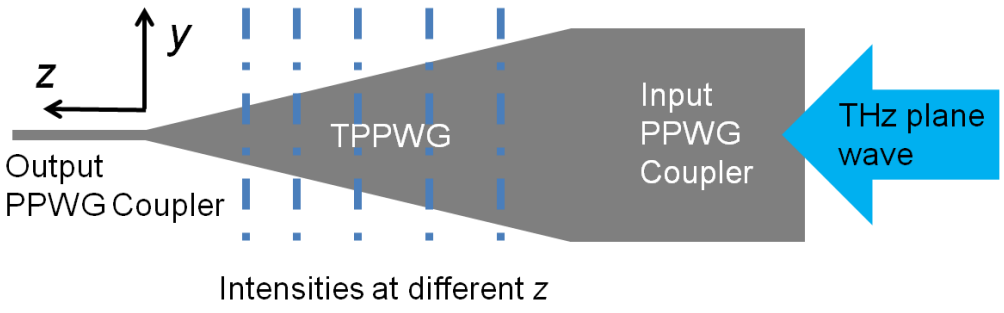

Figure 4.13. TPPWG structure for quantifying the metal angle loss. The blue dashed lines indicate the different positions of z to integrate the intensities of the areas.

A similar technique was used in the study of tapered fibre [20]. The advantage of this technique is that the input field and the output fields are not perturbed by external factors and only depend on the tapered length, *L*. We integrated the field intensity at

different z positions and plotted these values against z. The gradient of the intensity versus z gives the loss. The angle was changed by varying the separation of the two couplers. Figure 4.14 shows the calculated loss as a function of taper angle. As expected, it decreases asymptotically to zero with decreasing taper angle and the fitted curve shows a loss $\propto \theta_m^{2.5}$.

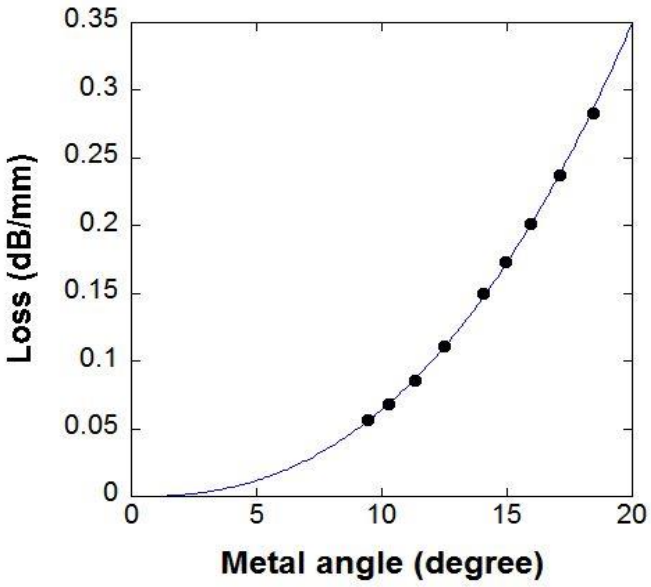

Figure 4.14. The loss of the TPPWG versus metal angle with the air angle fixed at 0.

To compare the simulation result with our experiment, we integrated the measured input field map shown in Figure 3.12 (a). The near-field probe aperture and the measured step size were both 50 μm and the total input intensity was approximately 3.16×10^{14} pA^2 over a 2 by 2 mm^2 area. For the measurements on the TPPWG, the 10 μm dipole near-field probe was used with an aperture of 20 μm, which has a similar size to the output aperture of the TPPWG. We took the maximum amplitude of 450 pA at z = 0 as the output electric field from the TPPWG aperture of 20 by 20 μm^2 in Figure 4.5 (b). With the coupling efficiency C^2 = 0.35, the measured loss was ~0.65 dB/mm for θ_m = 4.76°, θ_a = 1.43° and L = 125 mm. The simulation for the same metal angle indicates a loss as low as 0.02 dB/mm. The difference is possibly attributed to the air angle loss.

We tried many methods to quantify the loss associated with air angle but these were not successful due to the effect of reflections at input and output couplers.

4.4 Conclusions

In summary, we reported a PPWG with an internal step which converted the TEM mode into higher order TM modes. This illustrates the use of the near-field probe to reveal the nature of the mode.

A tapered parallel plate waveguide was constructed to reduce a mm-size THz beam to a subwavelength-size. Good agreement between numerical simulations and experimental results was obtained for the field confinement and the beam divergence. Using numerical simulations, the output reflection coefficient and the taper angle dependent distributed loss have been quantitatively analysed. This work provides some useful practical guides to exploiting the TPPWG for THz micro-spectroscopy and sensing.

References

1. G. Gallot, S. P. Jamison, R. W. McGowan, and D. Grischkowsky, "Terahertz waveguides," J. Opt. Soc. Am. B **17**, 851-863 (2000).

2. R. Mendis and D. Grischkowsky, "Undistorted guided-wave propagation of subpicosecond terahertz pulses," Opt. Lett. **26**, 846-848 (2001).

3. O. Mitrofanov and J. A. Harrington, "Dielectric-lined cylindrical metallic THz waveguides: mode structure and dispersion," Opt. Express **18**, 1898-1903 (2010).

4. O. Mitrofanov, R. Harel, M. Lee, L. N. Pfeiffer, K. West, J. D. Wynn, and J. Federici, "Study of single-cycle pulse propagation inside a terahertz near-field probe," Applied Physics Letters **78**, 252-254 (2001).

5. M. Misra, S. R. Andrews, and S. A. Maier, "Waveguide artefacts in terahertz near field imaging," Applied Physics Letters **100**, 191109 (2012).

6. M. Schnell, P. Alonso-Gonzalez, L. Arzubiaga, F. Casanova, L. E. Hueso, A. Chuvilin, and R. Hillenbrand, "Nanofocusing of mid-infrared energy with tapered transmission lines," Nature Photonics **5**, 283-287 (2011).

7. M. I. Stockman, "Nanofocusing of optical energy in tapered plasmonic waveguides," Physical Review Letters **93**, 019901 (2004).

8. N. Tho Duc, Z. V. Vardeny, and A. Nahata, "Concentration of terahertz radiation through a conically tapered aperture," Optics Express **18**, 25441-25448 (2010).

9. A. Rusina, M. Durach, K. A. Nelson, and M. I. Stockman, "Nanoconcentration of terahertz radiation in plasmonic waveguides," Optics Express **16**, 18576-

18589 (2008).

10. V. Astley, R. Mendis, and D. M. Mittleman, "Characterization of terahertz field confinement at the end of a tapered metal wire waveguide," Applied Physics Letters **95**, 031104 (2009).

11. H. Zhan, R. Mendis, and D. M. Mittleman, "Superfocusing terahertz waves below lambda/250 using plasmonic parallel-plate waveguides," Optics Express **18**, 9643-9650 (2010).

12. N. Klein, P. Lahl, U. Poppe, F. Kadlec, and P. Kuzel, "A metal-dielectric antenna for terahertz near-field imaging," Journal of Applied Physics **98,** 014910 (2005).

13. J. S. Melinger, N. Laman, S. S. Harsha, and D. Grischkowsky, "Line narrowing of terahertz vibrational modes for organic thin polycrystalline films within a parallel plate waveguide," Applied Physics Letters **89**, 251110 (2006).

14. R. Mueckstein and O. Mitrofanov, "Imaging of terahertz surface plasmon waves excited on a gold surface by a focused beam," Opt. Express **19**, 3212-3217 (2011).

15. R. Mueckstein, C. Graham, C. C. Renaud, A. J. Seeds, J. A. Harrington and O. Mitrofanov, "Imaging and analysis of THz surface plasmon polariton waves with the integrated sub-wavelength aperture probe," Journal of Infrared, Millimeter and Terahertz Waves **32,** 1031-1042 (2011)

16. K. Iwaszczuk, A. Andryieuski, A. Lavrinenko, X. C. Zhang, and P. U. Jepsen, "Non-invasive terahertz field imaging inside parallel plate waveguides," Applied Physics Letters **99**, 071113 (2011).

17. J. Zhang and D. Grischkowsky, "Adiabatic compression of parallel-plate metal waveguides for sensitivity enhancement of waveguide THz time-domain spectroscopy," Applied Physics Letters **86**, 1-3 (2005).

18. D. M. Pozar and M. P. David, *Microwave engineering* (New York Chichester : Wiley, New York Chichester, 2004).

19. K. Iwaszczuk, A. Andryieuski, A. Lavrinenko, X. C. Zhang, and P. U. Jepsen, "Terahertz field enhancement to the MV/cm regime in a tapered parallel plate waveguide," Opt. Express **20**, 8344-8355 (2012).

20. C. Chun-Wen, W. Mount-Learn, and H. Wen-Feng, "Design of low-loss tapered waveguides using the telescope structure compensation," IEEE Photonics Technology Letters **15**, 1378-1380 (2003).

Chapter 5
Dielectric thin-wall terahertz waveguides

5.1 Introduction

The previous chapter explored the metal parallel plate waveguide. In this chapter, we turn our attention to dielectric materials as THz waveguides. Using the antiresonant optical reflection waveguide principle, hollow core dielectric structures can guide THz radiation with low loss and broadband transmission.

Planar guides consisting of parallel thin plastic films were constructed to explore the guiding efficiency and properties of the core and cladding modes. Cylindrical silica capillaries and microstructured capillaries were also fabricated and characterized in terms of transmission band and loss.

5.2 Parallel dielectric thin-film for THz waveguide

5.2.1 Introduction

There has been recent interest in the fabrication of hollow waveguides to efficiently guide terahertz waves because guiding is mostly in the air and other materials are much more lossy in that frequency regime. In order to achieve broadband transmission, the antiresonant reflection optical waveguide (ARROW) concept has been applied in the THz regime [1]. In this scheme, guidance is achieved by destructive interferences of waves reflected from the interfaces of high-index materials surrounding an air core as

in a Fabry-Perot resonator. As the overlap of the propagating core-mode with the guide material is small, the efficiency of such waveguides is determined more by the geometry than the material, although the material choice does affect the loss and dispersion [2, 3].

To achieve a large bandwidth for transmission, high-index thin walls are preferable. Commercially available Teflon tubes have been verified experimentally to be capable of extremely low attenuation of 0.0008 cm^{-1} below 1 THz [2].

Most current work on dielectric guides focuses on the cylindrically symmetric case. Examples include the glass capillary [3] and microstructured fibres [4]. However, the fibre diameter and wall thickness are not easily varied independently for systematic studies. Here, we demonstrate the use of two-parallel planar dielectric sheets to form an ARROW resonator for TM guided modes. Its guiding principle is similar to that of fibres, but the core dimension can be varied whilst keeping the dielectric wall thickness constant or vice-versa.

We begin with a demonstration of two guiding mechanisms in parallel dielectric thin film: ARROW and subwavelength guiding. The latter term refers to guiding in a simple film. As the thickness of the dielectric is subwavelength, the majority part of the field is evanescent and guided outside the film and we define this type of waveguide as a subwavelength guide. The core-mode and cladding mode are studied in time and frequency domains. Then, we characterize the propagation properties of single thin films, similar to but one order of magnitude thinner than, the ribbon waveguide which Mendis and Grischkowsky have previously studied [5].

5.2.2 ARROW waveguide

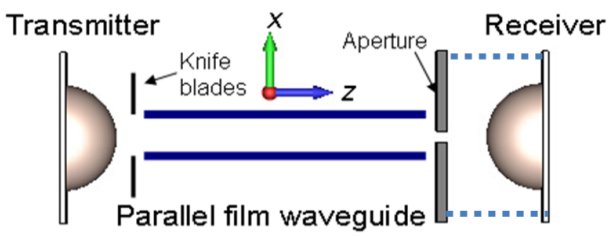

Figure 5.1. The experimental geometry. A 0.3 mm aperture was attached to the front of the receiver's silicon lens and moved together with the receiver.

We used two identical polyester thin films of 13.5 cm length to form a planar parallel sheet dielectric waveguide. The polyester films are known under the trade name of Mylar (HiFi industrial film Ltd, Stevenage). The attenuation constant of Mylar is reported to be about 20 cm^{-1} at 1 THz and is only weakly frequency dependent [6]. The two films were mounted on individual translation stages to achieve a variable separation between them. The experimental geometry is shown in Figure 5.1. A plane wave with electric field along the x axis (E_x) and a large input diameter of ~6 mm was launched to excite the fundamental mode. Razor blades were used to define an input aperture to avoid unwanted coupling to cladding modes, i.e. the subwavelength guiding.

Experimentally, end fire coupling was found to be efficient for both parallel film waveguide and single dielectric films. We compared this scheme with one using a plano-convex silicon lens with a focal length of ~5 cm and found a similar coupling efficiency.

Figure 5.2 (a) shows the core mode temporal signals for film thicknesses of 50 and 100 μm and a separation of 2.0 mm, measured with a 0.3 mm diameter circular receiver aperture on the optical axis. It is seen that the core-mode exhibits negative group-velocity dispersion, where the higher frequency signal components travel faster than the lower frequency components and the input pulse broadens to over 5 ps.

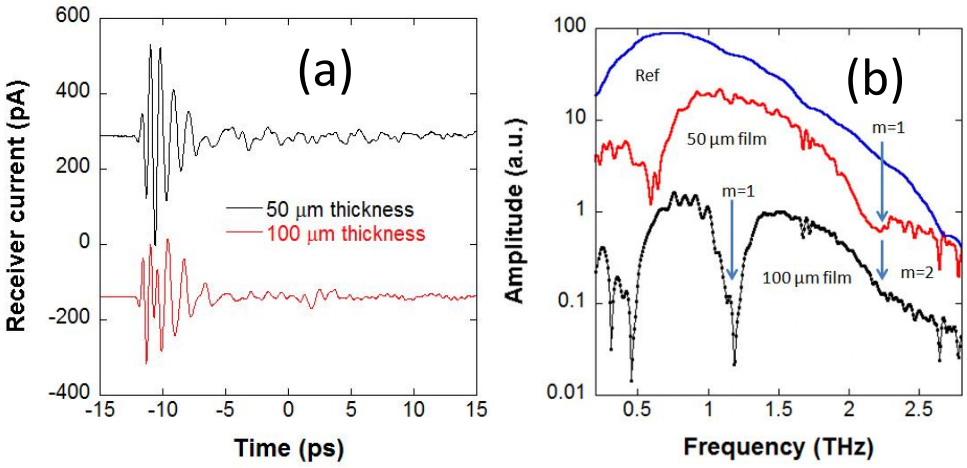

Figure 5.2. (a) Time domain traces of the core mode of the parallel thin Mylar film guide with a separation of 2 mm. (b) Spectra corresponding to the traces in (a). The vertical lines show the resonant frequencies calculated using Eq (5.1). The reference signal was obtained by removing the waveguide.

For the individual dielectric planar film, like a Fabry-Perot resonator, the reflected beams from the front and back air-dielectric interfaces interfere. The phase difference δ between the two beams is given by [7],

$$\delta = \frac{4\pi t}{\lambda}\left({n_f}^2 - {n_0}^2 \cos^2\theta\right)^{1/2} - \pi \tag{5.1}$$

where n_f is the refractive index of the dielectric film and n_0 is that of the surrounding medium, θ is the incident angle relative to the film surface, and t is the thickness of the dielectric. For a small angle $\theta < 30^o$, there is a π phase shift arising from reflections for either case, regardless of the TM or TE waves. For a destructive interference, the phase difference must equal to an odd multiple of π, so that

$$\frac{2\pi t}{\lambda}\left({n_f}^2 - {n_0}^2 \cos^2\theta\right)^{1/2} = m\pi, \qquad m = 1,2,3 \ldots \tag{5.2}$$

For our parallel dielectric thin-film waveguide, the core separation *d* is nearly an order of magnitude larger than the wavelengths，$d \gg \lambda/2n_0$, so the lowest order core-guided TM_0 mode propagates with a longitudinal wavevector β along the optical axis close to the free-space wave number ($\theta = 0$). The fundamental mode destructive resonant frequencies can then be obtained by the simple ARROW theory result,

$$f_m = \frac{mc}{2t\sqrt{{n_f}^2 - {n_0}^2}}. \tag{5.3}$$

The bandwidth of the transmission windows is given by,

$$\Delta f = f_m - f_{m-1} = \frac{c}{2t\sqrt{{n_f}^2 - {n_0}^2}}. \tag{5.4}$$

The spectra of the measured traces are presented in Figure 5.2 (b). For the 50 μm thick film, a transmission window is clearly visible with a loss dip (first resonant frequency) at 2.25 THz, whilst the equivalent dip for the 100 μm thickness films waveguide appears at 1.18 THz. The smaller second order resonant dip at 2.25 THz for the 100 μm film is attributed to its lower loss character. The arrows in Figure 5.2 (b) show the resonate frequency calculated using Eq (5.4) and a refractive index for Mylar of 1.67 [8]. There is good agreement with experiment.

It is useful to visualize the field distribution at the output end of the waveguide. The x component of the THz field was measured as a function of position along the x axis at the end of the waveguide. This is shown as a space-time map for 36 μm in Figure 5.3 (a). A substantial fraction of the core mode is guided in the gap between the parallel dielectric films. A small difference in time delay of ~0.5 ps between the time-domain electric fields in the core and outside of the core at a delay of -12 ps indicates that the leaky field is from the core. The amplitude ratio of the leaky field to the maximum core mode field is up to ~0.3, which indicates the very weakly confining properties of the ARROW mechanism. The loss of 36 μm films with a 2 mm separation was measured to be ~0.54 dB/cm at 1.0 THz (within the fundamental band) by comparing two different length waveguides.

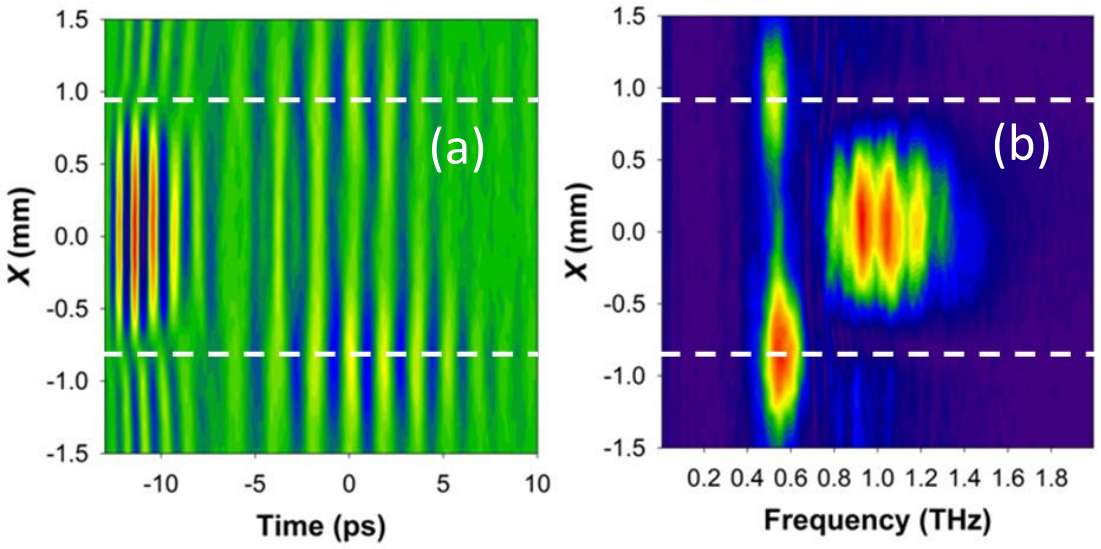

Figure 5.3. (a) Time domain electric field map along the x axis of 36 μm parallel dielectric film guide with a film separation of ~2.0 mm. (b) Corresponding spectral field map. The white dashed lines show the two films positions.

Figure 5.3 (b) shows the corresponding space-spectral map to Figure 5.3 (a). It clearly displays two spatial modes with different spectra. The higher frequency mode is confined in the core, whilst narrower band, lower frequency modes are guided by the individual films. We also examined the time-domain signals along the y axis (not shown) which exhibit a frequency independent Gaussian profile extending over many mm. It is concluded that a TM_0 mode is guided between the parallel dielectric films by the ARROW mechanism and that at lower frequencies guiding takes place in the thin-

walled films. We discuss this cladding mode further in the following section.

5.2.3 Subwavelength thin-film guided mode

Subwavelength diameter plastic fibres have been studied by Chen *et al* in the terahertz range [9]. In this work, less than 1% of the light propagated in the solid core by total internal reflection, while the majority of the light was guided as an evanescent surface wave. Here we studied single Mylar films with thickness an order of magnitude smaller than the guiding wavelength.

We used a cylindrical silicon substrate lens to couple to the film. A receiver slot aperture ~500 μm wide was employed to avoid the signal from unguided radiation. Knife blades were also placed very close to the cylindrical lens on both sides of the film.

Figure 5.4 shows transmitted spectra for films of different thicknesses with the same length of 13.5 cm but the same vertical scale is used for all data. The thinner films support a broader bandwidth and guide with higher transmission. The majority of the field is guided in the air. We now discuss the complex effective index $n_{eff} = N_m + i\alpha/2k_0$: the real part controls the time delay in propagation and the imaginary part the material absorption and other losses.

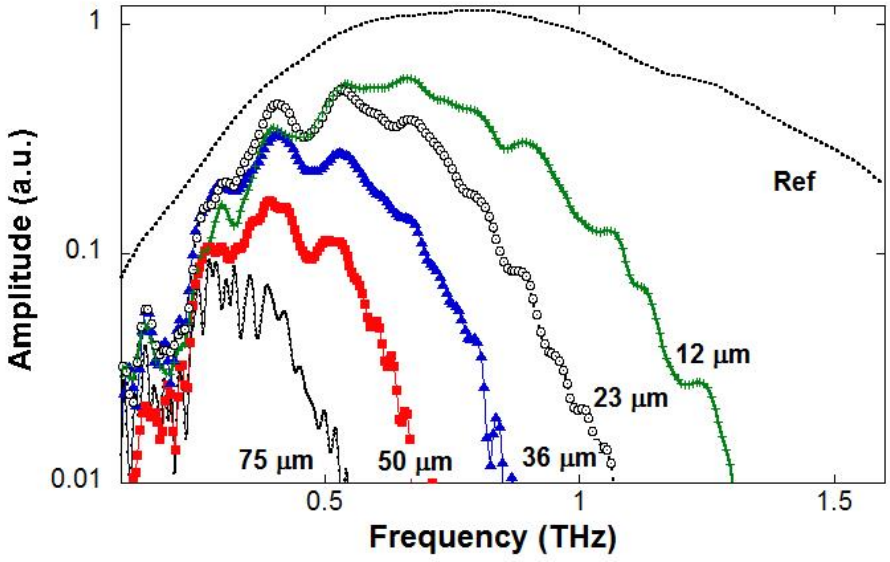

Figure 5.4. Transmitted spectra of different thickness Mylar film waveguides of 13.5 cm length.

The effective refractive index N_m can be derived from the dispersion formula of a dielectric slab waveguide. The transverse resonance condition is given by [10],

$$\frac{2\pi f}{c}\kappa t - 2\phi = m\pi, \qquad m = 1,2,3,\ldots \tag{5.5}$$

where t is the film thickness, ϕ is the phase angle of the total internal reflections at the film's surfaces, m is the index of the propagating mode.

$$\kappa = \sqrt{n^2 - N_m^2} \tag{5.6}$$

$$\phi = \tanh^{-1}(n^{2\sigma}\sqrt{N_m^2 - 1}/\kappa) \tag{5.7}$$

where n is the refractive index of the Mylar, N_m is the effective index of the m-th mode of propagation. $\sigma = 0$ for TE and $\sigma = 1$ for TM polarization. In our case the fundamental mode is guided so $m = 1$ and $\sigma = 1$. The real part of the refractive index, N_1, can be obtained from the measured spectral and shows good agreement with calculations from Eqs (5.5)-(5.7) as shown in Figure 5.5.

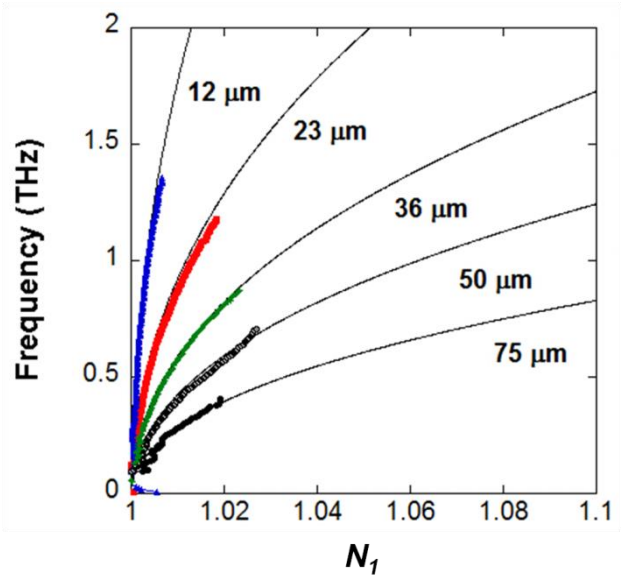

Figure 5.5. The effective refractive index N_1 of different Mylar films. Solid lines are calculations and dots are measurements.

We measured the field distribution along the x axis, as shown in the spectral map in Figure 5.6. The majority of the power is guided in the air surrounding the Mylar film

and the spatial extent is frequency dependent. The white points in Figure 5.6 are the 1/e amplitude falloff distances and show that the higher frequency components are bound more closely to the dielectric.

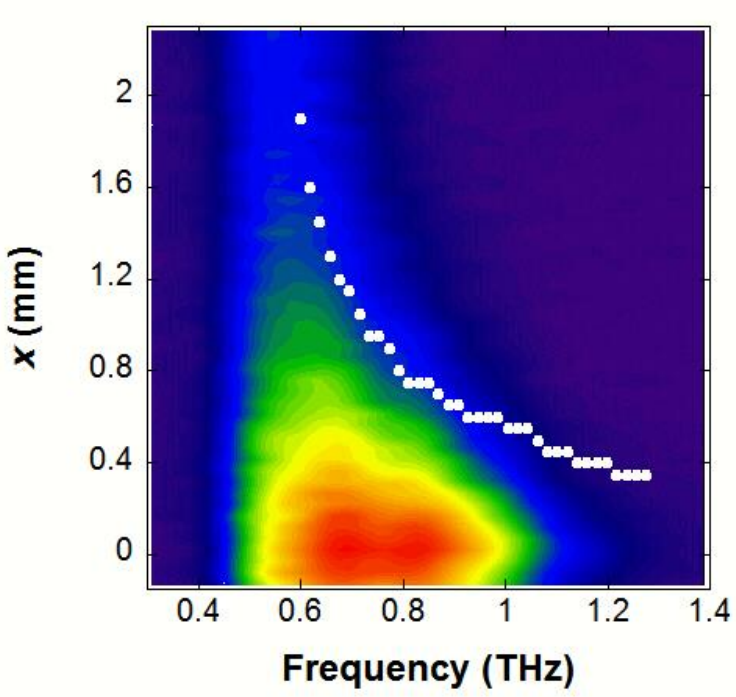

Figure 5.6. Spatial-frequency map of a 12 μm thick Mylar waveguide. The white dots are the 1/e amplitude falloff distances for each frequency. The film is centred at x = 0.

The spatial overlap with the material of the guide is frequency dependent. Contribution to the attenuation of such a waveguide can be summed as [10]:

$$\alpha = f\alpha_b + \alpha_s + \alpha_c \tag{5.8}$$

where α_b is the Mylar material loss, α_s is the radiation loss due to the scattering at irregularities and α_c due to curvature. In our measurement, the films were held straight and cleaned with acetone before measurements. Therefore, we ignored the loss due to scattering and curvature. f is the absorption loss factor associated with the portion of guided field in the material, $f = (2cW_e)/nP$, where W_e is the average electric energy stored in the dielectric slab per unit length and P is the guided power. For the thickness t much less than λ, the loss factor can be simplified to [10],

$$f = 2\pi^2 n(n^2-1)(t/\lambda)^2 n^{-6\sigma}\,. \tag{5.9}$$

The waveguide absorption of the 36 μm thick Mylar film was measured using two different lengths and is shown in Figure 5.7 (a). There is good agreement with the calculation from Eqs (5.8) and (5.9), if the Mylar bulk loss is taken as 20 cm^{-1} for all frequencies. Cutback measurement was performed to study the absorption loss in more detail. Figure 5.7 (b) shows that the attenuation is 199 dB/m at 0.8 THz and 88 dB/m at 0.5 THz.

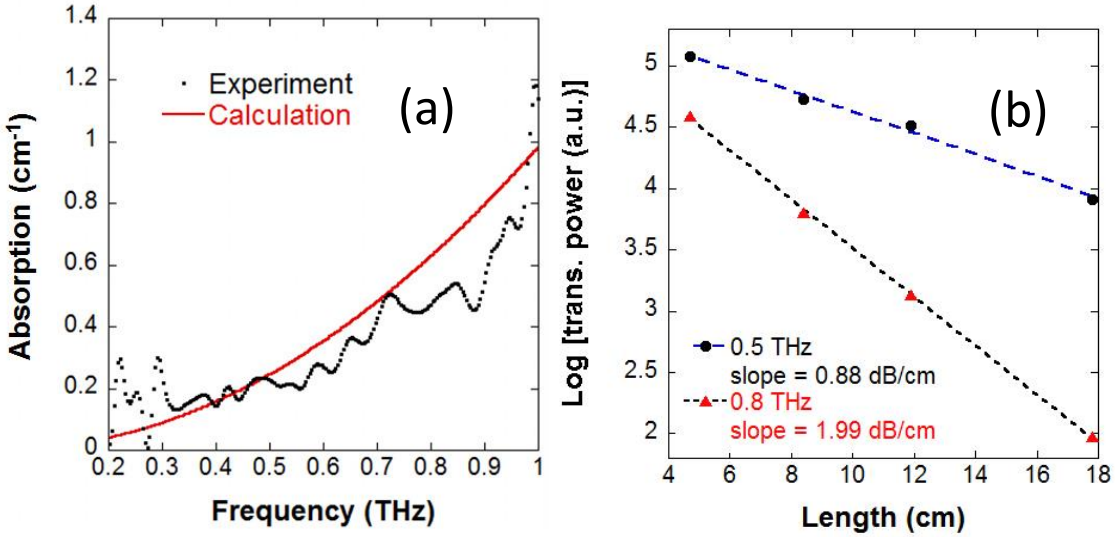

Figure 5.7. (a) The absorption measurement and calculation for the TM_1 mode of a 36 μm Mylar film. (b) Cutback measurement of transmitted power at 0.5 and 0.8 THz

5.2.4 Effect of reduced core size

Figure 5.8 (a) shows the spatial-temporal map obtained by varying the separation of parallel films of 36 μm thickness. The high frequency core mode before the time delay of -5.0 ps shows faster oscillations in time, due to the severe group velocity dispersion with smaller separations. The few oscillation shape for 3.5 mm film separation monotonically develops into many oscillations at 1.5 mm. On the other hand, the subwavelength mode which dominates after -5.0 ps, is not strongly affected by the gap size. The curvature in the wavefront of this mode below 1.5 mm separation is due to the interaction of the surface waves on the two films, which increases the effective index and causes the time delay shift.

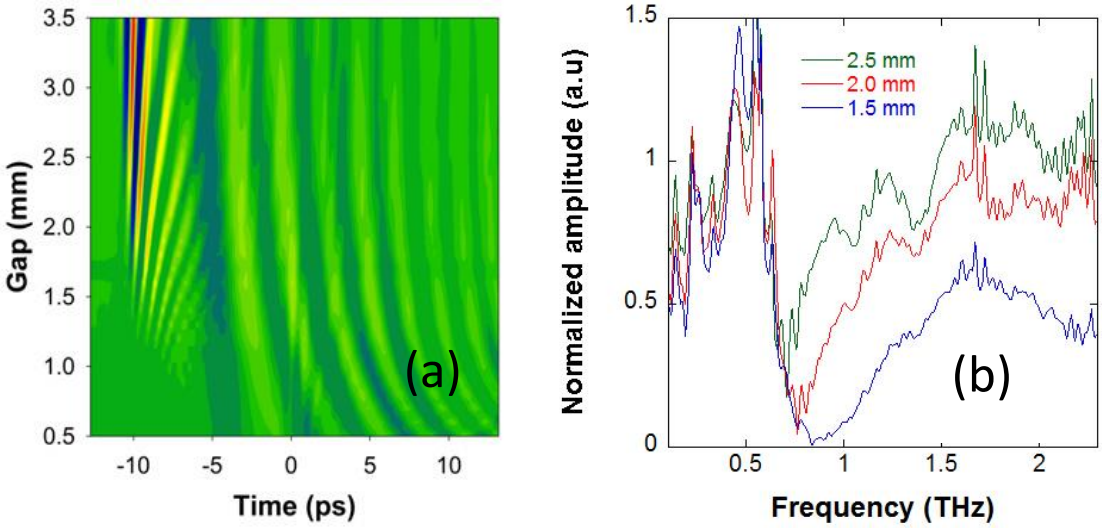

Figure 5.8. (a) Amplitude-time map of the waveguide showing the effect of changing the film separation. The core mode and subwavelength mode are both evident. (b) Normalized amplitude spectra for three gaps normalized to the transmitted spectrum with a gap of 3.5 mm.

Figure 5.8 (b) shows the spectra for three different separations normalized to the spectrum at 3.5 mm separation. A ratio over unity is an artefact caused by the THz system drift. One can notice that the frequency components below 0.6 THz are nearly independent of separation and are associated with guiding in the films. In the ARROW mode for higher frequencies, there is increasing attenuation with decreasing separation. There is a loss band around 0.6-1.0 THz between the ARROW mode and the subwavelength mode, which shifts to higher frequency with smaller separation as shown in Figure 5.8 (b). The fundamental band for the ARROW mode could be recognized as the frequency components between the dip frequency and the first resonant frequency.

It is interesting to compare the above results with those for hollow core fibres exploiting the ARROW mechanism at visible frequencies [11]. In this case, the loss band separating the two guiding mechanisms is not as pronounced and there is less difference between the subwavelength mode and core mode in the transmittance spectrum. This is attributed to the fact that the core diameter is 50 times larger than the guiding wavelength and the silica material absorption is very small. For our parallel Mylar film waveguide, a 2 mm “core size” is only seven wavelengths at 1 THz and the dielectric absorption is higher.

The parallel dielectric film waveguide exhibits negative GVD for the core mode and positive GVD for the cladding mode. The waveguide offers flexibility in control of the transmitted spectrum by using different film thicknesses and separations.

5.3 Cylindrical silica capillary

5.3.1 Introduction

Despite the relatively low loss of some polymer materials used in THz waveguiding, they are not suitable for some interesting applications, such as high intensity THz guiding which requires materials with high damage threshold. Silica is a promising alternative candidate. The well-established fabrication techniques for fused silica allow the production of a variety of thin-walled microstructured fibres with engineered properties, e.g. a negative curvature of the core boundary can be used to improve the transmission [12].

Guiding of THz radiations in a single silica capillary with 6 mm diameter has been demonstrated with a low loss of 0.03 cm^{-1} at 1 THz [3]. A stack of capillaries, like a Kagome structure of periodic silica rings [4], has potentially similar guiding properties [13]. The spectral characteristics are dominated by the first high-index layer rather than the periodic cladding structures [14] but the microstructuring strategy using stack-and-draw techniques [15] can easily achieve very thin guide walls. This allows shifting of the fundamental resonant to higher frequency whilst maintaining the ability to easily handle the structure, which can be suspended in a thick cladding jacket.

Here, we describe a microstructured silica capillary with subwavelength thick walls and characterize the waveguide transmission. Combining this with a study of a single capillary, we are able to compare the antiresonant core and cladding modes by analysing the space-time maps. Then we use cutback measurements to characterize the attenuation.

5.3.2 Antiresonant transmission

A single silica capillary fabricated using fibre perform drawing techniques is shown in Figure 5.9 (a). The microstructured design in Figure 5.9 (b) consists of a thick silica capillary jacket containing 8 smaller capillaries around a core without a central supporting capillary. The whole structure was drawn to the desired size using a controlled pressure of nitrogen in the central core.

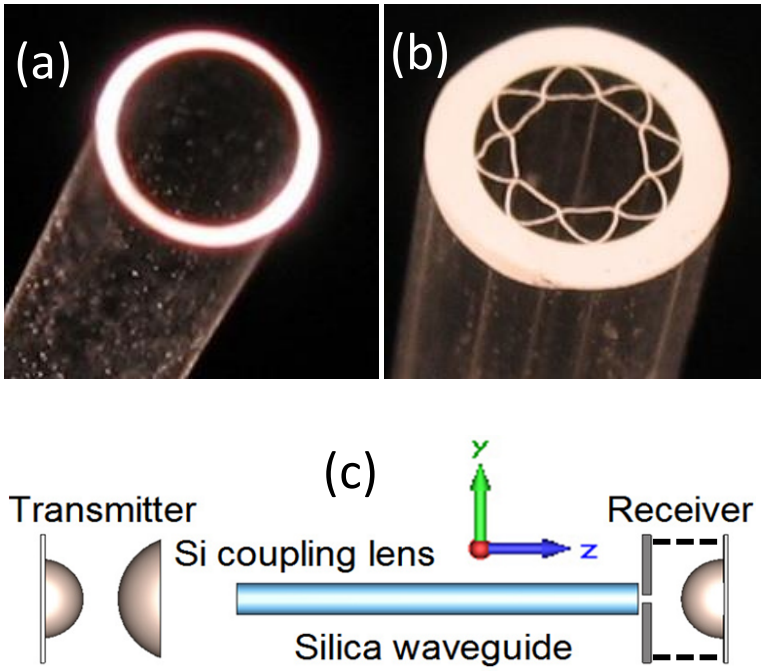

Figure 5.9. (a) Photograph of a 2.16 mm-inner diameter simple capillary with a wall thickness of 84 µm. (b) 2.14 mm inner diameter microstructured capillary with 37µm wall thickness (the first silica layer around the core). The gap between the thick jacket and the core inner wall is ~0.63 mm. The white areas are silica. (c) Schematic of the experimental geometry. A plano-convex silicon lens is used to couple the transmitter to the capillary. A wavelength size circular aperture is attached to the front of the receiver to measure the spatial dependence of the transmitted field.

The waveguides were characterized using time-domain THz imaging with a photoconductive transmitter and a freely positionable fibre-coupled 10 µm-dipole receiver in the geometry shown in Figure 5.9 (c). The capillary ends were polished flat. A high resistivity silicon lens with 5 cm focal length was used to focus the THz beam to a diameter of about 2 mm to excite the waveguide fundamental mode. A 0.3 mm diameter metal aperture with 0.2 THz low frequency cutoff was fixed to the front of the receiver's silicon lens to increase the spatial resolution. Using a motorized translation

stage, the receiver assembly was scanned across the output end to map the transmitted fields.

Examples of time-domain signals obtained from the simple and microstructured capillaries with the receiver aperture on the optical axis are shown in Figure 5.10 (a). The incident THz pulse undergoes considerable dispersive reshaping and broadening during the waveguide propagation and emerges strongly frequency chirped. Fast-oscillations are distinguishable in front of both guided traces, which implies that the hollow core experience a negative (i.e. anomalous) dispersion (higher frequency components travel faster).

The corresponding spectra of the time-domain traces are plotted in Figure 5.10 (b). Two transmission windows are clearly visible and separated by resonant dips near 1.08 and 2.14 THz for the 2.16 mm diameter capillary, and 1.45 and 2.83 THz for the 1.77 mm diameter capillary. The first resonant loss band for the microstructured capillary appears at 2.5 THz and the transmission window is about 1.5 THz wide, which shows good agreement with the calculations of Eq (5.3).

For a hollow core fibre surrounded by an infinite dielectric material, the dispersion curves can be obtained from [16],

$$\beta_{nm} = \frac{2\pi}{\lambda}\left[1 - \frac{1}{2}\left(\frac{u_{nm}\lambda}{\pi d}\right)^2\right] \tag{5.10}$$

where β_{nm} is the propagation constant, d is the diameter of the waveguide and u_{nm} is the m-th root of the Bessel function $J_{n-1}(u_{nm}) = 0$. The equation is not exactly applicable to a thin walled cylindrical waveguide (i.e. single capillary or microstructured capillary), but approximately indicates the dispersion properties: β_{11} for the HE_{11} mode is very close to k_0. This is why we cannot accurately extract the dispersion curves from the time-domain measurements.

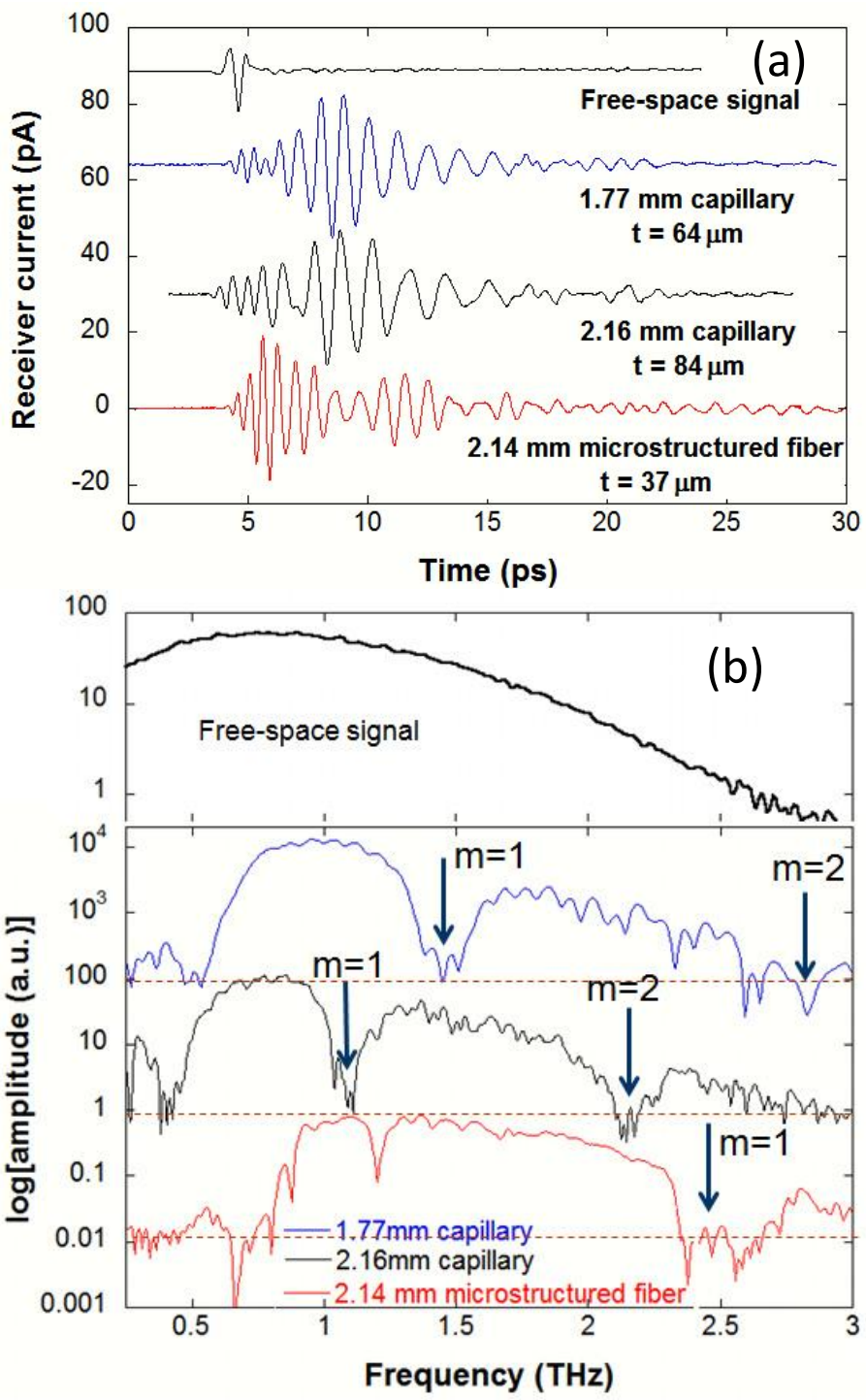

Figure 5.10. (a) Time-domain signals measured for simple capillaries of length 13.5 cm and a microstructured capillary of length 22.5 cm. The value in mm refers to the inner diameter and t is the wall thickness. (b) Spectra of the time-domain traces. The arrows indicate the calculated resonant frequencies. The signals have been vertically offset for eye in the figures and the red dashed lines indicate the noise levels.

5.3.3 Core and cladding modes

It is noticeable in Figure 5.10 (b) that additional low transmission bands appear around 0.4 THz for the 2.16 mm capillary and 0.5 THz for the 1.77 mm capillary. The fundamental guided band begins at 0.8 THz for the microstructured capillary with the even thinner wall of 37 μm. The low transmission band is not due to the receiver aperture cutoff because this is around 0.2 THz, as demonstrated in Chapter 3. By removing the receiver aperture, lower-frequency components in the single capillary were found to be time delayed by tens of ps with respect to the main peak.

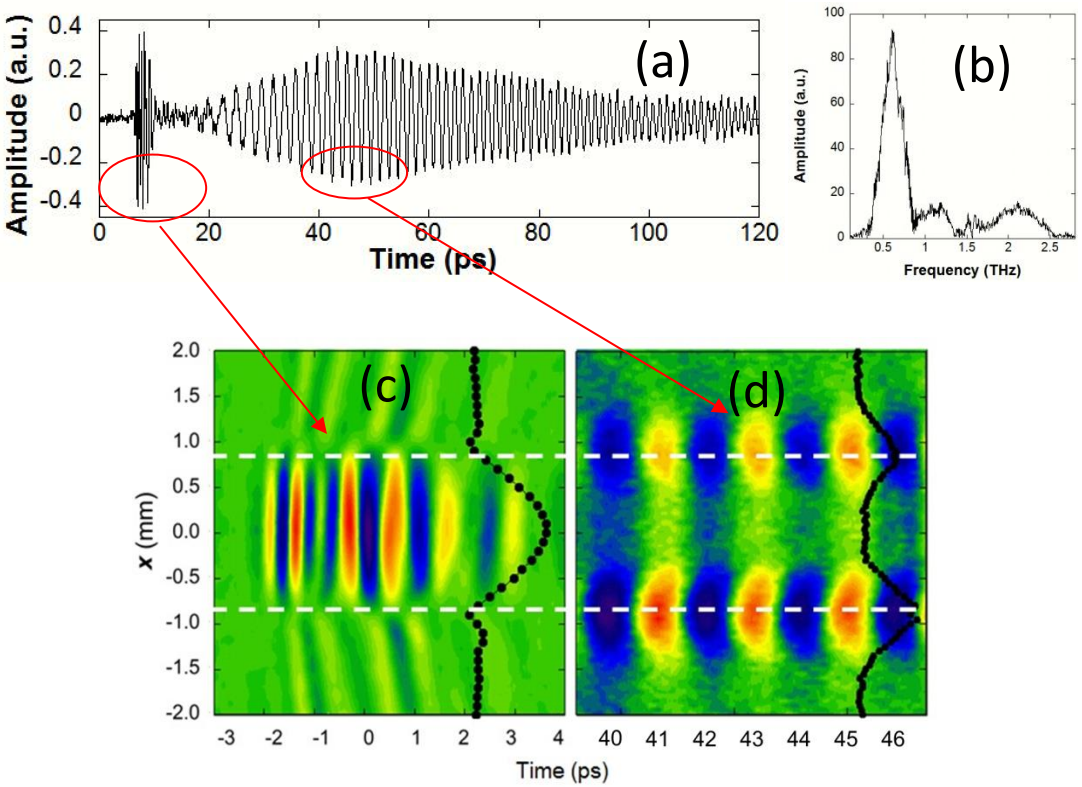

Figure 5.11. (a) Time domain signal with receiver aperture centred on the wall of a 1.77 mm diameter, 64 μm wall thickness capillary. The core and cladding modes are distinguishable in time. (b) Corresponding spectrum of the time-domain signal of (a). (c), (d) Measured spatial field maps (red positive, blue negative field). Black dots show the peak to peak amplitudes and reveal the Gaussian profile core mode in the air region and cladding mode in the thin walls. White dashed lines indicate the position of the silica wall.

To identify the low frequency waveguide mode, we focus on the simple capillary with 1.77 mm diameter. Figure 5.11 (a) shows the time-domain signal when the 0.3 mm receiver aperture is placed near the edge of the silica wall. Figure 5.11 (b) shows the

corresponding spectrum, which has a centre frequency of 0.61 THz and a narrow bandwidth of 0.15 THz.

We also measured a smaller-core capillary (d = 1.28 mm) with 34 μm wall thickness, which displayed a highly coherent trace over a long time-scale (>100 ps) and transmits in a narrow band (Δf = 0.2 THz) with a peak frequency at 0.74 THz. This suggests that low frequency components can be guided in the wall but are not guided in the core region.

We measured the temporal waveforms ~300 μm from the plane of the output face of the waveguide in the two time windows 3-10 ps and 40-47 ps as shown in Figure 5.11 (c, d). In the early window the majority of the power is confined in the inner waveguide core and the peak to peak amplitude plot reveals a Gaussian beam profile. One can see the electric field is non-zero outside the capillary because of the weak guiding. The minimum of the electric field should be just at the inner interface of the wall because of destructive interference [17], which prevents the field from leaking. The spatial-temporal map in the late window reveals a signal concentrated around the walls and the fields on opposite walls are in phase.

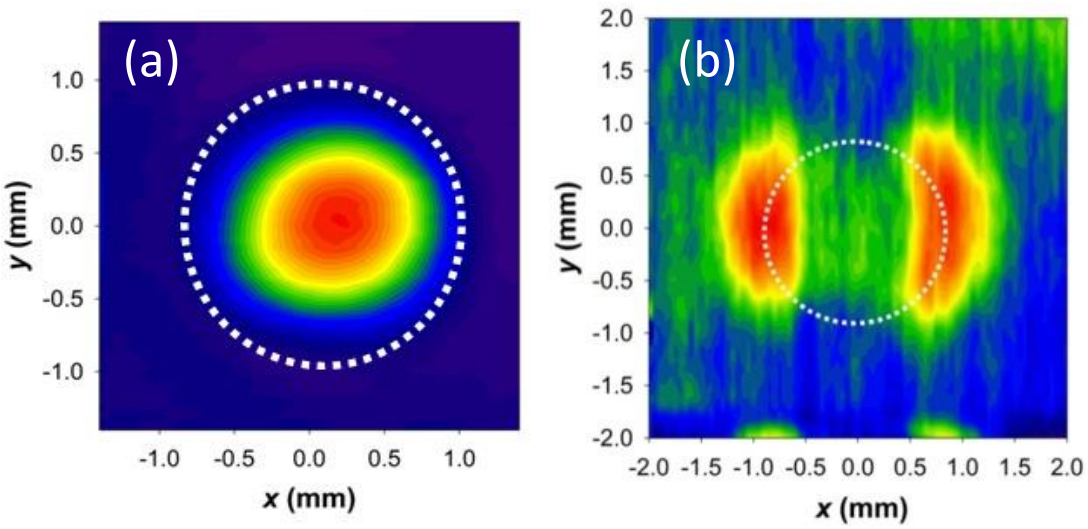

Figure 5.12. Cross-section 2D field maps measured at fixed time delays of (a) 4.75 and (b) 45 ps to confirm single mode propagation.

Figure 5.12 shows the measured modal amplitude distribution at fixed time-delays of 4.75 ps for the core mode and 45 ps for the cladding mode. The electric field

component along the x axis fills the hollow capillary, indicating a HE_{11} mode. For the cladding mode, the electric field is concentrated on the walls.

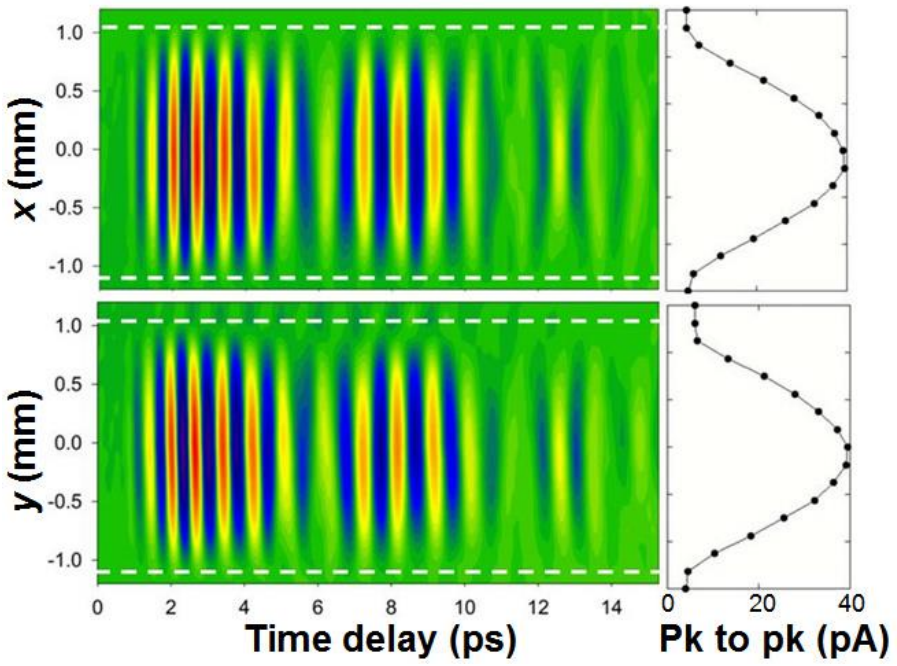

Figure 5.13. Spatial-temporal field maps of a 2.14 mm inner-diameter microstructured capillary of length 22.5 cm. The peak to peak amplitudes are plotted. The white dashed lines indicate the inner wall positions.

We then studied the beam profiles at the output end of the 2.14 mm inner-diameter microstructure capillary. As expected, the field maps (Figure 5.13a, b) along the x and y axes are nearly identical in terms of both time- and spatial- scales. No clear spatial interference pattern is evident over 15 ps, which indicates that the signal contains only the HE_{11} fundamental mode. The cladding mode is not seen in the measurements, which is likely be disturbed by the presence of the cladding structures and the thick outside jacket, since the distance between the core and cladding is only ~0.63 mm.

5.3.4 Loss

For a hollow cylindrical waveguide surrounded by an infinite dielectric, the attenuation constant for an HE_{nm} mode is given by [16]:

$$\alpha_{nm} = \left(\frac{u_{nm}}{\pi}\right)^2 \frac{\lambda^2}{d^3} Re\left[\frac{\nu^2+1}{\sqrt{\nu^2-1}}\right] \tag{5.11}$$

where d is the diameter of the core and $\nu = \sqrt{\epsilon/\epsilon_0}$ is the complex refractive index of the external medium and is usually real for dielectric made waveguides. The loss is proportional to λ^2/d^3. However, for simple capillaries with finite wall thickness, the loss is proportional to λ^3/d^4 [18].

As the capillary core diameter and wall thickness are varied together, it is impossible to compare the properties at a single frequency meaningfully. Instead, we performed cutback measurements to find the loss at the centre of the fundamental band in different structures and show the results in Figure 5.14. Compared with the same diameter simple capillary (77 dB m^{-1}), the microstructured capillary guides light with lower loss (42 dB m^{-1}), which we believe is due to the surrounding airspace and jacket [14]. Poletti *et al* [19] calculated the optimal cladding to core radius ratio in similar structures to be 0.65. The optimal structure in principle can reduce the loss by an order of magnitude compared with a simple capillary. The ratio of our microstructured cladding and the core radius in our capillary is 0.43, which is not too far from the optimum. In the context of THz waveguides, the disadvantage of the ARROW waveguide is that the loss is an order of magnitude greater than that in thin-dielectric coated metal tubes (1 dB m^{-1}) [20, 21]. However, the single mode propagation and controllable transmission bands indicate that there could be future applications of the microstructured capillary.

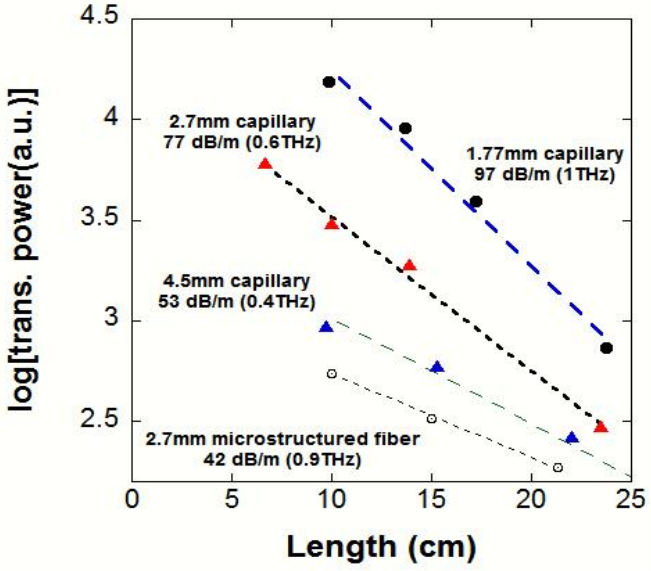

Figure 5.14. Cutback loss measurement near the central frequency in the fundamental band of the structures indicated.

5.4 Conclusions

We fabricated silica hollow core single and microstructured capillaries to guide THz radiation. The transmission loss from our microstructured capillary with inner diameter of 2.7 mm is 42 dB/m at 0.9 THz. Although the loss decreases with shorter wavelengths, the value is still more than an order of magnitude larger than can be obtained from metal waveguides, e.g. thin-dielectric coated metal tube (~1 dB/m) [20, 21]. However, this is not necessarily a limiting feature in the future applications that we envisage such as high energy THz guiding.

Combined with an experimental study of parallel thin-film dielectric waveguides, we were able to clearly show that higher frequencies are guided in the core by the anti-resonant reflection optical waveguide (ARROW) mechanism. Lower frequencies propagate in the cladding layers by total internal reflection in the subwavelength thick walls and significantly extend beyond the structure. The transmitted spectrum and the dispersion can be tuned by varying the wall thickness and the core diameter or film separation.

The microstructured silica capillary strategy offers control over bandwidth by varying the wall thickness. The thick glass outer jacket of the structure improves handling compared with conventional capillary and the wall-thickness is then easily fabricated to the desired dimensions of a few tens of micrometres. These features, together with the relatively high optical damage threshold of silica are attractive for prospective applications involving high optical and THz peak powers in rigid gas filled waveguides.

References

1. J.-Y. Lu, C.-P. Yu, H.-C. Chang, H.-W. Chen, Y.-T. Li, C.-L. Pan, and C.-K. Sun, "Terahertz air-core microstructure fiber," Applied Physics Letters **92**, 064105 (2008).

2. C.-H. Lai, Y.-C. Hsueh, H.-W. Chen, Y.-j. Huang, H.-c. Chang, and C.-K. Sun, "Low-index terahertz pipe waveguides," Optics Letters **34**, 3457-3459 (2009).

3. E. Nguema, D. Ferachou, G. Humbert, J.-L. Auguste, and J.-M. Blondy, "Broadband terahertz transmission within the air channel of thin-wall pipe," Optics Letters **36**, 1782-1784 (2011).

4. J. Anthony, R. Leonhardt, S. G. Leon-Saval, and A. Argyros, "THz propagation in kagome hollow-core microstructured fibers," Optics Express **19**, 18470-18478 (2011).

5. R. Mendis and D. Grischkowsky, "Plastic ribbon THz waveguides," J. Appl. Phys. **88**, 4449-4451 (2000).

6. Y.-S. Jin, G.-J. Kim, and S.-G. Jeon, "Terahertz dielectric properties of polymers," Journal of the Korean Physical Society **49**, 513-517 (2006).

7. E. Hecht and H. Eugene, *Optics* (San Francisco London : Addison-Wesley, San Francisco London, 2002).

8. S. Krishnamurthy, M. T. Reiten, S. A. Harmon, and R. A. Cheville, "Characterization of thin polymer films using terahertz time-domain interferometry," Applied Physics Letters **79**, 875-877 (2001).

9. L. J. Chen, H. W. Chen, T. F. Kao, J. Y. Lu, and C. K. Sun, "Low-loss subwavelength plastic fiber for terahertz waveguiding," Optics Letters **31**, 308-310 (2006).

10. M. Tacke and R. Ulrich, "Submillimeter wave-guiding on thin dielectric films," Optics Communications **8**, 234-238 (1973).

11. Y. Y. Wang, N. V. Wheeler, F. Couny, P. J. Roberts, and F. Benabid, "Low loss broadband transmission in hypocycloid-core Kagome hollow-core photonic crystal fiber," Optics Letters **36**, 669-671 (2011).

12. F. Yu, W. J. Wadsworth, and J. C. Knight, "Low loss silica hollow core fibers for 3-4 mu m spectral region," Optics Express **20**, 11153-11158 (2012).

13. F. Gerome, R. Jamier, J.-L. Auguste, G. Humbert, and J.-M. Blondy, "Simplified hollow-core photonic crystal fiber," Optics Letters **35**, 1157-1159 (2010).

14. S. Fevrier, B. Beaudou, and P. Viale, "Understanding origin of loss in large pitch hollow-core photonic crystal fibers and their design simplification," Optics Express **18**, 5142-5150 (2010).

15. P. S. J. Russell, "Photonic-crystal fibers," Journal of Lightwave Technology **24**, 4729-4749 (2006).

16. E. A. J. Marcatili and R. A. Schmeltzer, "Hollow metallic and dielectric waveguides for long distance optical transmission and lasers," Bell System Technical Journal **43**, 1783-1809 (1964).

17. P. J. Roberts, D. P. Williams, B. J. Mangan, H. Sabert, F. Couny, W. J. Wadsworth, T. A. Birks, J. C. Knight, and P. S. J. Russell, "Realizing low loss air core photonic crystal fibers by exploiting an antiresonant core surround," Optics Express **13**, 8277-8285 (2005).

18. M. Miyagi, "Bending losses in hollow and dielectric tube leaky waveguides," Appl. Opt. **20**, 1221-1229 (1981).

19. F. Poletti, J. R. Hayes, and D. Richardson, "Optimising the Performances of Hollow Antiresonant Fibres," in OSA Technical Digest (CD) (Optical Society of America, 2011)

20. O. Mitrofanov and J. A. Harrington, "Dielectric-lined cylindrical metallic THz waveguides: mode structure and dispersion," Optics Express **18**, 1898-1903 (2010).

21. O. Mitrofanov, R. James, F. A. Fernandez, T. K. Mavrogordatos, and J. A. Harrington, "Reducing Transmission Losses in Hollow THz Waveguides," Terahertz Science and Technology, IEEE Transactions on 1, 124-132 (2011).

Chapter 6

Planar structured metallic waveguide

6.1 Introduction

6.1.1 Surface plasmons

A metallic waveguide formed from parallel metal plates was described in Chapter 4. As the metallic surface is nearly a perfect reflector for terahertz waves, a parallel plate structure supports propagating waves with low loss and dispersion. The attenuation is due to Ohmic loss and increases inversely with the separation [1]. For a hollow cylindrical metal pipe, the loss is more severe and is inversely proportional to the cube of the diameter [2]. It is hard to achieve low loss and wavelength scale confinement with metal waveguides. Recently, electromagnetic surface waves have been explored as an alternative route to subwavelength scale THz guiding.

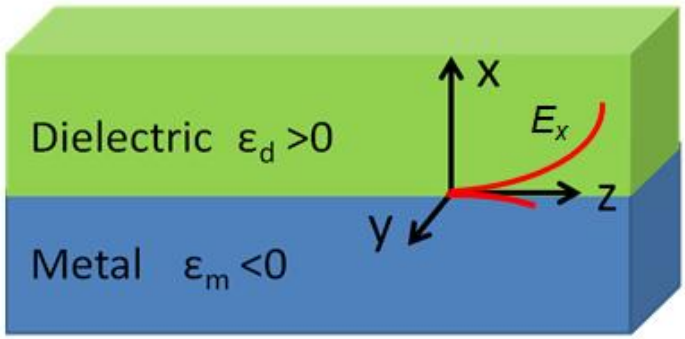

Figure 6.1. Schematic of surface plasmon polariton propagation at the interface of a dielectric and metal. The large extent of the field penetration into the dielectric and the small penetration into the metal are indicated.

The surface plasmon polariton (SPP) is a coupled excitation of an electromagnetic wave and the electron plasma at the interface of a metal and dielectric as shown in Figure 6.1 (a) [3].

In the Drude model, the bulk metal is regarded as a free electron gas. The dielectric function at frequencies is given by [4],

$$\varepsilon(\omega) = \varepsilon_{lattice} - \frac{\omega_p^2}{\omega^2 + i\omega\gamma} \tag{6.1}$$

which is determined by the scattering frequency γ, the plasma frequency ω_p, and the permittivity of the lattice $\varepsilon_{lattice}$. For the frequencies below the optical phonon frequencies in crystalline materials, the lattice permittivity is approximately constant and equal to the material permittivity at the zero frequency. The plasma frequency, ω_p, is determined by the free-electron density and effective mass,

$$\omega_p^2 = \frac{Ne^2}{m_e\varepsilon_0} = \frac{\sigma_0\gamma}{\varepsilon_0} \tag{6.2}$$

where N is the free electron density per unit volume, m_e is the effective electron mass and σ_0 is the dc conductivity. For most metals, ω_p lies in the ultraviolet. For gold, the plasma frequency is 1.2×10^{16} rad/s, the scattering frequency 1.2×10^{14} rad/s, and the lattice permittivity is approximately 9.1 [4]. At low frequency, such as THz frequencies, the real part and imaginary part of metal permittivity are approximately respectively given by,

$$\begin{aligned} Re[\varepsilon_m] &= -\frac{\omega_p^2}{\gamma^2} \\ Im[\varepsilon_m] &= i\frac{\omega_p^2}{\omega\gamma} \end{aligned} \tag{6.3}$$

where ε_m is very large and predominantly imaginary so that the surface plasmon polariton is weakly bound at THz frequencies.

The surface plasmon dispersion is related to the permittivity by,

$$k_z = \frac{\omega}{c}\sqrt{\frac{\varepsilon_m \varepsilon_d}{\varepsilon_m + \varepsilon_d}}. \tag{6.4}$$

As an example, the dispersion curve for a SPP at an air-copper interface is plotted in Figure 6.2. The red curve is the surface plasmon dispersion which lies below the light line and is bound to the surface. The mode above the bulk plasmon frequency is leaky and unbound.

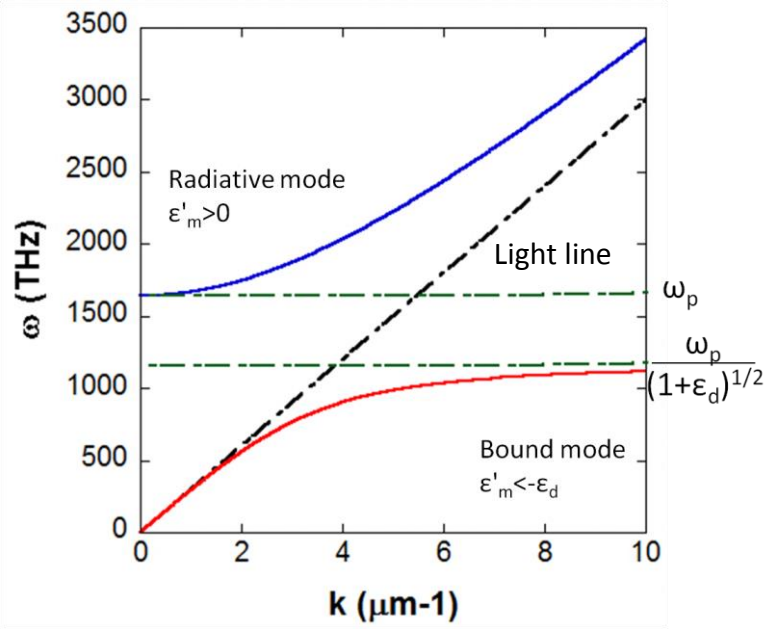

Figure 6.2. Dispersion of the SPP on an air-copper interface. The black dash-pointed line is the light line. N is 8.48×10^{28} m^{-3} and the approximation in Eq (6.4) is assumed.

For the bound SPP mode [4], the electromagnetic fields exponentially decay along the x axis in both the dielectric and metal. The decay length L_x is the distance over which the electric field of the SPP is reduced by a factor of 1/e,

$$L_x = \frac{1}{Im(k_x)} \tag{6.5}$$

where $k_x = i\sqrt{k_0^2 - k_z^2}$. Provided $\varepsilon_m \ll -\varepsilon_d$, the decay lengths can be approximated by,

$$L_x = \frac{c}{\omega} \cdot \begin{cases} 1/\sqrt{|\varepsilon_m|} & \text{in metal.} \\ \sqrt{|\varepsilon_m|/\varepsilon_d^2} & \text{in dielectric.} \end{cases} \tag{6.6}$$

The decay length in metal can also be estimated from the skin depth [5] at low frequency,

$$\delta_s = \sqrt{\frac{2}{\omega\mu\sigma}} \tag{6.7}$$

where $Im(\varepsilon_m) \sim \sigma/\omega\varepsilon_0$ and the skin depth is typically <100 nm at 1 THz. This assumption breaks down at frequencies above ~10 THz [6].

In the dielectric, the transverse confinement L_x is weak and the SPP extends over hundreds of wavelengths. The SPP is also known as a Zenneck wave on a flat metal surface [7]. In order to further localize the surface mode, the simplest solution is to alter the open boundary of the dielectric by using a higher dielectric constant material. For example, a thin dielectric coated onto the metal surface can collapse the surface field dramatically, so as to improve the confinement [8]. Inevitably, dispersion and material absorption are then increased.

6.1.2 Spoof surface plasmon polariton

Any disturbance of a flat surface can bind a surface mode. For example, as early as the 1970s, Ulrich reported THz guiding on a planar metallic mesh [9]. This early work led to the suggestion that subwavelength scale structuring of a metal surface could be used to engineer the dispersion of surface waves.

Periodic metallic structures can guide tightly bound THz surface waves, which have similarities to the much higher frequency SPP. Pendry [10] analysed a simple example of a flat metal sheet periodically structured with infinitely deep square holes of side a. An effective "plasmon" frequency is determined by the hole dimension,

$$\omega_{pl} = \frac{\pi c}{a\sqrt{\varepsilon_h}} \tag{6.8}$$

where ε_h are the permittivity of the dielectric material filling the holes. The in-plane dispersion is obtained as,

$$k_z^2 c^2 = \omega^2 + \frac{1}{\omega_{pl}^2 - \omega^2}\frac{64a^4\omega^4}{\pi^4 d^4} \tag{6.9}$$

where d is the period. In recognition of the fact that this wave is not an SPP but has a similar dispersion, Pendry used the phrase 'spoof' surface plasmon polariton (SSPP). Even a perfect electric conductor, for which there is no field penetration into the metal and no SPP, can still support SSPPs. Diffraction at the first Brillouin zone boundary gives a cutoff frequency, $\omega_c = \pi c/d$, which is lower than the SSPP frequency, ω_{pl}, if $\varepsilon_h = \varepsilon_0$. ω_{pl} can be shifted below ω_c by filling the holes with dielectric [11]. ω_{pl} is determined by the geometry rather than the properties of the metal. Therefore, SSPPs offer another solution to confining guided modes at surfaces.

6.2 Periodically perforated metal sheet

6.2.1 Introduction

The Bethe theory of transmission through a subwavelength circular aperture ($d < \lambda$) in an infinitesimally thin metallic screen gives a $1/d^3$ law for the electric field amplitude in the far field. The transmission is independent of polarization at normal incidence [12].

However, for a periodically perforated hole array, the story is different from that of a single hole. Ebbesen and his colleagues [13] first discovered an extraordinary optical transmission (EOT) many orders of magnitude greater than the Bethe predication at optical frequencies. EOT became a vibrant optical research field. The peak transmission frequency is smaller than the cutoff frequency of the hole waveguide, λ_c. The mechanism of EOT has been attributed to surface plasmon and shape effects. Recent theoretical and experimental work suggests that quasi-cylindrical wave (QCW) plays a significant role in EOT along with SPPs, when the hole spacing is roughly smaller than one wavelength [14]. The QCW is the field diffracted at the metal arrays surface and exist in the absence of SPPs.

EOT also occurs at frequencies well below the plasma frequency. Thick metal sheets perforated with periodic hole arrays have long been used as bandpass filters [15, 16] and as components of Fabry-Perot interferometers [17] in the microwave and THz regions. The transmission properties of individual holes and the excitation of SSPPs (which evolves from the QCWs) contribute to the total transmission spectrum. The transmission has features associated with Fano-type interference between the two

processes [18].

EOT is not limited to arrays of subwavelength elements. A single rectangular hole can also produce enhanced transmission [19, 20], which is known as a shape resonance. In contrast, single circular or square hole has no such shape resonant enhancement [21].

With terahertz time-domain spectroscopy, we are able to directly explore the spoof surface plasmon on periodic metal structures over a broad spectrum. Our group pioneered such studies with works on square holes arrays [22] and annular holes [23]. In these structures, the surface waves were confined to a single surface.

To explore guiding on two parallel surfaces, we have used freestanding metal sheets perforated with hexagonal arrays of subwavelength size circular holes. The samples were made using electroforming techniques on the thin nickel sheet and sold commercially under the name HiMesh [24]. The samples have previously been studied as narrow-band pass filters in the far-infrared by Huggard et al [25]. We firstly studied their filtering properties with a linearly polarized broadband THz beam at normal incidence. Then oblique transmission measurements were performed with either s- or p-polarized waves to explore the SSPP dispersion. Finally, we studied the in-plane waveguiding properties.

6.2.2 Normal transmission

For circular holes, the dominant contribution to the transmission is from the TE_{11} mode, which has a cutoff frequency given by Eq (3.7). At frequencies below the cutoff frequency the transmission is strongly attenuated. The periodic hole array acts as a grating to coherently scatter incident radiation into SSPPs.

For the SSPP mode, the resonant scattering wavevector k_{sspp} is given by [13],

$$k_{sspp} = k_z \pm G_{i,j} = k_0 \sin\theta \pm i\bar{b}_1 \pm j\bar{b}_2 \tag{6.10}$$

where $k_z = k_0 \sin\theta$ is the in-plane component of the incident wavevector, θ is the incident angle, i and j are the integers. If we define the real space primitive vectors as $\bar{a}_1 = g\bar{x}/2 + \sqrt{3}g\bar{y}/2$ and $\bar{a}_2 = g\bar{x}$, the reciprocal lattices are $\bar{b}_1 = 4\pi\bar{k}_y/\sqrt{3}g$ and

$\bar{b}_2 = 2\pi(\sqrt{3}\bar{k}_x - \bar{k}_y)/\sqrt{3}g$ for the hexagonal hole array of our samples, where g is the pitch of the hexagonal hole array. For normal transmission, the resonant wavelengths are given by [26],

$$\lambda = \frac{g}{\sqrt{\frac{4}{3}(i^2 + j^2 + ij)}} \left(\frac{\epsilon_d \epsilon_m}{\epsilon_d + \epsilon_m}\right)^{1/2}. \tag{6.11}$$

Our samples have the hexagonal lattices shown in Figure 6.3, with a pitch, g and film thickness of t. Each hole has a diameter of d_t on the top side which tapers to a minimum diameter of d_b on the bottom side. The bottom side has a shiny flat surface with holes of a good round shape. Our fibre-coupled far-field THz system was used to study the transmission with illumination through the bottom surface.

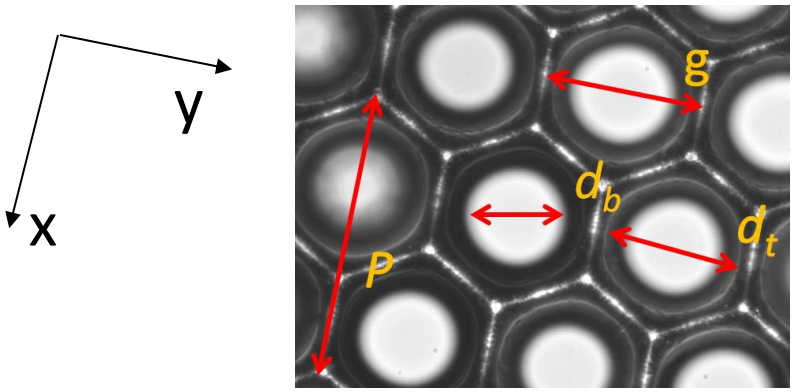

Figure 6.3. Microscope image of the upper surface of a metallic mesh with pitch g, hole diameters d_b and d_t.

Table 6.1. Dimensions of HiMesh samples

Parameters (μm)	**HiMesh 215**	**HiMesh 275**
Pitch (g)	118±1	91±1
Upper hole diameter (d_t)	98±2	77±2
Lower hole diameter (d_b)	77±2	55±2
Thickness (t)	55±1	55±1
TE_{11} cutoff frequency (THz)	~2.3	~3.2

The normal incidence transmission spectra of two samples are shown in Figure 6.4 (a). The HiMesh attenuates low frequencies significantly but allows high frequencies to pass through. The peak transmission is close to unity at 2.5 and 3.1 THz for HiMesh 215 and 275, respectively. Since the holes only cover ~30% of the total area of the film, this corresponds to a peak hole transmission efficiency exceeding unity.

Diffraction on periodic arrays also gives rise to spectral minima known as Wood or Rayleigh anomalies. Rayleigh named the spectral minima as "passing-off orders", which emerge tangential to be the plane of the arrays. At normal incidence, the wavelength of Wood anomalies is given by [26],

$$\lambda_R = \frac{\sqrt{3}g}{2n} \tag{6.12}$$

where $n = \pm 1, \pm 2$ ... and the sign describes positive or negative diffraction orders. At THz frequencies, λ_R is almost equal to the SSPP wavelength because $\epsilon_m \ll -\epsilon_d$. At $\theta = 0^o$, the calculated Wood anomaly frequency is 2.9±0.045 THz for HiMesh 215, which corresponds to the dip at ~3 THz in Figure 6.4 (a). For HiMesh 275, the calculated value is 3.8±0.045 THz and the measured dip probably appears at 3.7 THz in Figure 6.4 (a). Due to the THz system's spectral response, the results have poor accuracy above 3.5 THz.

Figure 6.4 (b) shows the normalized peak to peak amplitude as a function of the azimuth angle, α (defined in Figure 6.4c), for the HiMesh 215 and 275 along the z axis. It is surprising that the transmitted amplitude changes with the orientation of the polarization relative to the lattice. This behaviour is unrelated to which side of the HiMesh faces the THz transmitter. The transmitted maxima and minima angles appear at fixed geometrical orientations. The peaks are at the angles of ~150o/330o parallel to the (√ 3, 3) direction and the dips at ~60o/210o parallel to (√ 3, -1), as shown in Figure 6.4 (c).

We examined another HiMesh sample with a hexagonal pitch of 375 μm and found no polarization-dependent transmission. Inspected under a microscope, this larger pitch sample appeared more symmetrical. Previous studies suggested that the normal transmission is independent of the point group symmetry [26, 28]. We conclude that the

polarization dependence of the transmissions in Figure 6.4 (b) is due to fabrication artefacts.

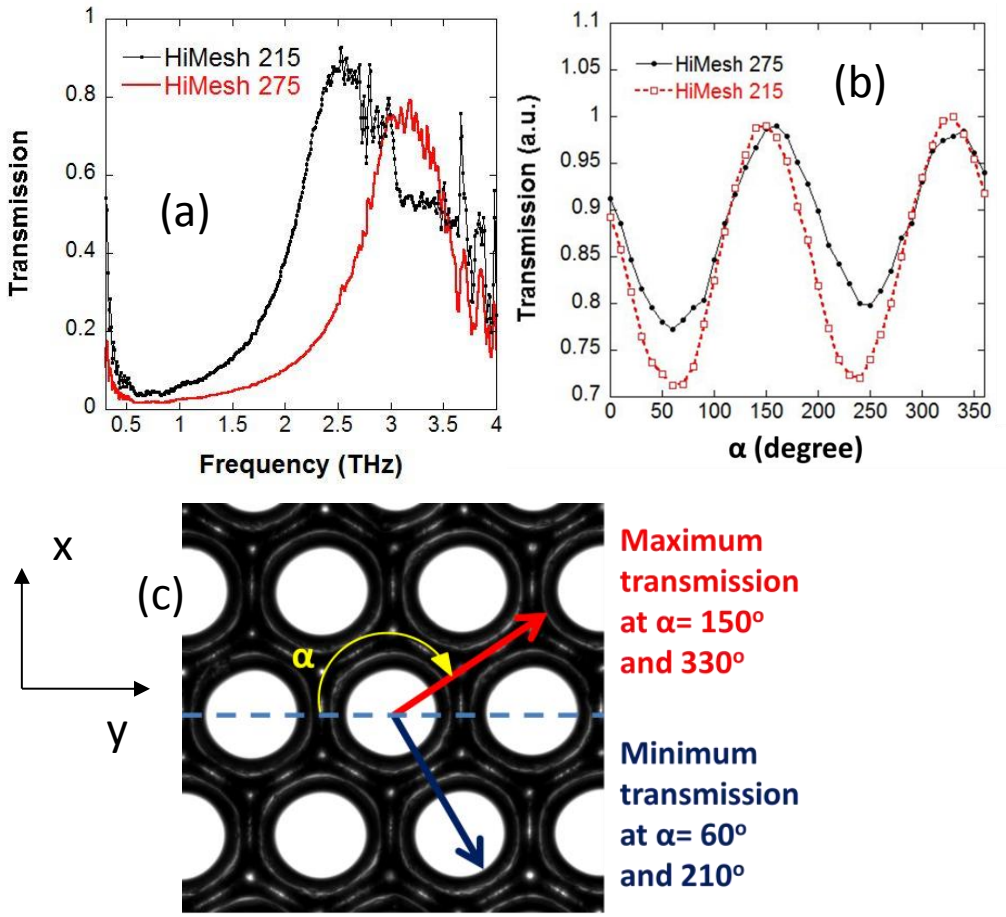

Figure 6.4. (a) Normal incidence transmission spectra of two HiMesh samples. (b) Normalized transmitted peak to peak measurement as a function of azimuthal angle. (c) The direction of the peak and dip are related to fabrication variations.

We performed numerical simulations of transmission through HiMesh 275 using CST Microwave Studio. The circular holes were modelled as truncated cones with diameters of 55 and 80 µm on opposite sides of the structure. The thickness of the structure was 50 µm and the pitch was 92 µm. The structure was modelled as a PEC consisting of a 40 × 20 hole array. Open boundaries were used in all directions. A waveguide port was placed 300 µm away from the sample to collect the transmission. In Figure 6.5, the simulated result shows reasonable agreement with the measured results below 3.5 THz. The dip at 3.8 THz corresponds to the Wood anomaly. The discrepancy can probably be attributed to differences between the parameters used in the model and the real sample. We also simulated the same hexagonal structure but with straight holes of diameter of 55 µm, which showed a narrower band transmission as seen in Figure 6.5.

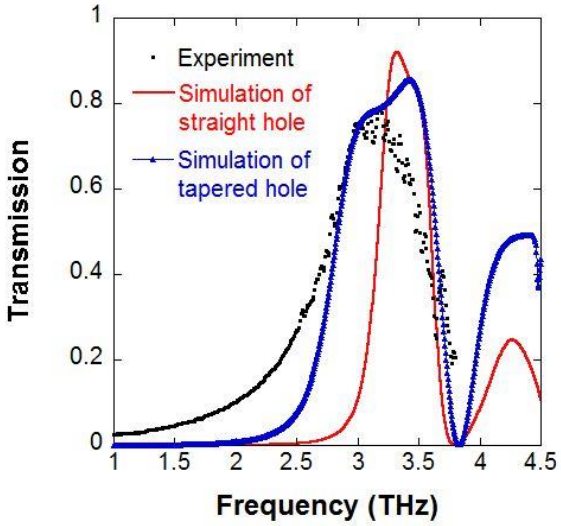

Figure 6.5. Normal transmission comparison of measurement and simulation of HiMesh 275.

6.2.3 Transmission at oblique angles

In this section, we discuss the transmission at oblique incidence where the sample of HiMesh 275 was rotated about the x or y axes with the electric field parallel or perpendicular to the rotation axis.

Figures 6.6 and 6.7 show transmission measurements for different tilt angles. Let us firstly look at the p-polarized wave with the magnetic field H_y parallel to the lattice direction (0,1) in Figure 6.6 (a). The 10^o spectrum shows a prominent transmission peak at 3.0 THz and strong attenuation at lower frequencies. A sharp dip at ~3.17 THz is attributed to the Wood anomaly. The calculated value is ~3.21 THz according to Eq (6.13). With increasing angle of incidence, the transmission peak and dip shift to lower frequencies and a second peak appears at higher frequency. For example, the second peak appears at ~3.0 THz at the incident angle of 60^o.

For the other transmission configurations in Figures 6.6 and 6.7, the spectra show similar behaviour with increasing angle. In Figure 6.7 (b), the prominent peak remains strong with near unity transmission, and the pass band becomes narrower with increasing angles. For example, the Q-factor is about ~58 at the incident angle of 60^o.

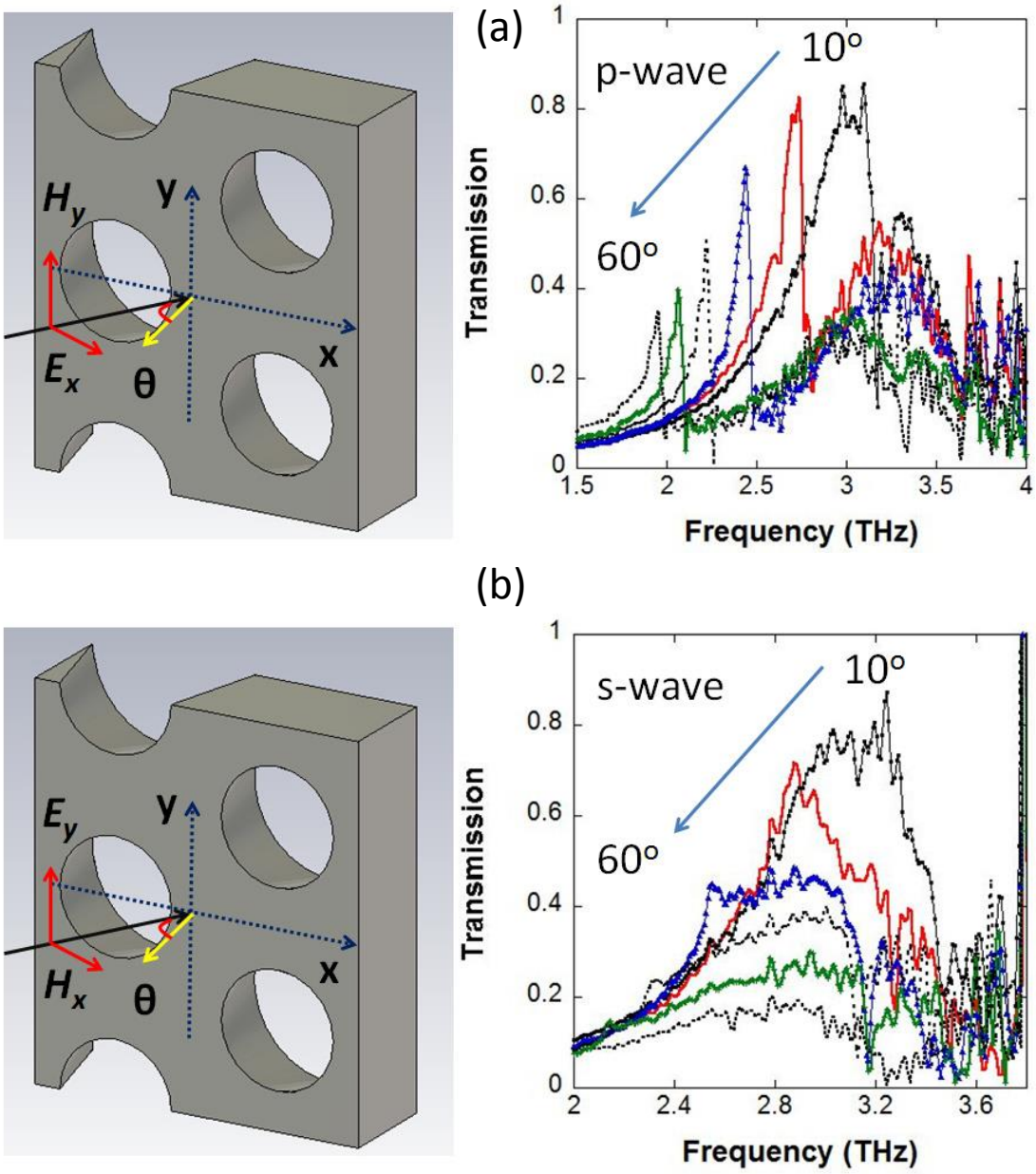

Figure 6.6. Measurements of oblique transmission when HiMesh 275 is rotated by an angle θ about the y axis in 10° steps. The left hand panels show the configuration of the measurements. (a) The magnetic field H_y is parallel to the y axis. (b) The electric field E_y is parallel to the y axis.

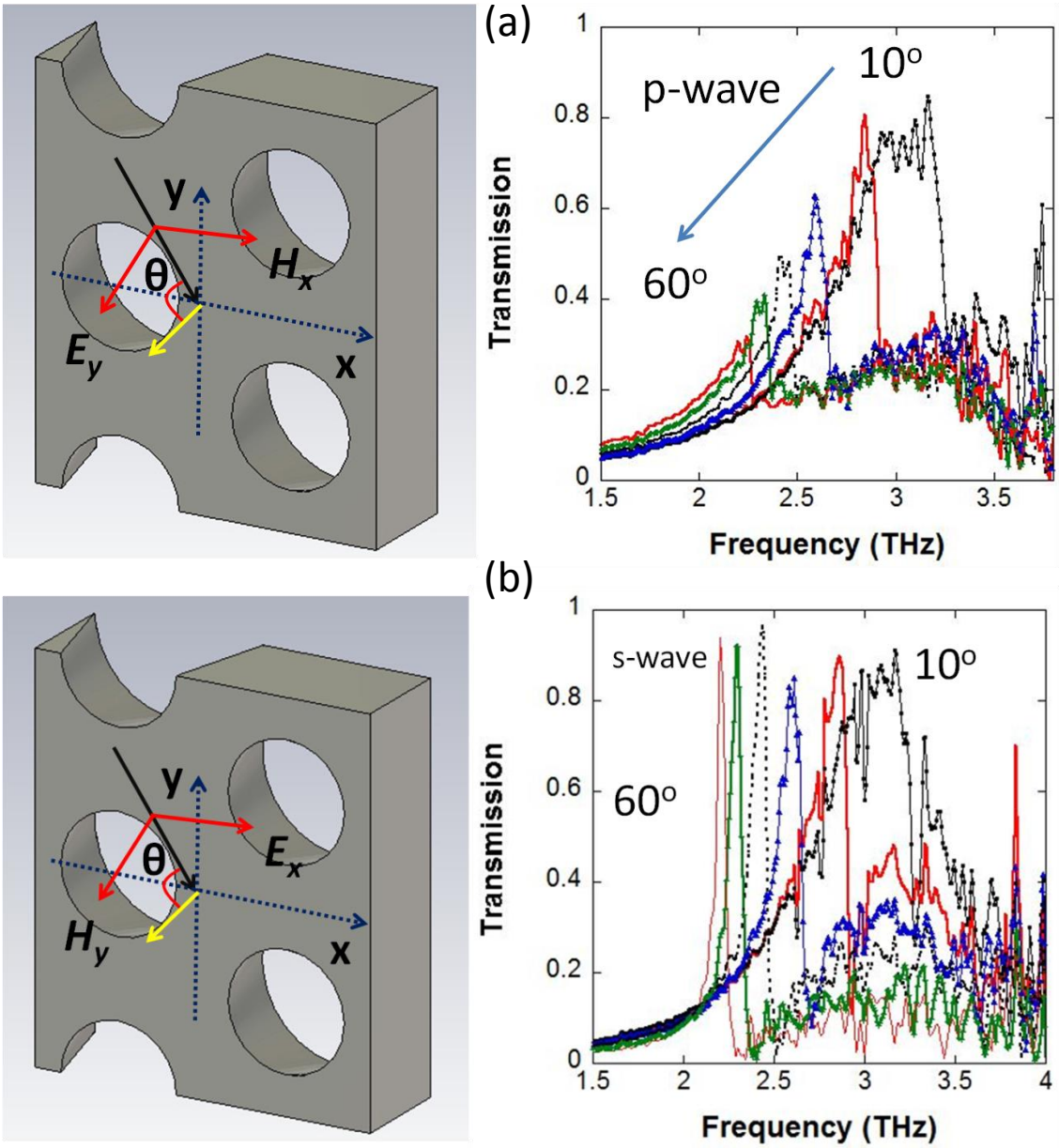

Figure 6.7. Measurements of oblique transmission when HiMesh 275 is rotated by an angle θ about the x axis in 10° steps. The left hand panels show the configuration of the measurements. (a) The magnetic field H_x is parallel to the x axis. (b) The electric field E_x is parallel to the x axis.

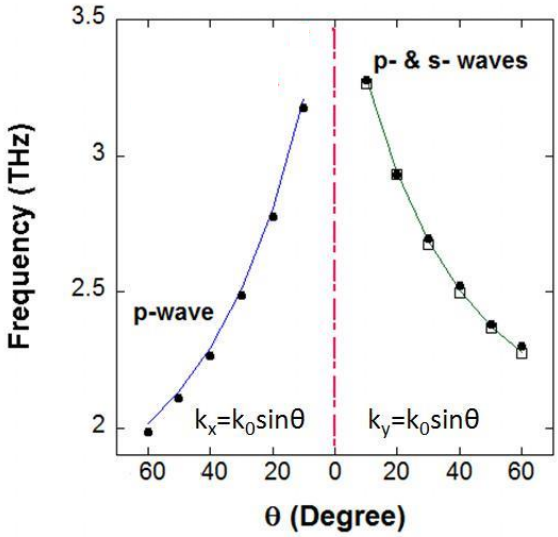

Figure 6.8. Dispersion curves of SSPP. The left side points are extracted from the results in Figure 6.6 and right side from Figure 6.7. The solid lines are the calculated results using Eq (6.13) for k_x and Eq (6.14) for k_y.

When the angle is varied, the incident radiation excites different wavevector SSPP modes. By plotting the dip frequencies just after the prominent peaks as a function of the angle θ, we obtain the dispersion relations shown in Figure 6.8. Using Eq (6.10) with $k_{x,y} = k_0 \sin\theta$, we can obtain the first order SSPP frequencies from

$$\frac{2c}{\sqrt{3}f} - g\sin\theta = g, \qquad (i,j) = (1,0) \tag{6.13}$$

$$\left(\frac{c}{f} - g\sin\theta\right)^2 + \frac{1}{3}\left(\frac{c}{f}\right)^2 = g^2, \quad (i,j) = (0,1)\,. \tag{6.14}$$

We then performed computer simulations using the same tapered-hole model as described above. For the results shown in Figure 6.9 (a), the excitation configuration is the same as that in Figure 6.6 (a) with tilt angle of 20°. The simulated result is scaled to fit the peak amplitude at 2.72 THz in the experiment data. There is good agreement between simulation and experiment for the peak frequencies of ~2.72 THz and ~3.2 THz and the dip at ~2.8 THz.

Figure 6.9 (b) shows the simulation result for the configuration of Figure 6.7 (b) with incident angle of 20°. The peak transmission at ~2.8 THz and dip at ~2.94 are again in good agreed with the experiment results. The simulated models are based on the PEC

approximation which cannot support surface plasmons. Therefore, the transmission spectrum can be explained by diffraction by the periodic holes array.

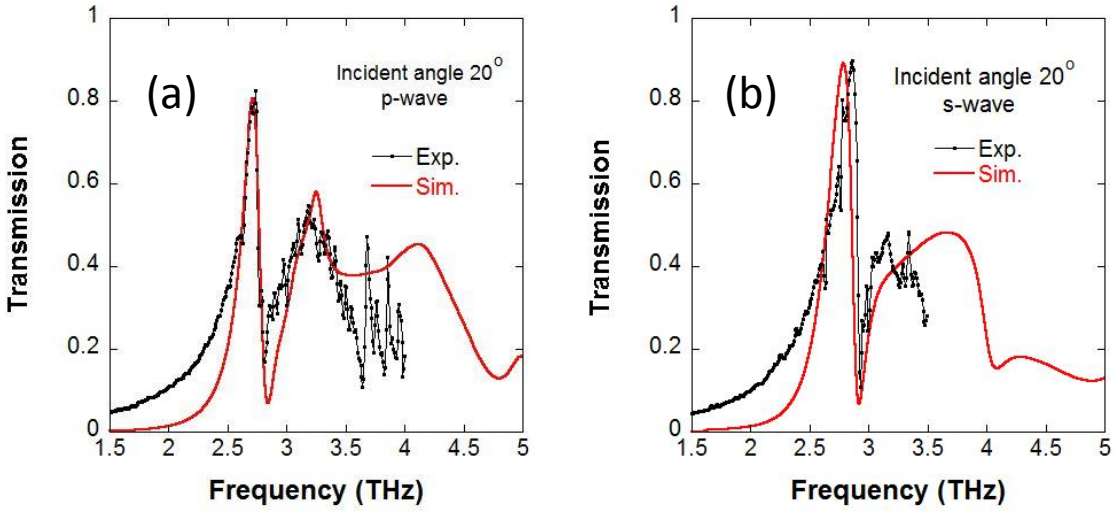

Figure 6.9. (a) Comparison of simulated and experimental results for 20° tilt about the y axis with the electric field parallel to the x axis. (b) Comparison for 20° tilt about the x axis with the electric field parallel to the y axis.

6.3 SSPP waveguide

6.3.1 In-plane THz waveguiding

Here, we study the waveguide properties of HiMesh 275. The propagation direction was arranged to be parallel to the (1,0) direction. Figure 6.10 shows the setup of the measurements. The self-supporting metal mesh was kept flat by stretching it over two metal bars. Steel razor blades were placed ~100 μm from the sample surface to minimize the signal from unguided radiation.

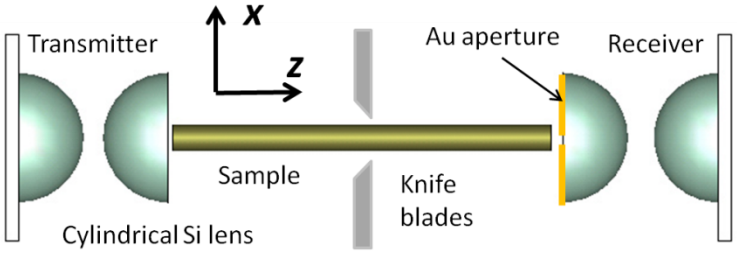

Figure 6.10. Schematic of the experimental setup.

We used cylindrical silicon lenses for end-fire coupling in and out of the SSPP modes of the waveguide. The collection cylindrical lens was covered by a pair of gold coated Mylar films to create an open slit of ~220 μm width. The gold layer is 300 nm thick which is larger than the skin depth of 80 nm at 1 THz. This technique allowed us to study the coupled-out field from the waveguide with good spatial resolution by displacing the collection lens along the x axis. The output coupling silicon lens was about ~100 μm away from the end of the guide.

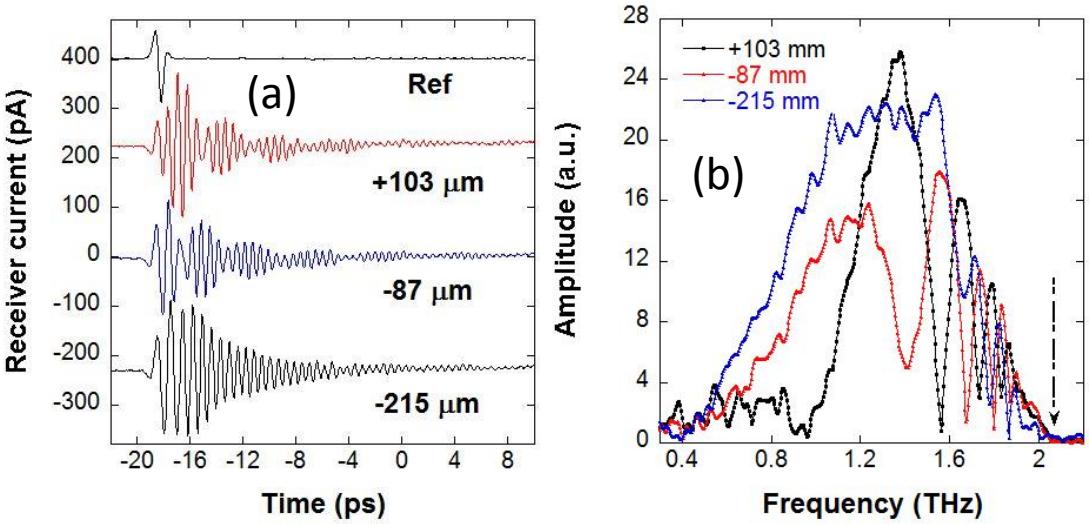

Figure 6.11 (a) Experimental time-domain traces at different positions in x for HiMesh 275 as well as the free space reference signal. (b) Spectra corresponding to the traces in (a). The black dashed arrow shows the calculated SSPP frequency of 2.17 THz in the orientation of (1,0).

When the collection lens was translated along the x axis, the position of minimum signal amplitude was taken as the centre of the waveguide (x = 0). Interestingly, different guiding modes were observed at the front and back surfaces of the HiMesh, which is due to the asymmetry in the structure. Figure 6.11 (a) shows time-domain measurements at the x positions of +103 and -87 μm. The corresponding spectra (Figure 6.11b) reveal a series of sharp dips, which move closer together with increasing frequency. The chirped spectrum arises from interference between two surface modes with different nonlinear dispersion. By moving to -215 μm, we find a different spectrum with fewer dips. This shows that the field at the end of the waveguide changes rapidly with x.

To further understand the asymmetry between the two surfaces, we simplified the

HiMesh by attaching a metal plate to one of the surfaces with a thin layer of paraffin oil (see the inset of Figure 6.12b). As the thickness of the nickel sheet is ~55 μm and the oil film is about a few μm, the dispersion is not significantly changed by oil in the holes. The coupling was the same as described above. The transmission spectrum shown in Figure 6.12 (a) exhibits no sharp features. By performing the same measurement on the opposite side we obtained a similar but slightly different spectrum shown in Figure 6.12 (a). The lower surface has smaller diameter holes which should support a more dispersive mode, so that the dispersion curve bends away from the light line faster than the upper surface guiding mode. This experiment confirms that the two surfaces support different SSPP modes because of the asymmetric structure.

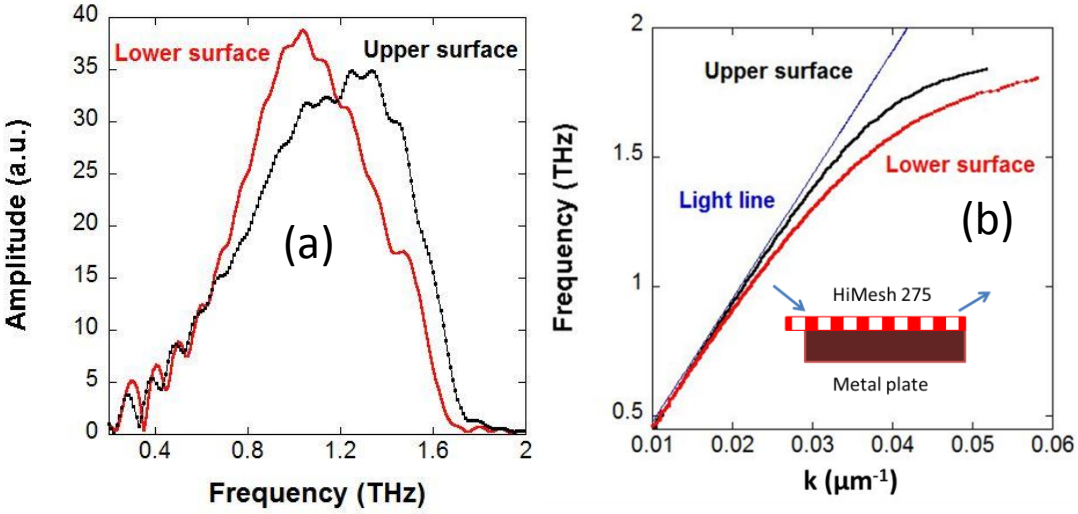

Figure 6.12. HiMesh backed by a metal plate. (a) The spectra of the upper and lower surfaces. (b) The SSPP dispersion curves. The inset shows a sketch of the geometry.

From the phase spectra and the propagation length of 3.9 cm, we can obtain the dispersion and effective refractive index n_{eff} using the equation,

$$k = k_0 + \frac{\Delta\varphi(\omega)}{L} = k_0 \cdot n_{eff} \tag{6.15}$$

where $\Delta\varphi(\omega)$ is the difference between the phase spectra with and without the sample in place, L is the sample length, k is the propagation constant of the waveguide, and k_0 is the free space wavevector. The different dispersion curves for the upper and lower surfaces are shown in Figure 6.12 (b). The refractive index is only slightly larger than that of air. For example, n_{eff} is about ~1.015 at 1.8 THz for the lower surface mode.

Using the experimental dispersion curve, we can estimate the field decay length in air, using Eq (6.5). At 1.5 THz, we obtain L_x = 273 μm (~λ). The loss of the HiMesh is due to the finite metal conductivity and scattering at imperfection. We have not measured the attenuation, but the loss would be expected to be similar in order of magnitude to other metamaterials (several dB/cm). For Ulrich's mesh [9], the loss at the frequency of 0.89 THz (λ = 337 μm) was as high as 5 dB/cm. For comparison, Williams *et al*'s dual band THz coaxial surface waveguide was measured to have a loss of 1.91 dB/cm within a 3 THz band [22] . Practical applications should consider the trade-off between confinement and loss.

6.3.2 Modal interference

We simulated waveguiding on the HiMesh using CST Microwave Studio. The nickel material was given a conductivity of 1.44 $\times 10^7$ S/m and surface impedance matching boundary conditions were used. The holes were modelled asf truncated cones with end diameters of 55 and 80 μm. The simulated length was 1 cm and probes were placed 160 μm away from the waveguide end. A port mode with the electric field parallel to the x axis was used to excite modes on the upper and lower surfaces.

Figure 6.13 (a) shows a schematic of interference by the modes guided on opposite sides of the HiMesh. Figure 6.13 (b) and (c) compare the measured spectra at x = +103 and -87 μm with the simulated spectra at x = +77 and -77 μm. Spectra dips rely on the SSPPs on the upper and lower surfaces having different dispersions and appear when the phases differ by an integer multiple of π. The dip frequencies become chirped towards higher frequencies because the nonlinear dispersions have a rapid change in phase at frequencies close to the cutoff frequency. The simulation results show good qualitative agreement with the experiments. The dips shift in frequency and change amplitude along both x and z axes. The strong interference between the SSPPs occurs in the near field region ($z < \lambda$). We did not observe spectral interference in the far field in experiments. Unlike a single surface guide, modal interference must be considered to interpret the transmission spectrum of the HiMesh guide.

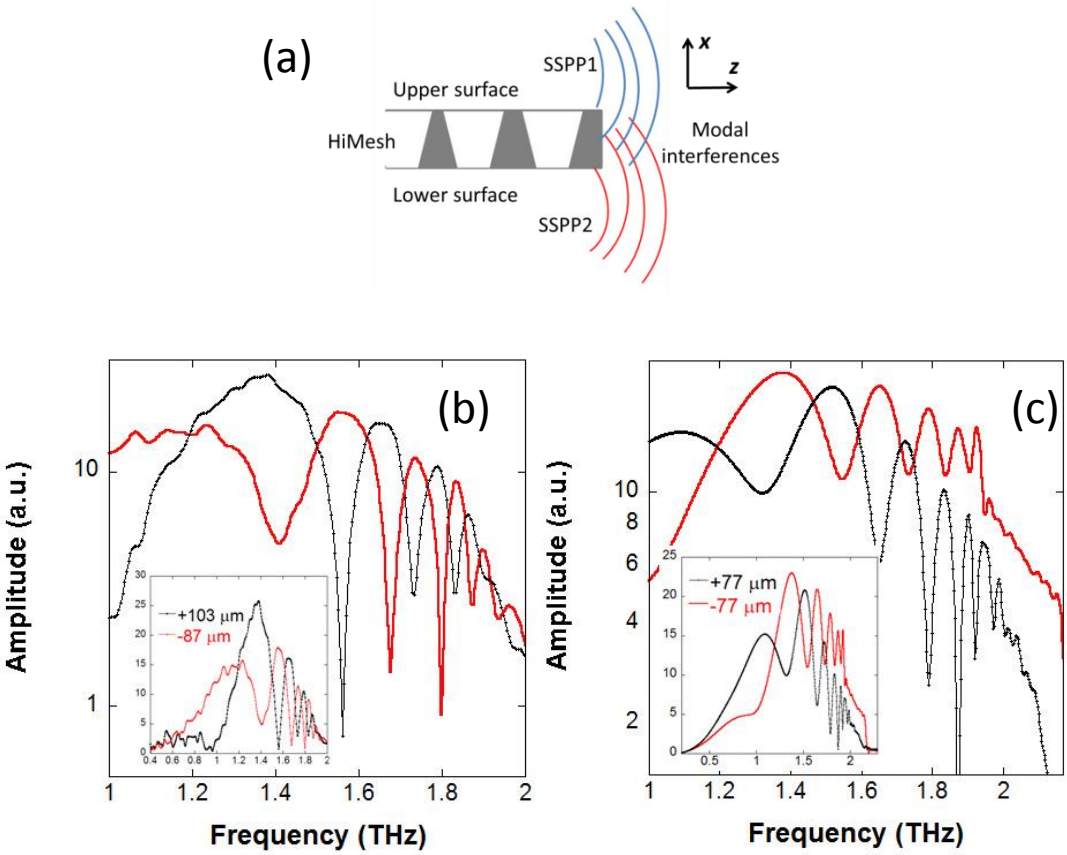

Figure 6.13. (a) Schematic of the SSPP modal interference (b) Normalized amplitudes of measured spectra at x = +103 and -87 μm (c) Simulated spectra at x = +77 and -77 μm. The insets show the linear scale spectra with an expanded range.

6.4 Conclusions

In summary, we have studied the transmission and waveguide properties of freestanding nickel sheet perforated with hexagonal arrays of conical holes. At normal incidence the metal meshes act as a bandpass filter with the frequency of maximum transmission just below the Wood anomaly. The oblique transmission of s- and p-polarised waves was measured to study the SSPP dispersion as a function of angle. There is a good agreement between the simulation and measurement. As the perfect conductor approximation was used for which there is no surface plasmon, the transmission was attributed to the excitation of spoof surface plasmon polaritons which have an upper frequency limited by diffraction at the Wood anomaly.

The metal meshes can support SSPPs on the front and back surfaces with different dispersion. The strongly nonlinear dispersion of the SSPPs gives rise to strongly

chirped interference spectra at the output end. The HiMesh may find an application in chemical sensing as the interference features are sharp and prominent over a broad frequency range.

References

1. J. Q. Zhang and D. Grischkowsky, "Adiabatic compression of parallel-plate metal waveguides for sensitivity enhancement of waveguide THz time-domain spectroscopy," Applied Physics Letters **86**, 061109 (2005).

2. M. Miyagi, "Bending losses in hollow and dielectric tube leaky wave-guides," Applied Optics **20**, 1221-1229 (1981).

3. W. L. Barnes, A. Dereux, and T. W. Ebbesen, "Surface plasmon subwavelength optics," Nature **424**, 824-830 (2003).

4. T. H. Isaac, W. L. Barnes, and E. Hendry, "Determining the terahertz optical properties of sub wavelength films using semiconductor surface plasmons", Applied Physics Letter **93**, 241115 (2008).

5. D. M. Pozar and M. P. David, *Microwave engineering* (New York Chichester : Wiley, New York Chichester, 2004).

6. C. Williams, "Terahertz waveguiding on metamaterials." PhD Thesis, University of Bath, 2009

7. J. Tae-In and D. Grischkowsky, "THz Zenneck surface wave (THz surface plasmon) propagation on a metal sheet," Applied Physics Letters **88**, 061113 (2006).

8. M. Gong, T.-I. Jeon, and D. Grischkowsky, "THz surface wave collapse on coated metal surfaces," Opt. Express **17**, 17088-17101 (2009).

9. R. Ulrich and M. Tacke, "Submillimeter waveguiding on periodic metal structure," Applied Physics Letters **22**, 251-253 (1973).

10. J. B. Pendry, L. Martin-Moreno, and F. J. Garcia-Vidal, "Mimicking surface plasmons with structured surfaces," Science **305**, 847-848 (2004).

11. A. P. Hibbins, E. Hendry, M. J. Lockyear and J. R. Sambles, "Prism coupling to 'designer' surface plasmons", Optics Express **16**, 20441-20447 (2008.)

12. C. Genet and T. W. Ebbesen, "Light in tiny holes," Nature **445**, 39-46 (2007).

13. T. W. Ebbesen, H. J. Lezec, H. F. Ghaemi, T. Thio, and P. A. Wolff, "Extraordinary optical transmission through sub-wavelength hole arrays," Nature **391**, 667-669 (1998).

14. F. van Beijnum, C. Retif, C. B. Smiet, H. Liu, P. Lalanne, and M. P. van Exter, "Quasi-cylindrical wave contribution in experiments on extraordinary optical transmission," Nature **492**, 411-414 (2012).

15. C. Winnewisser, F. Lewen, J. Weinzierl, and H. Helm, "Transmission features of frequency-selective components in the far infrared determined by terahertz time-domain spectroscopy," Appl. Opt. **38**, 3961-3967 (1999).

16. C. Chao-Chun, "Transmission of microwave through perforated flat plates of finite thickness," Microwave Theory and Techniques, IEEE Transactions on **21**, 1-6 (1973).

17. R. D. Rawcliffe and C. M. Randall, "Metal mesh interference filters for the far infrared," Appl. Opt. **6**, 1353-1358 (1967).

18. J. Bravo-Abad, L. Martin-Moreno, F. J. Garcia-Vidal, E. Hendry and J. Gomez Rivas, "Transmission of light through perodic arrays of sqaure holes: From a metallic wire mesh to an array of tiny holes", Physical Review B **76**, 241102 (2007).

19. Z. Ruan and M. Qiu, "Enhanced transmission through periodic arrays of subwavelength holes: the role of localized waveguide resonances," Physical Review Letters **96**, 233901-233904 (2006).

20. K. J. K. Koerkamp, S. Enoch, F. B. Segerink, N. F. van Hulst, and L. Kuipers, "Strong influence of hole shape on extraordinary transmission through periodic arrays of subwavelength holes," Physical Review Letters **92**, 183901 (2004).

21. J. W. Lee, M. A. Seo, D. H. Kang, K. S. Khim, S. C. Jeoung, and D. S. Kim, "Terahertz electromagnetic wave transmission through random arrays of single rectangular holes and slits in thin metallic sheets," Physical Review Letters **99**, 137401 (2007).

22. C. R. Williams, S. R. Andrews, S. A. Maier, A. I. Fernandez-Dominguez, L. Martin-Moreno, and F. J. Garcia-Vidal, "Highly confined guiding of terahertz surface plasmon polaritons on structured metal surfaces," Nature Photonics **2**, 175-179 (2008).

23. C. R. Williams, M. Misra, S. R. Andrews, S. A. Maier, S. Carretero-Palacios, S. G. Rodrigo, F. J. Garcia-Vidal, and L. Martin-Moreno, "Dual band terahertz waveguiding on a planar metal surface patterned with annular holes," Applied Physics Letters **96**, 011101 (2010).

24. Stork Screens B. V., 5830 AB Boxmeer, Holland.

25. P. G. Huggard, M. Meyringer, A. Schilz, K. Goller, and W. Prettl, "Far-infrared bandpass-filters from perforated metal screens," Applied Optics **33**, 39-41 (1994).

26. T. Thio, H. F. Ghaemi, H. J. Lezec, P. A. Wolff, and T. W. Ebbesen, "Surface-plasmon-enhanced transmission through hole arrays in Cr films," J. Opt. Soc. Am. B **16**, 1743-1748 (1999).

27. D. Jackson, "EM scattering from perforated films: transmission and resonance," (Duke University, 2012). PhD Thesis

28. J. Braun, B. Gompf, T. Weiss, H. Giessen, M. Dressel, and U. Hübner, "Optical transmission through subwavelength hole arrays in ultrathin metal films," Physical Review B **84**, 155419-155414 (2011).

Chapter 7

Summary and suggestions for future work

This thesis reported experimental studies of THz photoconductive devices and waveguided components. The main scope of the study was to explore new THz photonic tools for next-generation THz systems. The experimental work was undertaken using a photoconductive THz time-domain spectrometer in the frequency range 0.1 to 3 THz. Supporting numerical modelling was performed by CST Microwave Studio.

In chapter 2, an interdigitated photoconductive GaAs transmitter emitted an average THz power up to ~27 μW under a femtosecond laser pump power of 180 mW. The power from the new device was double that from a conventional 50 μm gap coplanar stripline transmitter. Further improvements in efficiency can be made by using higher laser pump powers whereas the output of the conventional transmitter saturated at about 100 mW.

In chapter 3, four different photoconductive receiver antennas, including dipoles and a bowtie, were compared in terms of bandwidth and sensitivity. The experiment results and CST Microwave simulations are in good agreement so the software can be used to design new antennas with tailored response.

The development of THz near-field imaging systems was reported in Chapter 3. In particular, a photoconductive near-field probe, consisting of a LT-GaAs thin-film receiver and an integrated subwavelength-size aperture, was fabricated and operated at very small distance from samples (~20 μm). The drawback of the probe is that imaging artefacts associated with waveguiding in the gap between sample and probe restrict

what can be measured and hinder imaging interpretation. These drawbacks could be overcome using electro-optic probing in the future.

In chapter 4, a variety of waveguides was studied. A step was fabricated in a parallel metal plate waveguide (PPWG) to generate higher order modes (TM_1) alongside with the fundamental TEM mode. Using the near-field probe, the properties of the different modes were easily observed in a 2D spatial-temporal map.

A linearly tapered parallel plate waveguide was shown to focus a mm-size THz beam into a subwavelength mode with a FWHM as small as 20 μm × 40 μm. The propagating beam at the immediate output end was measured by the near-field probe in the time domain and good agreement was found with CST Microwave Studio calculations. Experimentally, the overall transmission was lower than expected so that further investigation is needed.

A thin-layer of high-index material surrounding an air core can guide broad band THz radiation. In the first half of Chapter 5, a parallel dielectric film waveguide was formed by two thin Mylar films with mm-wide separation. This waveguide supported two different modes: higher frequency components were confined in the central core by the antiresonant optical reflection (ARROW) mechanism; and lower frequency components were guided by individual films due to total internal reflection.

In the second half of this chapter, a microstructured silica capillary with thin inner walls was fabricated by the stack-and-draw techniques. The microstructured capillary showed a relative lower loss of 42 dB/m at 0.9 THz, compared with a single capillary of the same diameter (77 dB/m at 0.6 THz). The improved loss character was attributed to the presence of interference in the structured cladding, although further work is needed to confirm and fully understand this. Although the loss was still orders of magnitude larger than that of thin dielectric-coated metal tubes (1 dB/m at1 THz), such waveguides can support single mode and broadband transmission windows and chromatic dispersion can be tuned by the waveguide geometry and materials. This type of waveguides is currently being explored for guiding an air plasma generation.

In chapter 6, a freestanding thin nickel sheet perforated with a periodic array of holes was used to guide THz radiation as spoof surface plasmon polaritons (SSPPs). As the

hole diameters on the two surfaces of the sheet are slightly different, two modes propagated independently with different nonlinear dispersions. Strong, unequally separated spectral interference minima occurred in the near-field transmission as a result. This feature could make the waveguide of interest for chemical sensing applications.

In conclusions, we have explored some aspects of THz technology which contribute to push towards exploiting this part of the spectrum for practical applications.

Publications

The work in this thesis is, in part, based on the following publications:

Journal article:

Chapter 3: M. Misra, Y. Pan, C. R. Williams, S. A. Maier, and S. R. Andrews, "Characterization of a hollow core fibre-coupled near field terahertz probe," Journal of Applied Physics **113**, 193104 (2013).

Conference paper:

Chapter 5: Y. Pan, S.R. Andrews, F. Yu, and J.C. Knight. "Single-mode microstructured silica waveguide for broadband terahertz transmission," 3rd EOS Topical Meeting on Terahertz Science & Technology, Prague, Czech Republic (2012).